Understanding Defects in Germanium and Silicon for Optoelectronic Energy Conversion

by

Neil Sunil Patel

B.S., Georgia Institute of Technology (2009)

Submitted to the Department of Materials Science and Engineering
in partial fulfillment of the requirements for the degree of

Doctor of Philosophy

at the

MASSACHUSETTS INSTITUTE OF TECHNOLOGY

June 2016

© Massachusetts Institute of Technology 2016. All rights reserved.

Author .....
Department of Materials Science and Engineering
May 17, 2016

Certified by .....
Lionel C. Kimerling
Thomas Lord Professor of Materials Science and Engineering
Thesis Supervisor

Certified by .....
Anuradha M. Agarwal
Principal Research Scientist, Materials Processing Center
Thesis Supervisor

Accepted by .....
Donald Sadoway
Chairman, Department Committee on Graduate Theses

Understanding Defects in Germanium and Silicon for Optoelectronic Energy Conversion

by

Neil Sunil Patel

Submitted to the Department of Materials Science and Engineering
on May 17, 2016, in partial fulfillment of the
requirements for the degree of
Doctor of Philosophy

Abstract

This thesis explores bulk and interface defects in germanium (Ge) and silicon (Si) with a focus on understanding the impact defect related bandgap states will have on optoelectronic applications. Optoelectronic devices are minority carrier devices and are particularly sensitive to defect states which can drastically reduce carrier lifetimes in small concentrations.

We performed a study of defect states in Sb-doped germanium by generation of defects via irradiation followed by subsequent characterization of electronic properties via deep-level transient spectroscopy (DLTS). Cobalt-60 gamma rays were used to generate isolated vacancies and interstitials which diffuse and react with impurities in the material to form four defect states (E_{37}, E_{30}, E_{22}, and E_{21}) in the upper half of the bandgap. Irradiations at 77 K and 300 K as well as isothermal anneals were performed to characterize the relationships between the four observable defects. E_{37} is assigned to the Sb donor-vacancy associate (E-center) and is the only vacancy containing defect giving an estimate of $2 \times 10^{11}\,\mathrm{cm}^{-3}\,\mathrm{Mrad}^{-1}$ for the uncorrelated vacancy-interstitial pair introduction rate. E_{37} decays by dissociation and vacancy diffusion to a sink present in a concentration of $10^{12}\,\mathrm{cm}^{-3}$. The remaining three defect states are interstitial associates and transform among one another. Conversion ratios between E_{22}, E_{21}, and E_{30} indicate that E_{22} likely contains two interstitials. The formation behavior of E_{22} after irradiation in liquid nitrogen indicates that E_{30} is required for formation of E_{22}. Eight defect states previously unseen after gamma irradiation were observed and characterized after irradiation by alpha and neutron sources. Their absence after gamma irradiation indicates that defect formation requires collision cascades.

We demonstrate electrically pumped lasing from Ge epitaxially grown on Si. Lasing is observed over a ~200 nm bandwidth showing that this system holds promise for low-cost on-chip communications applications via silicon microphotonics. The observed large threshold currents are determined to be largely a result of recombination due to threading dislocations. We estimate that recombination by threading dislocations becomes negligible when threading dislocation density is $\lesssim 4 \times 10^{6}\,\mathrm{cm}^{-2}$.

We developed a process for incorporation of colloidal quantum dots (QD) into a chalcogenide glass (ChG) matrix via solution based processing in common solvents. Observation of photoluminescence (PL) comparable to QD/polymethyl methacrylate (PMMA) films shows potential for this material to form the basis for low cost light sources which can be integrated with ChG microphotonic systems.

We investigated the impact of surface recombination on the benefit of combining a singlet fission material (tetracene) with a Si solar cell. Our simulations show that for efficiency gains, surface recombination velocity (SRV) for the tetracene/silicon interface must be less than $10^{4}\,\mathrm{cm\,s}^{-1}$. Characterization via radio frequency photoconductivity decay (RFPCD) measurements show that tetracene does not provide a sufficient level of passivation thus

requiring another material which passivates the interface. Using thin films fabricated by atomic layer deposition (ALD), we showed the first direct evidence of triplet energy transfer to Si via magnetic field effect (MFE) PL measurements.

Thesis Supervisor: Lionel C. Kimerling
Title: Thomas Lord Professor of Materials Science and Engineering

Thesis Supervisor: Anuradha M. Agarwal
Title: Principal Research Scientist, Materials Processing Center

For Mom and Dad

Acknowledgments

This work would not have been possible without generous support from many people. First and foremost, I must thank my advisors, Prof. Kimerling and Dr. Agarwal, who have taught me more than I could have imagined when I started graduate school. I have become a much better researcher due to their great mentorship. I was also fortunate to work with Dr. Michel who provided valuable guidance and advice for the setup of various experimental apparatuses. Together, Kim, Anu, and Jurgen have formed a fantastic research environment within EMAT.

Every EMAT student and postdoc past and present has been a pleasure to work with and I owe all of them thanks. Especially Corentin Monmeyran, who was my partner in studying germanium defects. In addition, the many conversations with Vivek Singh, Rodolfo Camacho-Aguilera, Zhaohong Han, Brian Albert, and Timothy Zens made our office an enjoyable space to work. I'd also like to apologize to Brian Pearson and the Fitzgerald group for treating their office as a break room.

I also want to thank the numerous collaborators I've been fortunate enough to work with over the years: Dr. Marco Romagnoli, Prof. Kazumi Wada, Stefano Grillanda, Davide Bianchi, Prof. Kathleen Richardson and her students (David Musgraves, Spencer Novak, Jacklyn Wilkinson), Prof. Clara Dimas, Prof. Moungi Bawendi and his students (Jennifer Scherer, Scott Geyer), and Prof. Marc Baldo and his students (Dan Congreve, Markus Einzinger, Tony Wu). I am also indebted to the many staff members at MIT's shared facilities, especially Kurt Broderick and Bernard Alamariu. I've also benefited greatly from the awe-inspiring DIY skills of David Bono and Dr. Piotr Becla.

My time at MIT has been very enjoyable largely due to the support of friends. I especially owe thanks to DMSE classmates Dan Harris, Adam Jandl, Jocelyn Newhouse, Max Solar, and Brian Spatocco for their continued camaraderie. Thanks to Ryan Iutzi for (almost) never saying no to a ski trip.

Finally, I want to thank my family for their love and encouragement over the years. This thesis would not exist without the curiosity and confidence they instilled in me.

Contents

List of Figures

List of Tables

Chapter 1

Introduction

Optoelectronic components perform conversions between optical and electrical energy and are used to generate (e.g., lasers and LEDs), control (e.g., optical modulators), and detect (e.g., photodiodes and CCDs) light. In recent years, optoelectronics have had a surge in interest due to the increasing importance of optoelectronics for computing applications. Advances in computing have largely been a result of reductions in component sizes within integrated circuits over time. As this process moves components to even smaller dimensions, electrical interconnects become a bottleneck to increased performance [1]. Optical communications via optoelectronic devices and fiber optics have allowed for the transmission of data over long distances with high bandwidth. As bottlenecks in electronic circuit scaling become more problematic, using optical communications on shorter length scales becomes necessary for increased performance scaling. Integration of electronics with microphotonic optoelectronic interconnect systems can provide higher bandwidth density, lower energy costs, and increased resistance to electromagnetic interference [2]. For use in practical applications, the fabrication of microphotonic components must be compatible with CMOS process flows. The obvious materials choice for building a microphotonic platform is silicon due to its ubiquity in the microelectronics industry. High volume fabrication processes methods developed by the semiconductor industry can be leveraged for high volume integration of silicon photonics with silicon microelectronics at low cost [3]. In addition to improved computing scaling, integrated optoelectronics also have applications in a variety of other fields such as imaging [4] and chemical/biological species sensing [5].

Optoelectronic devices are minority carrier devices and whose operation is strongly influenced by recombination and generation processes which are dominated in germanium (Ge) and silicon (Si) by defects. Chapter 2 briefly introduces semiconductor concepts relevant to understanding the impact of defects on optoelectronic applications. Of particular importance is understanding the influence of defect related trap states on carrier recombination-generation processes. In this thesis, we look at a few systems where understanding various material defects are beneficial for improving optoelectronic performance.

Chapter 3 focuses on the characterization of point defects in germanium. Germanium forms the basis for mature modulator and photodetector technologies and shows potential for development of a Si photonics monolithically integrated light source. Many of the photodetectors used in long-range telecom systems and mid-range data centers are

germanium-based. Even though germanium was used for many of the first semiconductor studies and devices, it has largely been supplanted by silicon for microelectronics applications. However, germanium has recently seen renewed interest partially due to the surge in Si photonics for which germanium provides a CMOS-compatible active material which can be integrated with passive Si photonic components. In addition, the high hole mobilities of germanium have renewed interest in developing Ge computing circuits as silicon devices start to approach theoretical limits. Compared to silicon, relatively little is understood about point defect states in germanium which act as generation-recombination centers and limit the performance of devices. We use a variety of radiation sources to generate vacancies and interstitials in germanium. The generated vacancies and interstitials diffuse and react with each other or impurities resulting in the formation of stable defect associates which we characterize by deep-level transient spectroscopy (DLTS). Annealing studies were also performed to determine the kinetics of various defect reactions. Electronic characterization (from DLTS) together with the reaction kinetics are analyzed in order to make tentative assignments for the identity of some defect states.

Out of all the components in a microphotonic circuit, fabrication of an integrated light source currently poses the largest challenge. Chapter 4 shows successfully demonstration of electrically pumped lasing from germanium. This system provides a monolithically integrable solution for a Si photonics compatible light source for optical interconnect applications. Germanium is epitaxially grown on silicon with tensile strain and is highly n-type doped in order to engineering the bandgap to be pseudo-direct. Heteroepitaxy of Ge-on-Si requires relaxation of strain through nucleation of dislocations which become the dominant defect in this system. Threshold current densities for our Ge lasers are approximately two orders of magnitude greater than for traditional III-V laser diodes. In order to understand the observed behavior, we develop a model to determine the impact of recombination at dislocations on laser performance.

Chapter 5 investigates a potential materials system for fabrication of substrate-independent integrated light sources. We develop the processes needed to solution process colloidal quantum dot (QD) chalcogenide glass (ChG) composite thin films by investigating the interface between QD surfaces and the ChG matrix. This system provides a wide bandwidth, substrate independent platform for developing light sources that can be integrated easily with ChG-based optical sensor microphotonic systems.

Chapter 6 focuses on investigating the transfer of triplet exciton energy from tetracene to silicon. Due to increasing worry about the impact of CO_2 emissions from burning fossil fuels, photovoltaics are another optoelectronic application that have seen a recent surge in interest. Even though silicon has a bandgap close to ideal for a single junction cell, due to theoretical limitations, the overall efficiency for a silicon solar cell is limited to ~32 %. A significant portion of the incident solar energy is lost by thermalization of carriers generated by photons with energies greater than the bandgap. Tetracene is an organic semiconductor material which can absorb high energy photons to generate singlet excitons. These singlet excitons can undergo singlet exciton fission to generated two triplet excitons with approximately half the energy. If that energy from the two triplet excitons can be efficiently transfered to a silicon solar cell to generate two electron-hole pairs, this would effectively double the photocurrent from high energy photons. An important factor in determining whether a practical increase in efficiency can be gained is the interface between silicon and tetracene. We model what

surface recombination velocities are required for transfer to be useful assuming that transfer of energy from tetracene to silicon places carriers closer to the surface than they would be in a traditional cell design. We also experimentally investigate and demonstrate transfer of triplet exciton energy to silicon which has not previously been conclusively shown to occur. Experimental characterization of recombination at the interface between silicon and tetracene is crucial to understanding and improving energy transfer. We use contactless radio frequency photoconductivity decay (RFPCD) measurements to quickly characterize the quality of interfaces and also develop a methodology for observing transfer of energy from tetracene to silicon (via RFPCD).

Chapter 7 summarizes the key accomplishments of the work presented in this thesis.

Chapter 2

Semiconductor Concepts

2.1 Carrier Generation and Recombination

When a semiconductor is in thermal equilibrium, a dynamic balance between generation and recombination of carriers is present. Electrons and holes are continuously being generated and are also recombining to annihilate each other. Generation and recombination occurs through the following mechanisms (Figure 2-1):

1. Thermal band-to-band generation/recombination
2. Optical band-to-band generation/recombination
3. Auger generation/recombination
4. Trap-assisted generation/recombination

A semiconductor is in thermal equilibrium when there is no exchange of energy outside the system and the system is in steady state. Under these conditions, the following balance is established:

$$G = R \tag{2.1}$$

where G is the generation rate (number of electron-hole pairs created per unit volume per time, $\mathrm{cm}^{-3}\,\mathrm{s}^{-1}$) and R is the recombination rate (number of electron-hole recombination events per unit volume per time, $\mathrm{cm}^{-3}\,\mathrm{s}^{-1}$). Because multiple pathways are present for generation and recombination, the overall generation and recombination rates are the sum of the individual rates. Moreover, the existence of multiple pathways requires that the system satisfy the principle of detailed balance in thermal equilibrium which states that the rates of a process and its inverse must equal and balance in detail:

$$G_i = R_i \qquad \text{for all } i \tag{2.2}$$

where the subscript i indicates a specific generation/recombination mechanism.

2.1.1 Carrier Lifetimes

For semiconductors, the carrier lifetime can refer to both the generation lifetime and the recombination lifetime. These parameters are most relevant outside of equilibrium

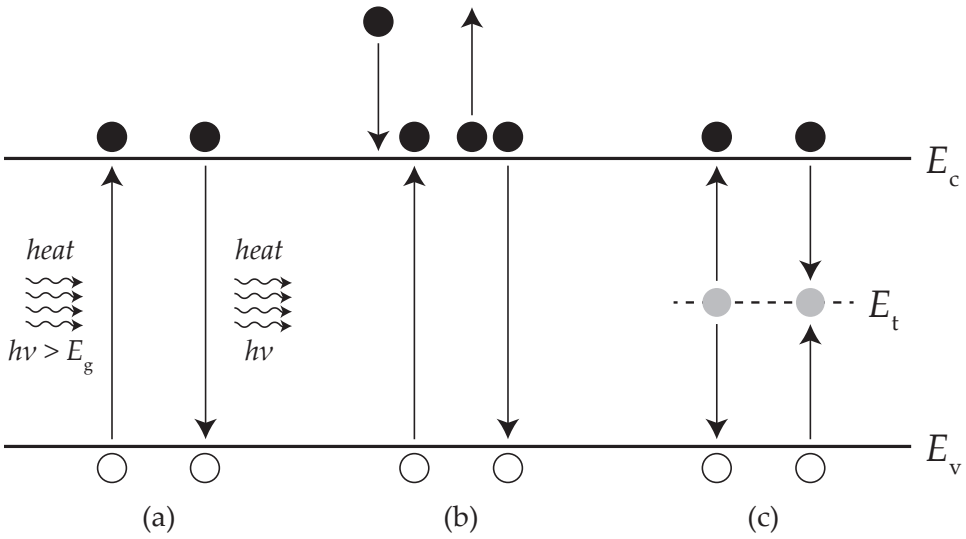

Figure 2-1: Generation and recombination mechanisms: (a) Thermal/optical band-to-band, (b) Auger, and (c) Trap-assisted.

conditions. While the rates of generation and recombination must equal each other in thermal equilibrium, they are not required to be equal when the semiconductor is removed from thermal equilibrium as the result of external influence. Carrier concentrations can be perturbed from their equilibrium values by either being generated in excess (e.g., through illumination or injection) or being extracted (e.g., as in the depletion region of a semiconductor diode). When carriers are generated in excess, carrier concentrations are described by

$$n = n_0 + \Delta n \tag{2.3}$$

$$p = p_0 + \Delta p \tag{2.4}$$

where n_0 and p_0 are the equilibrium electron and hole concentrations and Δn and Δp are the excess electron and hole concentrations. Even outside of thermal equilibrium, charge neutrality is still satisfied outside of thermal equilibrium meaning that $\Delta n \simeq \Delta p$. In this scenario, the generation rate will remain mostly unaffected if the number of excess carriers is not too great and the temperature is unchanged. However, the increased number of electrons and holes will make it more likely for them to recombine increasing the recombination rate. The imbalance between the generation and recombination rates can be used to define the net recombination rate:

$$U = R - G \tag{2.5}$$

where the total net recombination rate is the sum of net recombination rates due to each recombination mechanism (e.g., radiative band-to-band recombination, Auger recombination,

and trap-assisted recombination):

$$U = \sum U_i = U_{\text{rad}} + U_{\text{Auger}} + U_{\text{trap}}. \tag{2.6}$$

Under low-level injection conditions (for n-type and p-type materials):

$$p_0 \ll \Delta n \simeq \Delta p \ll n_0, \qquad \text{n-type} \tag{2.7}$$

$$n_0 \ll \Delta n \simeq \Delta p \ll p_0, \qquad \text{p-type} \tag{2.8}$$

the total net recombination rate follows the form of

$$U \simeq \frac{\Delta n}{\tau_{\text{r}}} \tag{2.9}$$

where τ_{r} is the recombination lifetime which is a characteristic of the material and gives an indication of the average time an excess electron-hole pair will last before recombination. In extrinsic semiconductors, the recombination lifetime is also referred to as the minority carrier lifetime. Similar to the net recombination rate, the overall recombination lifetime is the result of contributions from various mechanisms:

$$\frac{1}{\tau_{\text{r}}} = \sum \frac{1}{\tau_i} = \frac{1}{\tau_{\text{rad}}} + \frac{1}{\tau_{\text{Auger}}} + \frac{1}{\tau_{\text{trap}}}. \tag{2.10}$$

Thus, the overall recombination lifetime is dominated by the mechanism with the shortest lifetime.

When carriers are extracted ($n, p \ll n_{\text{i}}$), the reduction in electron and hole concentrations reduces the recombination rate. Therefore, there is now a net generation rate of electron-hole pairs in the material. A similar characteristic time can be obtained which is called the generation lifetime, τ_{g}. It is important to not confuse the recombination lifetime with the generation lifetime as the two are not equivalent for the same material.

2.1.2 Generation/Recombination Mechanisms

Thermal Band-to-band Generation/Recombination

In these processes, heat in the form of phonons is either consumed in order to break bonds or is released to the surroundings when bonds are formed. Both of these processes are rare in typical semiconductors. The maximum phonon energy (~50 meV) for most materials is many times smaller than the bandgap energy (~1 eV). This requires that many phonons be simultaneously involved during thermal band-to-band generation and recombination events which is statistically unlikely.

Optical Band-to-band Generation/Recombination

In these processes, energy in the form of photons is either consumed (optical absorption) in order to break bonds or is released to the surroundings (radiative recombination) when bonds are formed. These processes are extremely important for many optoelectronic applications. Generation of carriers by optical absorption is the process by which photodetectors

and photovoltaic cells operate. Light emission by radiative recombination is the process by which light emitting diodes (LEDs) and semiconductor diode lasers operate.

Because band-to-band processes require both conservation of energy and momentum, the rate of optical band-to-band processes can vary greatly depending on whether the material has a direct or indirect bandgap. In direct bandgap materials, conservation of momentum is easily satisfied for band-to-band transisitions. Therefore, the rates of these processes can be quite large in direct bandgap materials. However, in indirect bandgap materials (such as Si and Ge), a phonon is required in order to satisfy momentum conservation during band-to-band transitions. Therefore, the rates of optical generation and recombination processes are much smaller in indirect bandgap materials than in direct bandgap materials.

Generation produces carriers by the breaking of bonds and is therefore dependent on the number of available bonds in the material. Practically speaking, this supply can be considered to be unlimited. Recombination on the other hand requires the presence of free electrons and holes and thus depends on the carrier concentrations. Outside of the equilibrium conditions, the net reaction rates are described by

$$-U_{\text{rad}} = G_{\text{rad}} - R_{\text{rad}} \simeq k_{\text{rad}} n_{\text{i}}^2 \qquad \text{extracted carriers} \qquad (2.11)$$

$$U_{\text{rad}} = R_{\text{rad}} - G_{\text{rad}} = k_{\text{rad}} \left(np - n_0 p_0 \right) \qquad \text{excess carriers} \qquad (2.12)$$

where k_{rad} is a temperature dependent reaction rate constant characteristic of the material. This relationship shows that the net recombination rate is proportional to the excess np product.

Auger Generation/Recombination

Auger processes involve "hot" carriers which have large kinetic energy. Auger generation occurs when carriers transfer some of their excess kinetic energy to a bond, thereby breaking it and generating an electron-hole pair. Auger recombination occurs when a recombination event transfers the energy released from electron-hole recombination to a third carrier (which now has excess kinetic energy). Because Auger recombination requires a third carrier, it is typically an unlikely recombination mechanism. However, when the concentration of carriers is large (for heavily-doped semiconductors or under carrier injection conditions), the probability of Auger recombination occurring increases potentially making this an important recombination pathway.

Unlike band-to-band generation, the supply of reactants cannot be considered unlimited. Because the probability of a carrier containing sufficient energy for Auger processes increases with carrier concentration, the Auger generation rate is proportional to the relevant carrier concentration. The Auger recombination rate requires three carriers and is thus proportional to the square of the relevant carrier concentration times the concentration of the complementary carrier. For a Auger processes, the net reaction rates are described by

$$-U_{\text{Auger}} = \left(k_{\text{he}} n + k_{\text{hh}} p \right) n_{\text{i}}^2 \qquad \text{extracted carriers} \qquad (2.13)$$

$$U_{\text{Auger}} = \left(k_{\text{he}} n + k_{\text{hh}} p \right) \left(np - n_0 p_0 \right) \qquad \text{excess carriers} \qquad (2.14)$$

where k_{he} and k_{hh} are temperature dependent reaction rate constants characteristic of the material for hot-electron and hot-hole processes, respectively. Similar to band-to-band processes, the net recombination rate is proportional to the excess np product. Auger generation under extracted carrier conditions is extremely unlikely due to the lack of carriers.

Trap-assisted (SRH) Generation/Recombination

Defects within the semiconductor material can produce trap states (Section 2.2) which can greatly enhance thermal generation and recombination of carriers. These processes are also referred to as Shockley-Read-Hall (SRH) processes based on the models developed by Shockley and Read [6] and Hall [7, 8]. During trap-assisted recombination, one carrier type can become "trapped" at a localized site until the complementary carrier is present making it much more likely that recombination will occur. This is particularly important in indirect bandgap materials because while the trap site is localized in the lattice, it is delocalized in k-space making it easier to satisfy momentum conservation. In addition, compared to band-to-band processes, trap-assisted processes require substantially less energy. In fact, this is typically the most dominant mechanism for generation and recombination in microelectronic devices. For trap-assisted processes, the net recombination reaction rate is described by

$$U_{\text{trap}} = \frac{np - n_{\text{i}}^2}{\frac{1}{\sigma_{\text{p}}\langle v_{\text{p}}\rangle N_{\text{t}}}\left(n + n_{\text{i}} \exp\frac{E_{\text{t}}-E_{\text{i}}}{kT}\right) + \frac{1}{\sigma_{\text{n}}\langle v_{\text{n}}\rangle N_{\text{t}}}\left(p + n_{\text{i}} \exp\frac{E_{\text{i}}-E_{\text{t}}}{kT}\right)} \tag{2.15}$$

where σ_{n} and σ_{p} are the capture cross sections for electrons and holes, n_{i} is the intrinsic carrier concentration, N_{t} is the number of trap states, E_{t} is the energy of the trap level, E_{i} is the intrinsic Fermi level and $\langle v_{\text{n,p}}\rangle$ is the mean thermal velocity of carriers given by

$$\langle v_{\text{n,p}}\rangle = \sqrt{\frac{3kT}{m^*_{\text{n,p}}}} \tag{2.16}$$

where $m^*_{\text{n,p}}$ is the effective mass of conductivity for the relevant carrier.

2.2 Semiconductor Defects

Semiconductor electronic properties are determined by the band structure which is related to the crystal structure. Crystallographic lattice defects are perturbations to the structure which in turn modify in the band structure altering the properties of the material. Because defects have a large impact on the properties of the material, understanding their behavior is crucial. The inclusion of a small number of defects is thermodynamically favorable and unavoidable. For almost all semiconductor applications, defects are intentionally introduced in the form of dopants. In addition, deleterious defects are often inadvertently introduced during fabrication and processing limiting device performance. Therefore, knowledge of defects and how they impact properties can be used to both reduce device degradation and

engineer the properties of a material and open up uses for new applications. Lattice defects can be classified based on their dimensionality into the following groups:

1. Zero-Dimensional Defects (Point Defects)
2. One-Dimensional Defects (Dislocations)
3. Two-Dimensional Defects (Surfaces, Grain Boundaries, Stacking Faults, etc.)
4. Three-Dimensional Defects (Clusters, Precipitates, Voids, etc.)

A few of the defect types most relevant to this thesis will be described in the following sections:

2.2.1 Point Defects

Zero-dimensional defects involve atomic-sized perturbations from the ideal lattice and are often referred to as point defects. Within this classification there are a variety of defect types (Figure 2-2). A vacancy is the absence of an atom from a lattice site. An interstitial is an atom which is located at a site which is not part of the host lattice. Interstitials can either be composed from an atom of the host material (self-interstitial) or from an impurity atom. Impurity atoms can also be located at lattice sites forming substitutional defects. Semiconductor carrier concentrations are often precisely controlled by introduction of substitutional impurities with one greater or one fewer valence electron (acceptors and donors). These defects can also react with each other to form defect associates (also referred to as defect complexes) such as di-interstitials or vacancy-donor associates.

Point defects are a large focus of this thesis due to the impact (Section 2.3.1) of the bandgap states they generate. These states can be further classified as either shallow states or deep states:

Shallow States

Point defect states are often divided into two categories: shallow states (ionization energies $\lessapprox 50\,\text{meV}$) and deep states (ionization energies $\gtrapprox 50\,\text{meV}$). Shallow states form levels close to the relevant band edges (valence band for acceptors and conduction band for donors) and are sometimes referred to as hydrogenic defect states because they form levels similar to that of a hydrogen atom. However, the energy levels are modified since the hydrogen-like impurities are contained in a crystalline material . A modified Rydberg binding energy can be calculated by accounting for dielectric screening by the host and using the effective mass of the relevant band edge:

$$E = \frac{m^*}{m_\text{e}\varepsilon_\text{r}^2} \cdot \frac{13.6}{n^2}\ \text{eV} \tag{2.17}$$

where m^* is the effective mass of the carrier, m_e is the electron rest mass, ε_r is the relative permittivity (dielectric constant), and n is the principle quantum number. Similar to a hydrogen atom, carriers are weakly bound by a Coulombic potential. An analogous Bohr radius can be calculated and is typically equal to several lattice spacings:

$$a_\text{B} = \varepsilon_\text{r}\frac{m_\text{e}}{m^*}a_0 \tag{2.18}$$

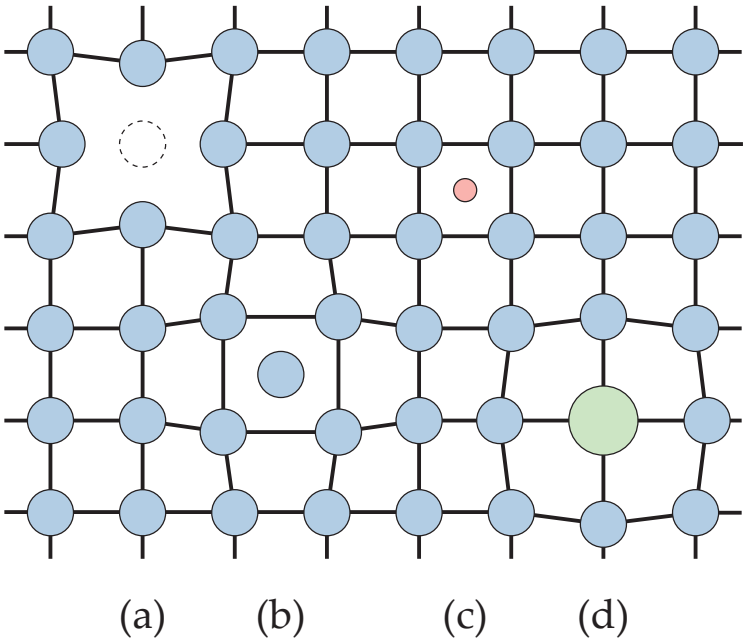

Figure 2-2: Schematic of point defect types: (a) Vacancies, (b) Self-interstitials, (c) Interstitial impurities, and (d) Substitutional impurities.

where a_0 is the hydrogen atom Bohr radius. These states are often generated by substitutional impurities which contain either one greater or one fewer valence electron than the replaced atom. Substitutional dopants are often added to generate shallow states whose levels are ionized at room temperature, thus providing additional carriers for conduction.

Deep States

Deep states, on the other hand, are strongly localized, tightly bound carriers, and have energy levels which lie deeper within the band gap. Large concentrations of deep states can effect carrier concentrations through compensation of acceptors and donors. However, even small concentrations of deep states can determine the overall carrier recombination lifetime of the material through trap-assisted/SRH recombination. Compared to shallow defect states, defects generating deep states distort the host lattice to a greater extent. Therefore, calculating defect energies from first principles becomes much more difficult and requires many atoms around the defect to be considered [9].

Defect centers which generate deep states can become occupied by more than a single electron and exist in several charge states. Figure 2-3 shows a schematic energy level diagram for a multivalent defect center. In this example scenario, the defect center generates three trap levels (E_{t1}, E_{t2}, and E_{t3}) and can exist in four charge states: doubly positively charged (++), positively charged (+), neutral (○), and negatively charged (−). Each trap level corresponds to a transition in charge state of the defect center. Equilibrium occupation of

trap levels is determined by the Fermi level of the material. When the Fermi level is below E_{t1}, the defect centers are unoccupied and the charge state is doubly positive. As the Fermi level moves up above E_{t2}, the defect centers become occupied by a single electron and are positively charged. Depending on the difference between the Fermi level and the next trap level, some fraction of the defect centers may be occupied by a second electron and become neutral. Similarly, once the Fermi level moves above E_{t2} and E_{t3}, the defect centers all become occupied by two electrons (neutral charge) and three electrons (negatively charged), respectively. Some trap levels can be classified as either donor-like or acceptor-like states based on their similarity to dopant behavior. Donor-like states are positively charged when unoccupied (e.g., E_{t2}) and acceptor-like states are negatively charged when occupied (e.g., E_{t3}). The specific charge states observed for various electron occupations were arbitrarily chosen for this example and are not universally true for all multivalent defect centers.

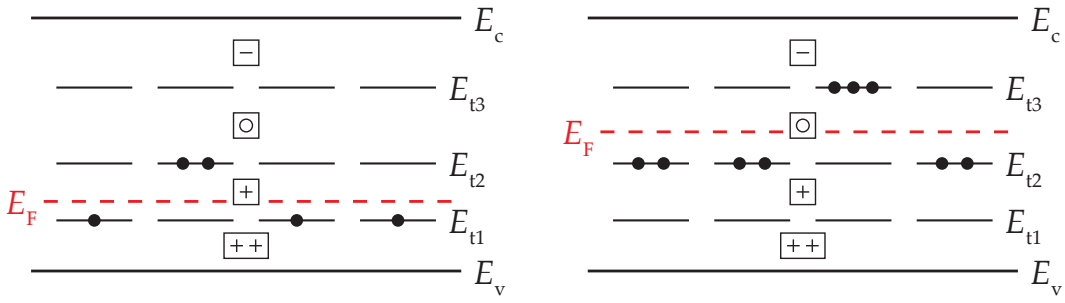

Figure 2-3: Schematic energy level diagram for a multivalent defect center showing occupation of trap levels for different Fermi level positions. *Reproduced from [10]*

2.2.2 Dislocations

Similar to point defects, dislocations can introduce energy states (either localized levels or bands) into the bandgap impacting carrier lifetimes. Compared to point defects, the underlying mechanisms behind electrical and optical effects of dislocations can be more complex and are often influenced by point defects and impurities. A detailed summary of these mechanisms can be found in [11]. The original Shockley model predicted that dislocations contain dangling bonds within their cores whose wavefunctions would overlap forming a band. However, experimental results show a relatively small number of electrically active sites along the length of a dislocation indicating that dislocations bond rearrangement eliminates the majority of dangling bonds. Instead, defect states are generated at specific sites along the dislocation such as kinks or point defect associates. Moreover, under high injection conditions (common for LEDs and lasers), recombination at dislocations can enhance their motion and growth quickly leading to "dark line defects" and device failure [12, 13].

Dislocations can be a dominant defect in applications requiring epitaxy of multiple materials with different lattice constants. Misfit dislocation segments nucleate at the interface between materials to relieve strain [14]. The misfit dislocations are localized to the

interface but can still impact the active region because segments can "thread" up through the material and create threading dislocations in the active device region (Figure 2-4).

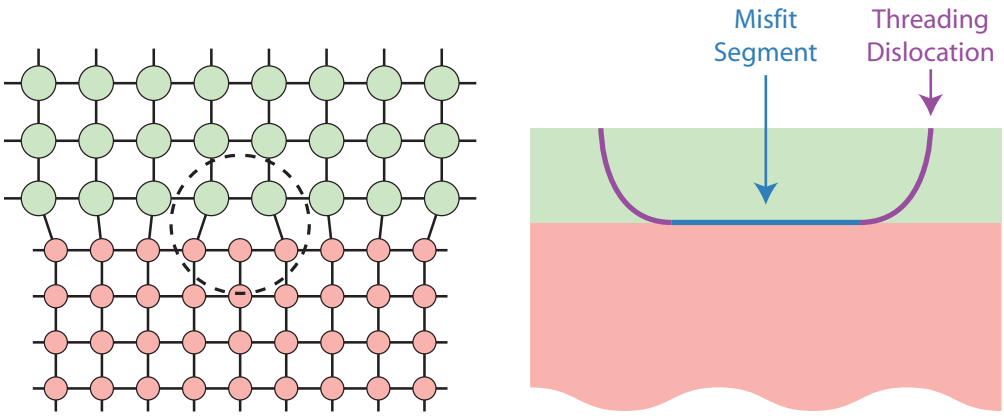

(a) (b)

Figure 2-4: Schematic of dislocations formed during heteroepitaxy: (a) Close view of interface illustrating how misfit dislocations relieve the strain between materials with dissimilar lattice constants; (b) Illustration of threading dislocations nucleated from misfit segments which extend throughout the film to the surface.

2.2.3 Surfaces and Interfaces

Surfaces and interfaces are large lattice disruptions that act as recombination-generation centers in a similar way as bulk defects through the SRH model. Surface recombination is most commonly characterized by S, the surface recombination velocity (SRV) which has the same dimensionality as velocity. This allows for a construction of an expression similar to Equation 2.9, relating a recombination rate per unit area (U_s) to the excess carrier density near the surface:

$$U_s = S\Delta n \tag{2.19}$$

where U_s can be interpreted as a flux due to Δn carriers traveling at a velocity S towards the surface where they recombine. Equation 2.19 is a presented to give a more intuitive definition of SRV. In reality, SRV is defined by a boundary condition for the 1-D diffusion equation for carriers assuming no applied electric fields:

$$\frac{\partial \Delta n(x,t)}{\partial t} = D\frac{\partial^2 \Delta n(x,t)}{\partial x^2} + G(x,t) - \frac{\Delta n(x,t)}{\tau_{\text{bulk}}} \tag{2.20}$$

where D is the carrier diffusion coefficient and τ_{bulk} is the lifetime composed of components related to recombination in the bulk (Equation 2.10). The SRV, S, is then defined by the

following boundary condition (in steady-state, $\frac{\partial n}{\partial t} = 0$)

$$D \left. \frac{\mathrm{d}\Delta n(x)}{\mathrm{d}x} \right|_{x=0} = S\Delta n(x=0). \tag{2.21}$$

When surfaces contribute to recombination, is it useful to describe an effective recombination lifetime which includes bulk and surface lifetime, τ_{surf}, components:

$$\frac{1}{\tau_{\mathrm{eff}}} = \frac{1}{\tau_{\mathrm{bulk}}} + \frac{1}{\tau_{\mathrm{surf}}} \tag{2.22}$$

where τ_{surf} is related to S by

$$\frac{1}{\tau_{\mathrm{surf}}} = \beta^2 D \tag{2.23}$$

where β can be obtained from a solution of

$$\beta \tan\left(\frac{\beta d}{2}\right) = \frac{S}{D} \tag{2.24}$$

where d is the sample thickness [15]. It should be noted that this equation is derived for the condition that S for both front and back surfaces are equal. In the limits of low and high surface recombination velocity

$$\tau_{\mathrm{surf}}(S \to 0) = \frac{d}{2S} \tag{2.25}$$

$$\tau_{\mathrm{surf}}(S \to \infty) = \frac{d^2}{\pi^2 D}. \tag{2.26}$$

If τ_{bulk} and S are both large, then the effective carrier lifetime reduces to Equation 2.26 meaning that the observed lifetime is simply the average time it takes for carriers to diffuse to the surface.

2.3 Dynamic Behavior of Deep Defect States

The dynamic electronic behavior of deep states are controlled by four competing processes (Figure 2-5):

1. Electron emission into the conduction band (e_{n})
2. Electron capture into non-occupied deep states (c_{n})
3. Hole capture into electron occupied deep states (c_{p})
4. Hole emission into the valence band (e_{p})

Electrons are emitted from and holes are captured at n_{t} sites occupied by electrons while holes are emitted from and electrons are captured at $(N_{\mathrm{t}} - n_{\mathrm{t}})$ unoccupied sites. Thus, the rate of change of electron occupancy at a defect state is

$$\frac{\mathrm{d}n_{\mathrm{t}}}{\mathrm{d}t} = (e_{\mathrm{p}} + c_{\mathrm{n}})(N_{\mathrm{t}} - n_{\mathrm{t}}) - (e_{\mathrm{n}} + c_{\mathrm{p}})n_{\mathrm{t}} \tag{2.27}$$

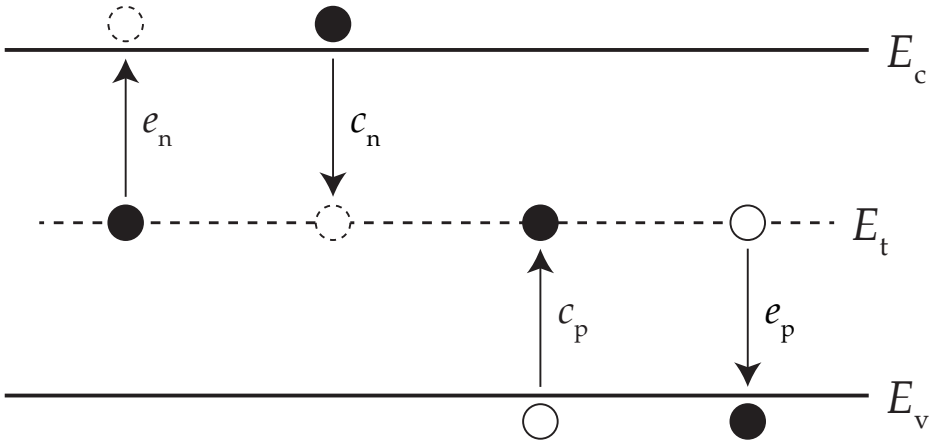

Figure 2-5: Competeing emission (e) and capture (c) process for electrons (n) and holes (p) at a defect state (E_t) within the bandgap.

where n_t is the number of occupied states, N_t is the total concentration of deep states, c_n and c_p are the capture rates for electrons and holes, and e_n and e_p are the emission rates for electrons and holes. The capture rates c_n and c_p are described by

$$c_n = \sigma_n \langle v_n \rangle n, \tag{2.28}$$

$$c_p = \sigma_p \langle v_p \rangle p. \tag{2.29}$$

Electron and hole concentrations for non-degenerate semiconductors are

$$n = N_c \exp\left(-\frac{E_c - E_F}{kT}\right) \tag{2.30}$$

$$p = N_v \exp\left(-\frac{E_F - E_v}{kT}\right) \tag{2.31}$$

where N_c is the effective density of states in the conduction band, N_v is the effective density of states in the valence band, E_c is the conduction band edge, E_v is the valence band edge, and E_F is the Fermi level.

The relative magnitudes of capture rates can be used to categorize defect states. If the capture rate for one carrier type is much larger than for the other type, then the defect can be classified as a trap state. If instead they are both large and of comparable magnitude, then the defect can be classified as a recombination center. However, a specific defect state could be classified as both a trap state and recombination state depending on the carrier concentrations. When a defect state is located within the depletion region of a diode, regardless of the magnitude of the capture cross section, the capture rates are very small due to low carrier concentrations. In that situation, all defect states could be classified as

trap states.

Defects can also be categorized by their emission rates when under depletion conditions. When the emission rate of the majority carrier is greater than the minority carrier, the defect is classified as a majority carrier trap. Similarly, when the emission rate of the minority carrier is greater than the majority carrier, the defect is classified as a minority carrier trap. In addition, defects are often labeled as either electron traps ($e_n > e_p$) or hole traps ($e_p > e_n$). Defects can also be classified as generation centers when the emission rates are roughly equal ($e_n \sim e_p$).

In thermal equilibrium, capture and emission processes must obey the principle of detailed balance. The rates of emission and capture for electrons must be equal. Similarly, the rates of emission and capture for holes must also be equal. Steady state trap occupancy, $\frac{dn_t}{dt} = 0$, is not a sufficient condition for equilibrium because, without detailed balance, it is possible for there to be a net transfer of carriers from one band to the other. Detailed balance thus requires

$$e_n n_t = c_n(N_t - n_t) \tag{2.32}$$

and

$$e_p(N_t - n_t) = c_p n_t. \tag{2.33}$$

Therefore, the occupancy of a defect state in thermal equilibrium can be written as a function of the emission and capture rates:

$$\frac{n_t}{N_t} = \frac{c_n}{e_n + c_n} = \frac{e_p}{c_p + e_p}. \tag{2.34}$$

Because electrons obey Fermi-Dirac statistics, the occupancy of a defect state with energy E_t in thermal equilibrium can also be described by a Fermi-Dirac distribution function:

$$\frac{n_t}{N_t} = \left[1 + \frac{g_0}{g_1}\exp\left(\frac{E_t - E_F}{kT}\right)\right]^{-1} \tag{2.35}$$

where g_0 and g_1 are degeneracies of the state when emptied and filled, respectively. Relationships between the emission rate and the capture rate in thermal equilibrium can be found by combining Equation 2.34 with Equation 2.35:

$$\frac{e_n}{c_n} = \frac{g_0}{g_1}\exp\left(\frac{E_t - E_F}{kT}\right) \tag{2.36}$$

$$\frac{e_p}{c_p} = \frac{g_1}{g_0}\exp\left(\frac{E_F - E_t}{kT}\right). \tag{2.37}$$

An expression for the electron emission rate can be obtained by substituting Equation 2.28 and Equation 2.30 into Equation 2.36:

$$e_n(T) = \sigma_n\langle v_n\rangle\frac{g_0}{g_1}N_c\exp\left(-\frac{E_c - E_t}{kT}\right). \tag{2.38}$$

A similar expression for the hole emission rate can be obtained by substituting Equation 2.29

and Equation 2.31 into Equation 2.37:

$$e_{\mathrm{p}}(T) = \sigma_{\mathrm{p}}\langle v_{\mathrm{p}}\rangle \frac{g_1}{g_0} N_{\mathrm{v}} \exp\left(-\frac{E_{\mathrm{t}} - E_{\mathrm{v}}}{kT}\right). \tag{2.39}$$

We can see that for trap states located in the upper half of the bandgap, $e_{\mathrm{n}} > e_{\mathrm{p}}$, and for states in the lower half of the bandgap, $e_{\mathrm{p}} > e_{\mathrm{n}}$. Therefore, for an n-type material, majority carrier traps will be observed in the upper half of the bandgap while minority carrier traps will be observed in the lower half of the bandgap.

2.3.1 Impact of Defect States on Device Performance

As previously mentioned, defect states in the bandgap act as capture and emission centers for carriers. This primarily has two effects in semiconductors which can drastically affect the performance of electronic and optoelectronic devices:

1. Carrier Compensation
2. Carrier Generation-Recombination

Carrier compensation refers to a reduction in the free carrier concentration due to the presence of defect states. Typically, this is related to the capture of majority carriers (by deep states) or generation of minority carriers (by shallow states). In addition, free carrier concentrations can be compensated by formation of defect associates containing dopant atoms (e.g. vacancy binding with a phosphorus dopant atom) which are not ionized at room temperature. Because the resistivity, ρ, is related to carrier concentrations by

$$\rho = \frac{1}{q(\mu_{\mathrm{n}} n + \mu_{\mathrm{p}} p)} \tag{2.40}$$

where μ_{n} and μ_{p} are the mobilities for electrons and holes respectively, carrier compensation primarily has the effect of increasing the resistivity which can lead to a variety of issues in devices (e.g., increased RC delay, energy losses). However, intentional compensation via defect states can also be useful for applications requiring high resistivity material such as photoconductors. This can be achieved through addition of impurities and/or irradiation of the material. In most applications, carrier compensation is not an issue due to the high level of control of impurities in semiconductors. Because carriers are compensated by only one or two carriers per defect, impurities must be present in concentrations close to the dopant concentration to drastically alter the resistivity.

However, as previously mentioned, defect states can also mediate generation and recombination (through SRH processes) which can significantly alter carrier lifetimes even in below parts per billion defect concentrations. Defect states are particularly deleterious for optoelectronic applications which are all minority carrier devices. For a few specific applications, recombination and generation due to defect states largely results in the following:

- **Photodiodes:** The noise level and power dissipation is determined by the dark current (leakage current) due to diffusion of thermally generated minority carriers to

the junction. Defects which generate states near mid-gap can drastically lower the energy required to thermally generate carriers thus drastically increasing the dark current thereby decreasing signal/noise and increasing power consumption.

- **Light Sources:** Defect states increase competition of non-radiative recombination with radiative recombination lowering the quantum efficiency of emission. As we will discuss in further detail in Chapter 4, this can also lead to increased threshold currents for lasers.
- **Photovoltaics:** Electron-hole pairs generated in the depletion region of a photovoltaic cell are split by the junction and efficiently collected. In order for carriers generated outside of the depletion region to provide useful energy, minority carriers must diffuse to the junction before recombination. When defect states reduce carrier lifetimes, a larger fraction of carriers will recombination before diffusing to the junction thereby lowering the efficiency of cell.

Similar to carrier compensation, for some applications, it is desirable to reduce carrier lifetimes (e.g., high speed electronics) and impurities which introduce mid-gap states are intentionally added. It should be noted that this section only contains brief descriptions for some of the numerous effects that defect states have on semiconductor devices.

Chapter 3

Point Defects in Germanium

High carrier mobilities, compatibility with silicon processes, and a direct bandgap corresponding to a wavelength of 1.55 µm make germanium a strong candidate for the new generation of MOSFETs and as the active material in a variety of optoelectronic devices including photodetectors [17, 18] , modulators [19–21], and light sources (Chapter 4). However, the properties of point defects in germanium have not been investigated as thoroughly as those of silicon. This is partially a consequence of the limited success of electron paramagnetic resonance (EPR) studies in germanium due to its varied isotopic composition4 and large spin orbit coupling which yields a short spin-lattice relaxation time [22, 23]. In addition, knowledge of defects in silicon is not directly applicable to germanium, as was shown in SixGe1-x studies [24]. EPR currently does not provide direct identification of defects in germanium; therefore, identifications must be obtained through more indirect methods. In this work, we use ^{60}Co gamma, alpha, and neutron irradiation to generate vacancy and interstitial related defect associates in Sb-doped germanium which we characterize by deep-level transient spectroscopy (DLTS). Similar DLTS studies of defects in germanium have been performed in the past [25–33], however, as is often noted, there is little consensus and considerable scatter between different studies as to the properties and identification of previously observed defects. In conjunction with the analysis of defect state properties by DLTS, annealing studies were also performed to investigate the kinetics of various defect growth and decay reactions. Electronic characterization (from DLTS) together with the reaction kinetics are analyzed in order to make tentative assignments for the identity of some defect states.

3.1 Deep Level Transient Spectrocopy (DLTS)

Deep level transient spectroscopy (DLTS) is a technique for the characterization of electrically-active defect states developed in 1974 by Lang [34]. Using DLTS, defect state concentrations, energy levels, and capture cross sections can be measured giving complete characterization of the defect properties which ultimately affect device performance. In addition, compared to other analytical techniques, such as fourier transform infrared spectroscopy

The work in this chapter is partially adapted from [16] and was done in collaboration with C. Monmeyran, also a member of the Kimerling group at MIT.

(FTIR) and secondary ion mass spectroscopy (SIMS), DLTS has greater sensitivity to defect concentration. The detection limit for defect concentrations is $\sim 10^{-5}$ times the free carrier concentration allowing for measurement of defect concentrations as low as $10^9\,\mathrm{cm}^{-3}$ to $10^{10}\,\mathrm{cm}^{-3}$ in this work. The remainder of Section 3.1 contains an introduction to the theory and application of DLTS for the characterization of defect states in n-type material. For brevity and clarity, expressions relevant to the analysis of p-type materials will be omitted, however a similar process can be used to characterize defects in p-type materials via DLTS. More detailed descriptions of DLTS techniques can be found in a review by Miller et al. [35] and a book by Blood et al. [10].

3.1.1 Theory of Operation

Using DLTS, defects are characterized by observation of thermal emission of carriers from deep states within the depletion region of a diode by means of a capacitive transient. Emission of majority carriers from trap states increases the net positive space charge density in the depletion region of a semiconductor junction. If the diode is kept at constant voltage, the depletion region shrinks in response to the additional charge resulting in a measurable increase in the junction capacitance.

Schematics for an n-type Schottky diode under neutral and reverse biased conditions are shown in Figure 3-1. In the absence of a bias, trap states are occupied outside the depletion width x_0 because $E_\mathrm{F} > E_\mathrm{t}$ which leads to $c_\mathrm{n} > e_\mathrm{n}$ (Equation 2.36). When a reverse bias is applied, electrons are depleted for an extended distance x_d from the surface. The removal of free electrons halts the capture process and traps empty by thermal emission of electrons at a rate e_n described by Equation 2.38. This produces an exponential transient in the capacitance measured across the junction which can be described by

$$C(t) = C(\infty) + \Delta C \exp(-e_\mathrm{n} t) \tag{3.1}$$

where $C(\infty)$ is the steady state capacitance at reverse bias and ΔC is the difference in capacitance due to the emptying of traps which can be related to the concentration of trap states (Section 3.1.3.2).

During a DLTS measurement, the following voltage biasing steps are repeated to generate capacitance transients which correspond to thermal emission of carriers from traps (Figure 3-2):

1. The diode is held in reverse bias which sweeps carriers out of the depletion region and empties traps.
2. The diode is pulsed forward which reduces the depletion region and fills traps with carriers.
3. The diode is put back into reverse bias after the pulse. Free carriers are swept out of the depletion region and capture of carriers by traps is halted.
4. Capacitance transient is observed as traps empty due to thermal emission of carriers.

Often an observed capacitance transient contains contributions from several defects, each with different emission rates. This simplest way to separate out distinct defects is to construct a DLTS spectrum through the application of a rate window to the capacitance transients

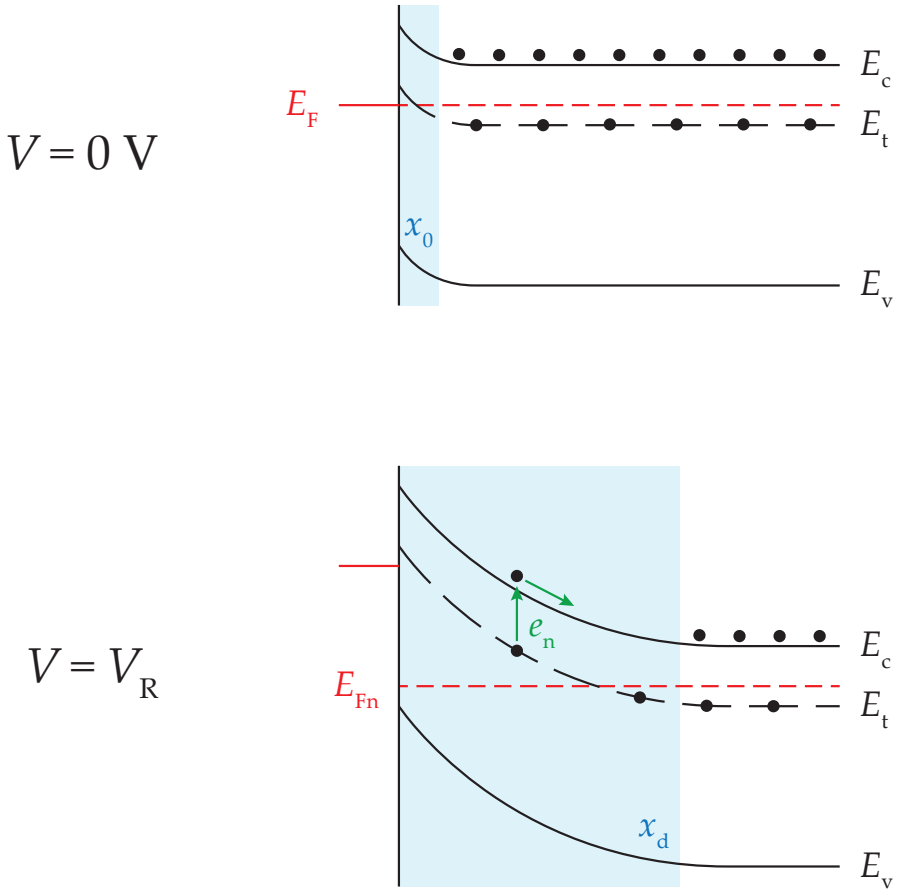

Figure 3-1: Schottky diode bands under neutral and reverse bias conditions

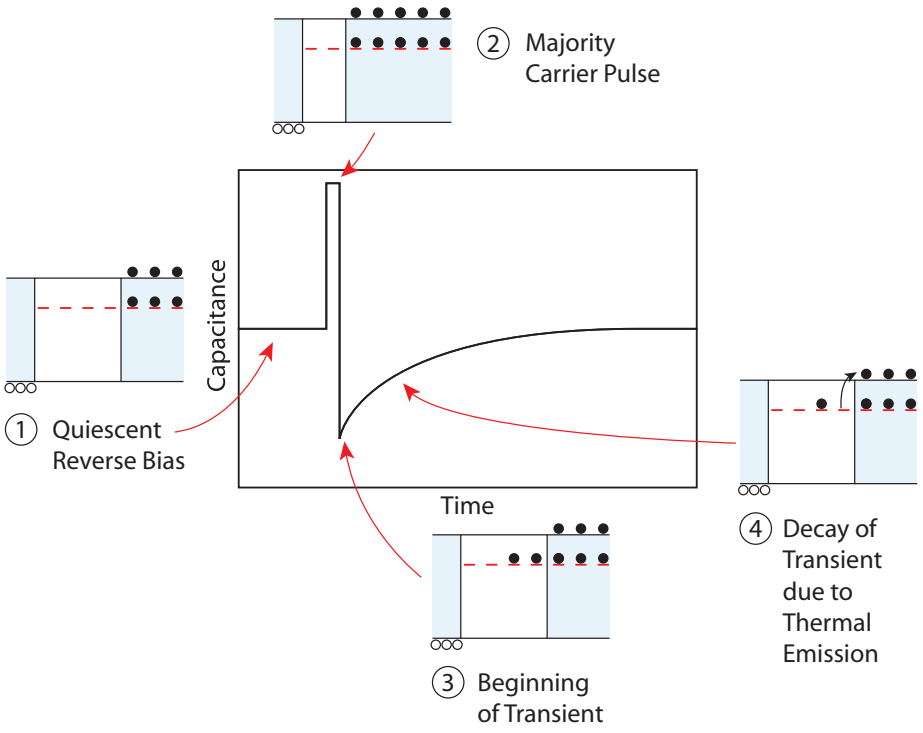

Figure 3-2: Schematic representation of the generation of a capacitance transient during DLTS measurements by emission of majority carriers from defect states in the depletion region of a diode after voltage pulsing. *Reproduced from [35]*

as the temperature is swept (Figure 3-3). In a conventional double boxcar averaging configuration, the capacitance is measured at two specific times and the difference is plotted as the temperature is swept. These times are chosen so that as the emission rate of a defect reaches a specific value, the signal difference reaches a maximum forming a peak in the DLTS spectra. Since each defect will have an emission rate equaling the time set by the rate window at a different temperature, individual defects can be distinguished (Figure 3-4). This rate window can be adjusted so that peaks correspond to different emission rates. Even though an individual spectrum only gives the emission rate of individual defects at a single temperature, they are often useful for giving an overview of the numbers and concentrations of defects present. Multiple temperature scans (or varying the rate window while the temperature is scanned) can be used to determine the relationship between the emission rate and temperature for each defect which can be used to determine the energy level and capture cross section of a defect state. An alternative to the double boxcar algorithm is the use of a lock-in amplifier algorithm where a larger part of the capacitance transient is used by integrating the first half of the window with a positive weight and the last half of the window with a negative weight. Use of more of the transient gives the lock-in amplifier algorithm a lower noise level. In this work, all conventional DLTS scans are acquired using a lock-in amplifier algorithm.

3.1.2 Laplace DLTS

In reality, capacitance transients observed are described by a spectral function

$$\Delta C = \int_0^\infty F(s) \exp(-st)\, \mathrm{d}s \tag{3.2}$$

where s is the emission rate. More than one defect can contribute to the capacitance transient observed. Defects whose peaks are close to each other or overlapping can be difficult to distinguish complicating determination of electronic properties using conventional DLTS analysis of transients. Laplace DLTS was developed to allow for higher resolution extraction of emission rates by numerical analysis of the entire transient [36]. This technique has much higher resolution and potentially lower noise (for long averaging) but is time consuming due to the need for the temperature to be stabilized to $\pm 0.01\,\mathrm{K}$ before transients can be obtained. In this work, most of the extracted electronic properties are obtained from analysis of Laplace DLTS data.

3.1.3 Determination of Defect Properties

3.1.3.1 Free Energy of Ionization

During DLTS measurements, the emission rate of carriers from defect states are measured as temperature is swept. For an electron trap, the relationship between the emission rate and the energy level of the defect state as determined from the principle of detailed balance is given by Equation 2.38. The temperature dependencies of N_c and $\langle v_\mathrm{n} \rangle$ can be factored

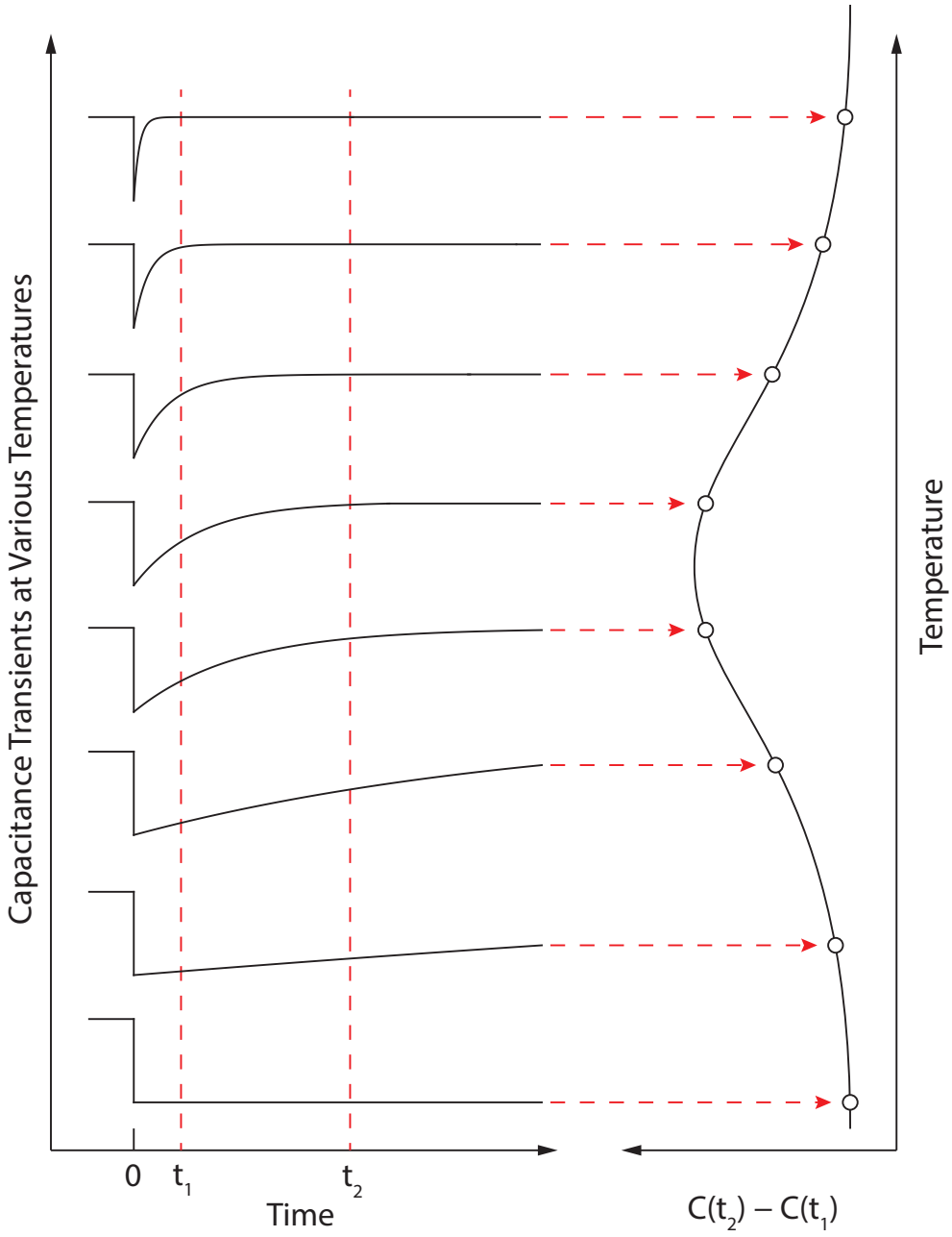

Figure 3-3: Construction of a DLTS spectrum by implementation of a rate window using a double boxcar configuration. *Reproduced from [35]*

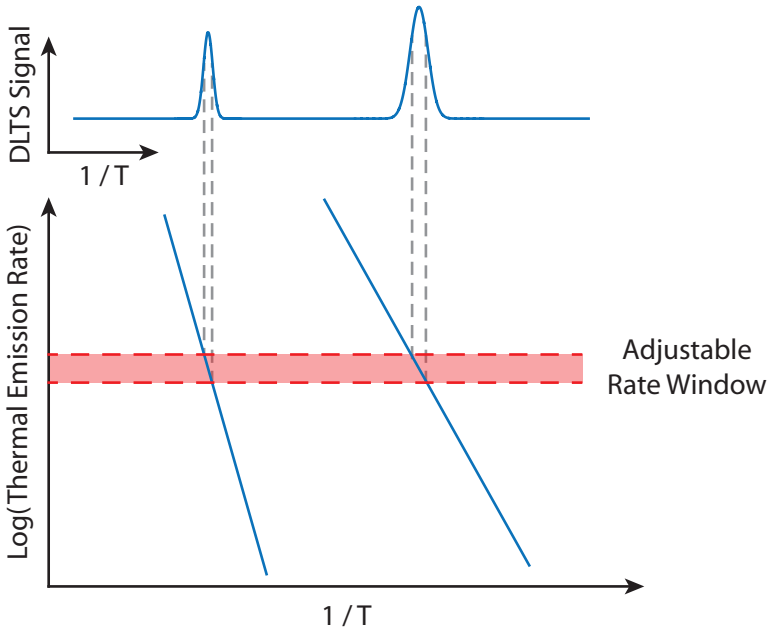

Figure 3-4: Schematic illustrating how a rate window produces a peak in the DLTS spectrum when the emission rate of the defect state corresponds to the chosen rate window. *Reproduced from [35]*

out to yield the following expression:

$$\frac{e_n}{T^2} = A\sigma \exp\left(-\frac{E_c - E_t}{kT}\right) \tag{3.3}$$

where A is independent of temperature and contains the relevant physical and material constants. Often the defect level and capture cross section are simply determined from the slope and y-intercept of a plot of e_n/T^2 vs. $1/T$. This results in an intrinsically rough estimation for the capture cross section due to the imprecision of the y-intercept extrapolation on an Arrhenius plot. This method can yield values that are significantly different from the real values due to the fact that the defect level and capture cross sections can be temperature dependent. In addition, the free energy of ionization of the defect contains enthalpy and entropy contributions. The capture process can be thermally activated resulting in an Arrhenius temperature dependence for the capture cross section. These two facts yield a difference between the measured (apparent) and real enthalpy of ionization and capture cross section. Consequently, for an accurate determination of defect properties the following expressions should be considered:

$$E_c - E_t = \Delta G = \Delta H - T\Delta S \tag{3.4}$$

and

$$\sigma(T) = \sigma_\infty \exp\left(-\frac{E_\sigma}{kT}\right). \tag{3.5}$$

Thus,

$$\frac{e_n}{T^2} = A\sigma_\infty \exp\left(\frac{\Delta S}{k}\right) \exp\left(-\frac{\Delta H + E_\sigma}{kT}\right). \tag{3.6}$$

Therefore instead of directly determining real values, an analysis of the plot of e_n/T^2 vs. $1/T$ leads to the extraction of an apparent enthalpy, E_a, and apparent cross section, σ_a, which correspond to

$$E_a = \Delta H + E_\sigma \tag{3.7}$$

and

$$\sigma_a = \sigma_\infty \exp\left(\frac{\Delta S}{k}\right). \tag{3.8}$$

Pulse filling methods (Section 3.1.3.3) can be used to independently measure the real capture cross section, $\sigma(T)$. Once E_σ and σ_∞ are known, the enthalpy and entropy can be calculated allowing for precise determination of the energy level of the defect state.

3.1.3.2 Defect Concentration

In addition to determination of the activation energy and capture cross section, DLTS allows for calculation of the defect concentration from

$$N_t \approx 2N_d \frac{\Delta C}{C_R} \tag{3.9}$$

where N_d is the donor dopant concentration, ΔC is the magnitude of the capacitance transient, and C_R is the capacitance at reverse bias. This equation is convenient because the concentration measurement does not rely on the location of the defect energy level within the bandgap. However, this calculation can be off by more than 50 % when the defect level is far from the Fermi level. In that case, there is a significant area, known as the transition region (Figure 3-5), between the depletion region and the neutral bulk of the material which contains carriers that have not been swept out of the depletion region due to screening effects [37]. If the precise energy level of the trap has been determined then the width of the transition region can be determined from

$$\lambda = \sqrt{\frac{2\varepsilon(E_F - E_t)}{q^2 N_d}} \tag{3.10}$$

where ε is the dielectric constant, E_F is the Fermi level, E_t is the free energy of the trap, and q is the elementary charge constant. With knowledge of the transition region width, diode area, A, and the junction capacitance under filling conditions, C_P, the precise defect concentration can be calculated from

$$N_t = 2N_d \frac{\Delta C}{C_R}\left[1 - \left(\frac{C_R}{C_P}\right)^2 - \frac{2\lambda C_R}{\varepsilon A}\left(1 - \frac{C_R}{C_P}\right)\right]^{-1}. \tag{3.11}$$

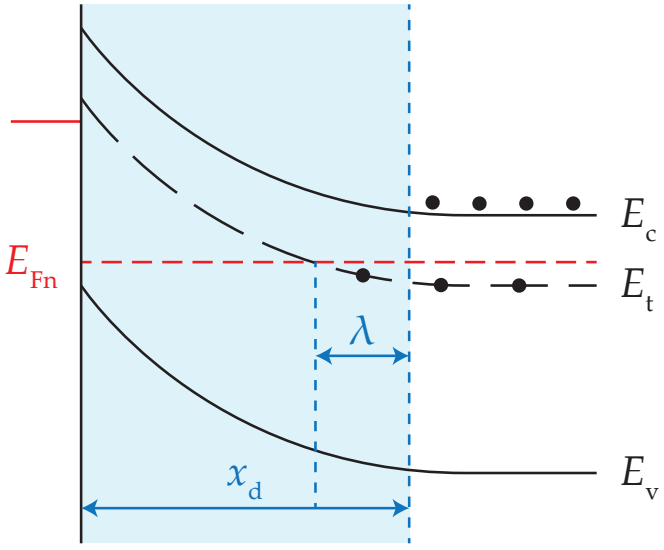

Figure 3-5: Schematic diagram of transition region for a reverse biased Schottky diode containing deep defect states.

3.1.3.3 Real Capture Cross Section

The real capture cross section can be determined by varying the duration of the DLTS filling pulse and observing how the magnitude of the DLTS signal varies in response. For defects observed in n-type materials, $e_n \gg e_p$ and c_p is negligible, whereas in p-type materials, $e_p \gg e_n$ and c_n is negligible. In addition, for short durations, majority carrier emission can be neglected reducing Equation 2.27 to

$$\frac{dn_t}{dt} = c_n(N_t - n_t), \qquad \text{n-type} \tag{3.12}$$

$$\frac{dn_t}{dt} = -c_p n_t. \qquad \text{p-type} \tag{3.13}$$

Assuming $n_t(0) = 0$ for majority carrier n-type traps and $n_t(0) = N_t$ for majority carrier p-type traps, these equations can be solved to yield

$$n_t(t) = N_t \left[1 - \exp(-c_n t)\right], \qquad \text{n-type} \tag{3.14}$$

$$n_t(t) = N_t \exp(-c_p t). \qquad \text{p-type} \tag{3.15}$$

To represent the number of emptied states due to hole capture, Equation 3.15 can be rewritten as

$$N_t - n_t(t) = N_t \left[1 - \exp(-c_p t)\right]. \tag{3.16}$$

In a typical DLTS measurement, τ_p, the filling pulse duration, is chosen such that $c_{n,p}\tau_p \gg 1$ and the trap is either completely filled with electrons for n-type materials, $n_t(\tau_p) = N_t$, or completely emptied of electrons for p-type materials, $n_t(\tau_p) = 0$. However, for short filling pulses, the measured DLTS signal (Equation 3.1) is modified:

$$\Delta C(\tau_p) = \left[1 - \exp(-c_{n,p}\tau_p)\right] \Delta C_{max} \tag{3.17}$$

where ΔC_{max} is the maximum observed signal obtained when τ_p is long. This expression allows for experimental measurement of the capture rate from DLTS measurements with varying filling pulse durations. The real capture cross section can then be determined from Equation 2.28 for electron traps and Equation 2.29 for hole traps. Measurements can be repeated at various temperatures to determine the temperature dependence of the capture cross section in order to extract out the parameters (σ_∞ and E_σ) in Equation 3.5.

It should be noted that if the capture cross section is too large, then measurement becomes limited by the inability to generate well-shaped pulses with durations short enough to only partially fill traps. In our experimental setup (Figure 3-6), the filling pulse duration is limited to ~200 ns.

3.1.4 Experimental Apparatus

A schematic of the experimental apparatus used for DLTS measurements is shown in Figure 3-6. Samples are mounted within a cryostat with electrical connections allowing for measurement of capacitance transients as the sample is cooled or heated. During sample pulsing, we utilized an analog switch in order to alternately connect the diode sample to the pulse generator and capacitance meter. If the capacitance meter is not removed from

the circuit during pulsing, it can act as a low-pass filter distorting the excitation pulse shape increasing rise and fall times as well as introducing ringing. In addition, the actual pulse voltage level seen by the sample can differ from the desired value. Removing the capacitance meter from the circuit during pulsing is particularly important for capture cross section measurements where short, square pulses are required. In addition to altering the shape of the excitation pulse, the excitation itself can overload the capacitance meter requiring that some portion of the initial transient be discarded. When using a switch, the recovery time of the capacitance meter can be reduced to ~100 µs increasing the sensitivity of our measurements.

The capacitance meter (Boonton 7200) supplies a DC bias when in connection to the sample reverse biasing the test diode. Our particular implementation uses a DG419 chip to switch from the capacitance meter to an external pulse generator upon application of +5 V to the DG419 TTL input. Instead of using an external pulse generator, it may seem sufficient to connect a higher voltage DC signal to the second switch input and define the pulse duration by the length of the TTL input. However, the large swing in voltage immediately seen upon switching causes some distortion of the signal pulse. Instead, we connect the second output of the switch to a pulse generator which is triggered by the same signal as the TTL pulse and sends a pulse after a 50 ns delay (where the bias during the delay is matched to the bias applied by the capacitance meter). A 50 ns delay after the pulse is also required before the TTL is removed and the sample is reconnected to the capacitance meter. This allows for well-formed square excitation pulses down to ~200 ns for bias changes as large as −12 V to 0 V.

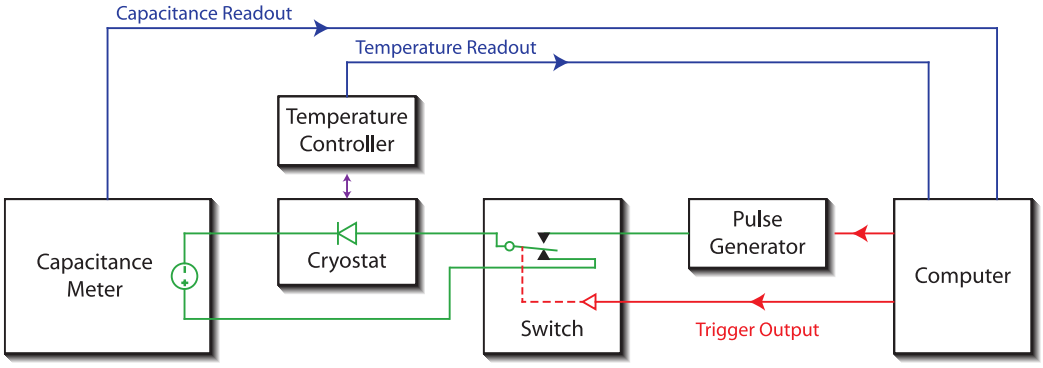

Figure 3-6: Schematic diagram of our DLTS experimental apparatus showing how a switch is used to remove the capacitance meter from the circuit during pulsing.

Our cryostat is cooled by a closed cycle helium compressor. Samples must be in good thermal contact with the cryostat state while being electrically isolated. Therefore, a polished sapphire wafer (0.010" thick) is mounted to the cryostat stage with a thin layer of silver paste. Samples can then be mounted to the sapphire wafer. In our work, diodes are fabricated with backside ohmic contacts such that junction areas are well defined by the top Schottky contact area allowing for accurate determination of defect concentrations. Electrical contact to the wafer backside is formed by mounting samples (with InGa eutectic) to a polished

copper plate to which a wire has been soldered. The copper plate is thermally contacted to the sapphire plate using InGa eutectic. Sample temperatures and PID feedback are both supplied by a calibrated Si diode sensor attached to the copper plate (with Apezion N, cryogenic vacuum grease) as close to the sample as possible. This mounting scheme allows for sample cooling down to ~30 K. However, in practice, the silver paste layer between the stage and sapphire wafer can crack at low temperatures only allowing for reliable cooling to ~60 K. Figure 3-7 contains a schematic representation of how samples are mounted within the DLTS cryostat.

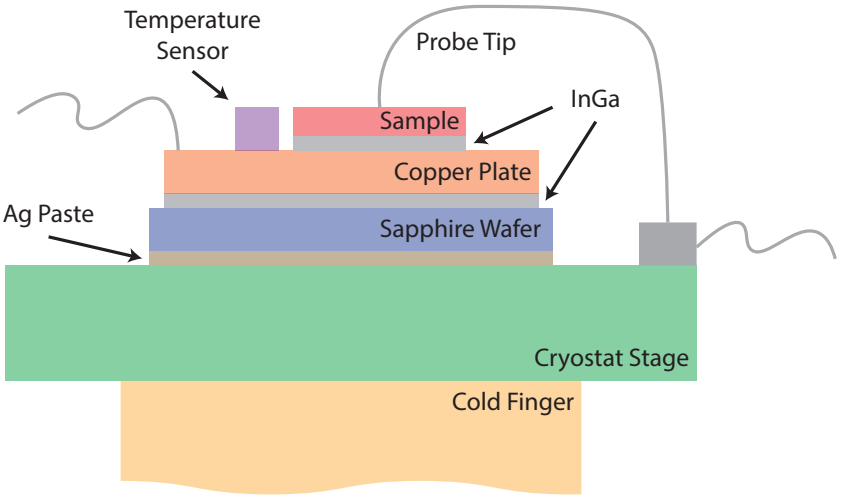

Figure 3-7: Schematic showing how back contacted samples are mounted within in the DLTS cryostat to maintain thermal contact while providing electric isolation.

3.2 Gamma Irradiation of Germanium

3.2.1 Point Defect Production

In order to probe defect states, a controllable and reliable method for introducing defects is required. This is achievable by using high energy photons and particles to intentionally create damage within the material. When incident radiation is able to transfer sufficient energy to displace atoms from their lattice site (~10s of eV), vacancy - interstitial pairs (also known as Frenkel pairs) are created (Figure 3-8). Once generated, these vacancies and interstitials can:

1. Recombine with each other and self-annihilate.
2. Be absorbed at sinks (i.e. dislocations, grain boundaries, and surfaces).
3. Combine with other vacancies and interstitials.
4. Combine with impurities in the material to form defect impurity associates.

Incident radiation will lose energy as it travels through a material through generation of electron-hole pairs (ionization) and the removal of atoms from their lattice sites (displacement) [38]. Displacement damage creates a wide variety of defects which are of interest

due to the resulting formation of new energy states within the bandgap. Atomic displacements directly result in the formation of vacancies and interstitials which can then migrate throughout the material. Some damage is quickly reversed by the migration of vacancies and interstitials to each other causing annihilation. However, some damage is permanent as vacancies and interstitials form into more stable defect configurations by clustering with like defects (for example creating divacancies) or binding to impurity and dopant atoms [39]. If enough energy has been transferred from the radiation to the displaced atom, the displaced atom can also interact with surrounding atoms causing further displacements. If these displacement cascades occur in a relatively small volume, regions of clustered defects can form.

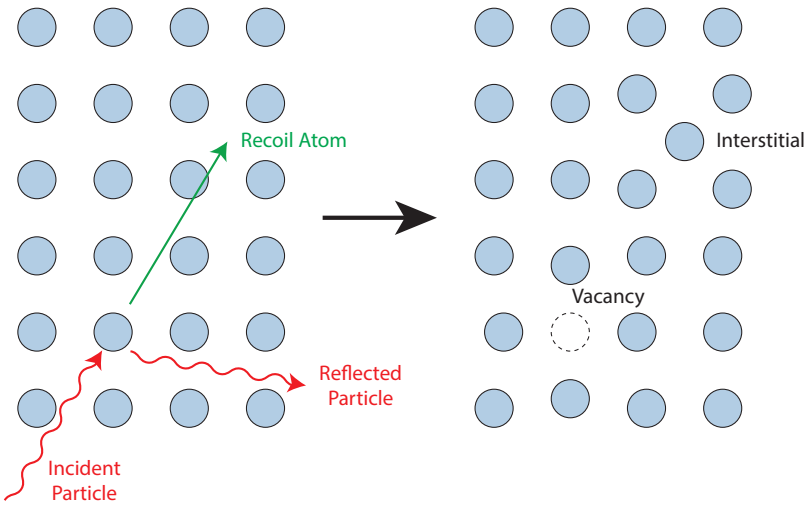

Figure 3-8: Schematic representation of Frenkel pair production in a crystalline material after collision of a high energy particle with a lattice atom.

3.2.1.1 Compton Scattering by ^{60}Co Gamma Irradation

High energy photons are highly penetrative and generate point defects through indirect means. The predominant energy loss mechanism for gamma rays (1.17 MeV and 1.33 MeV) emitted by ^{60}Co decay processes is Compton scattering by interaction with lattice electrons. Some of the lost photon energy is transferred to the electron from which it was scattered generating electrons whose energies can be close to that of the incident photon. The energetic recoil electrons can then create Frenkel pairs if they have sufficient kinetic energy to displace atoms from their lattice sites. From conservation of energy and momentum (accounting for relativisitic effects) the kinetic energy of the recoil electron can be calculated as a function of photon scattering angle from

$$KE_e = E_0 \frac{\alpha(1-\cos\theta)}{1+\alpha(1-\cos\theta)} \qquad \text{where} \qquad \alpha = \frac{E_0}{m_e c^2} \tag{3.18}$$

where E_0 is the energy of the incident photon and θ is the scattering angle. The differential cross section for photons scattered by electrons can be calculated from the Klein-Nishina formula [40]:

$$\frac{\mathrm{d}\sigma_{\mathrm{KN}}}{\mathrm{d}\Omega}(\alpha,\theta) = \frac{r_0^2}{2}\frac{1}{(1+\alpha(1-\cos\theta))^2}\left(1+\cos^2\theta+\frac{\alpha^2(1-\cos\theta)^2}{1+\alpha(1-\cos\theta)}\right) \tag{3.19}$$

where Ω is the solid angle and r_0 is the classical radius of an electron. Using this expression we can find the probability that a photon will be scattered between 0 and θ:

$$P(0\rightarrow\theta) = \frac{\int_0^{\theta}\frac{\mathrm{d}\sigma_{\mathrm{KN}}}{\mathrm{d}\Omega}\,\mathrm{d}\Omega}{\int_0^{\pi}\frac{\mathrm{d}\sigma_{\mathrm{KN}}}{\mathrm{d}\Omega}\,\mathrm{d}\Omega}. \tag{3.20}$$

The probability that a photon will be scattered between two angles (θ_1 and θ_2) is then

$$P(\theta_1\rightarrow\theta_2) = P(0\rightarrow\theta_2) - P(0\rightarrow\theta_1). \tag{3.21}$$

Figure 3-9 shows plots of scattering probability and kinetic energy transferred as a function of scattering angle for Compton scattering of incident photons with 1.33 MeV. The kinetic energy of the Compton electron can take any value between 0 and 1.1 MeV for irradiation by photons generated from ^{60}Co decay. Figure 3-10 shows the probability density of scattering as a function of electron energy after Compton scattering of a 1.33 MeV photon.

3.2.1.2 Number of Displacements Generated per Collision

The maximum energy transferred to a lattice atom after a binary collision with a high kinetic energy electron (accounting for relativistic effects) can be found from

$$T_{\mathrm{max}} = \frac{2ME(E+2m_{\mathrm{e}}c^2)}{(m_{\mathrm{e}}+M)^2c^2+2ME} \tag{3.22}$$

where m_{e} is the mass of an electron, M is the mass of the lattice atom, and E is the energy of the incident electron. The maximum energy transferred to Si and Ge atoms from recoil electrons produced by Compton scattering of ^{60}Co gamma irradiation is plotted in Figure 3-11. Previous studies [41] have shown that to create one Frenkel pair, the transferred energy needs to be above a threshold of approximately 20 eV. In order to create two Frenkel pairs from a single collision, the transferred energy needs to be four times the value necessary for single Frenkel pair production according to the Kinchin-Pease model [42]. As observed in Figure 3-11, the formation of two Frenkel pairs by one scattered electron is possible in silicon but not in germanium. Therefore, the divacancy, the defect with the largest introduction rate in irradiated CZ silicon after the A-center (V-O pair), can be created as a primary defect in silicon but not germanium.

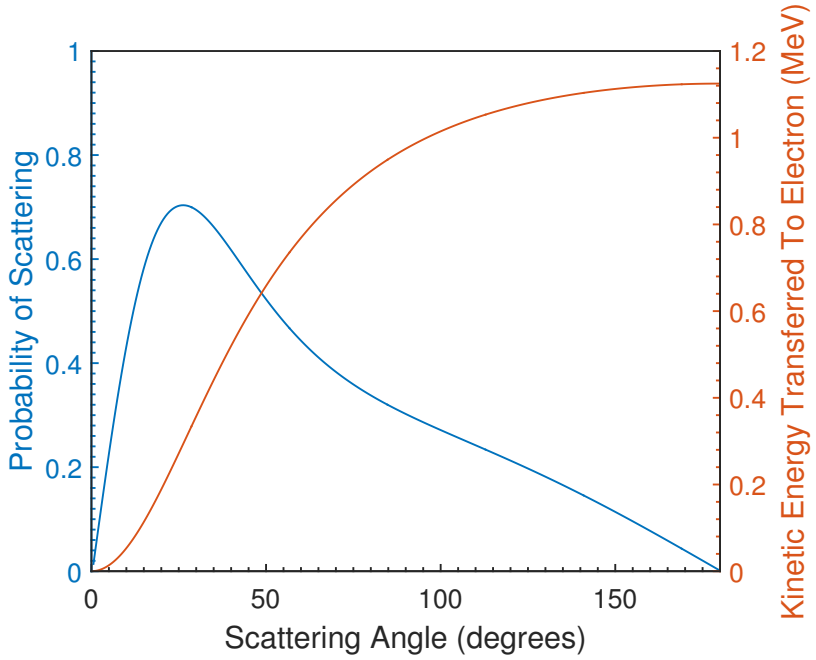

Figure 3-9: Scattering probability and kinetic energy transferred as a function of scattering angle for 1.33 MeV ^{60}Co irradiation. The kinetic energy of the Compton electron can take any value between 0 and 1.1 MeV.

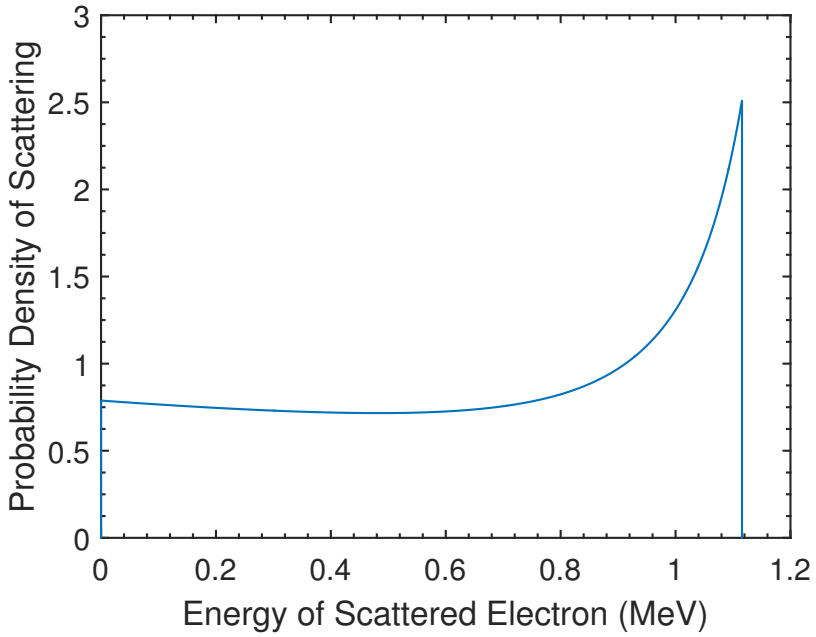

Figure 3-10: Probability density of Compton scattering by 1.33 MeV photons as a function of the kinetic energy of the scattered electron.

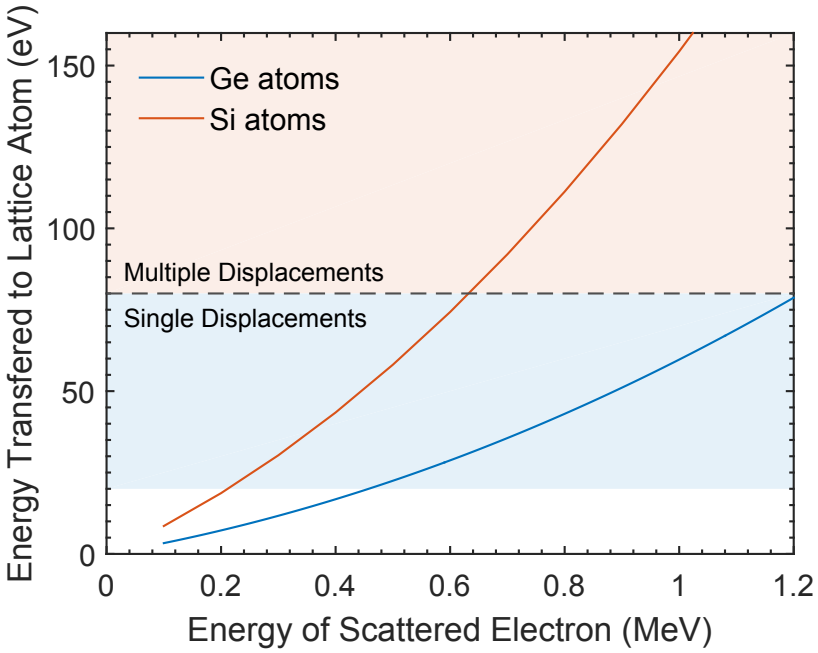

Figure 3-11: Maximum energy transferred to a lattice atom of silicon or germanium as a function of the kinetic energy of the scattered electron due to a binary collision. Previous studies have shown that the energy threshold for one displacement is approximately 20 eV. For that displacement threshold, Kinchen-Pease theory predicts that at least 80 eV is required for multiple displacements. If these thresholds are accurate, then multiple displacements will not occur in ^{60}Co gamma irradiated germanium.

3.2.2 Experimental Parameters

The tested germanium wafers were grown by Czochralski (CZ) method with an Sb concentration of $\sim 1 \times 10^{15}\,\mathrm{cm}^{-3}$ as measured by C-V analysis at 300 K. Schottky contacts were formed by thermal evaporation of Au onto Ge immediately after an adaptation of RCA cleaning procedures for germanium (5 minutes in a 1:4 NH_4OH:H_2O bath, followed by 30 seconds in 1:6 H_2O_2:H_2O, 15 seconds in HF and finally 30 seconds in 1:4 HCl:H_2O, all done at room temperature). Ohmic contacts were formed by scratching InGa eutectic alloy onto the backside of the wafer.

Gamma irradiations were performed at MIT using a ^{60}Co source which radioactively decays emitting gamma rays with energies of 1.17 MeV and 1.33 MeV in equal proportions. Samples were irradiated in a circular chamber lined with ^{60}Co rods providing homogenous irradiation of the material. In order to prevent oxidation of the surface during irradiation by ozone generated from the reaction of gamma rays with oxygen in the air, samples were irradiated either inside vacuum ampoules or with their surface in contact with a piece of silicon wafer. Both methods prevent sample surfaces from directly contacting the air in the irradiation chamber and yielded similar defect profiles. Radiation dose rates were approximately $7\,\mathrm{krad\,min}^{-1}$. Reported irradiation doses are calibrated with reference to water. This radiation source only generates isolated Frenkel pairs and rules out the direct generation of complex defects such as the divacancy (Section 3.2.1.2). While secondary formation of uncorrelated defects is possible (Section 3.2.6), the divacancy is not expected to form due to coulombic repulsion between negatively charged mono-vacancies.

Irradiation doses were chosen such that measured defect concentrations were not greater than 1 % of the carrier concentration. This allowed for a more accurate determination of defect concentrations when using DLTS. Gamma irradiations were performed after deposition of Schottky contacts. Gamma radiation with energies around 1 MeV are highly penetrative with absorption lengths close to 10 cm in germanium. Therefore, generated defects are expected to be homogenously distributed through the irradiated 500 µm thick wafer samples.

Anneals were performed by rapid submersion of samples, wrapped in aluminum foil, into a heated oil bath, followed by air quenching. DLTS signal was collected digitally using a lock-in amplifier algorithm allowing for measurement of defect concentrations $\sim 10^{-5}\,\mathrm{cm}^{-3}$ below carrier concentrations. Samples are placed in a cryogenic chamber which can be cooled to 85 K during measurements. DLTS scans of unirradiated diodes showed no defects with measureable concentrations.

3.2.3 Defect States

A DLTS spectrum for $1 \times 10^{15}\,\mathrm{cm}^{-3}$ Sb-doped germanium irradiated with ^{60}Co gamma radiation at room temperature (300 K) is shown in Figure 3-12. For coherence with previous convention, defects will be labeled by their apparent activation enthalpies; E_{37} denotes an electron trap with an apparent activation enthalpy of 0.37 eV. Four electron trap states were produced during irradiation in contrast to the numerous defect states seen in previous literature. Figure 3-13 shows emission rate vs. temperature data for defect states observed after gamma irradiation in this work compared to defect states seen in the

literature due to gamma, proton, and electron irradiation sources. Our data was analyzed to extract apparent activation enthalpies and apparent capture cross sections. Pulse-filling measurements were performed at various temperatures to measure real capture cross sections and determine temperature dependencies if present. A summary of properties extracted from DLTS measurements for the observed defect states after irradiation at 300 K is listed in Table 3.1. It should be noted that, even though DLTS has sensitivity to 10^{-5} cm^{-3} below carrier concentrations, we observe variations in introduction rates from sample to sample, making the reported introduction rates accurate to approximately ±10 %. When possible, anneals were performed on the same sample in order to remove error from this contact to contact variation. In those cases, the error in defect concentration is close to the limit of DLTS sensitivity. To make comparisons between samples with varying doses, defect concentrations are normalized by the irradiation dose and are reported in units of cm^{-3} Mrad^{-1}. We approximate our temperatures to be accurate to ±1 K which allows for accuracy of reported energies to ±1 %.

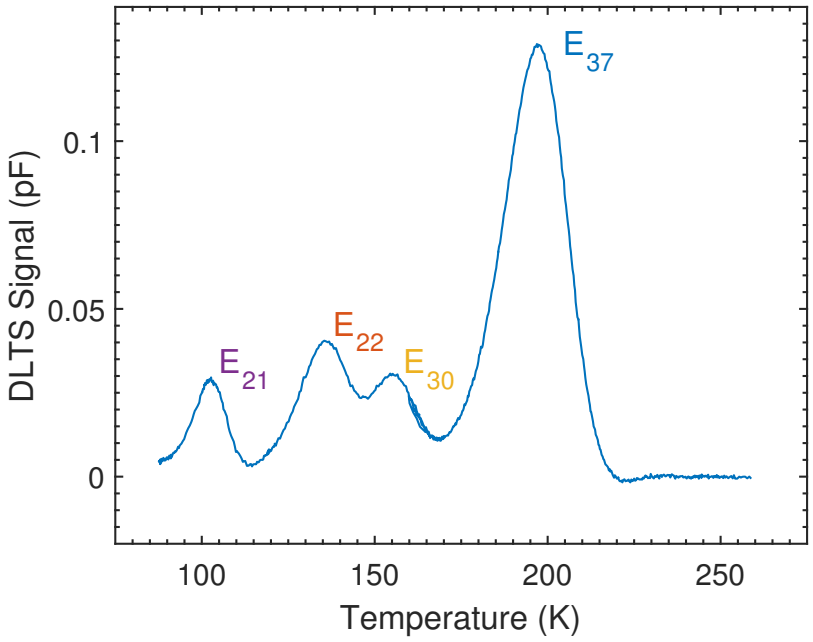

Figure 3-12: DLTS spectrum obtained after ^{60}Co irradiation at 300 K of 10^{15} cm^{-3} Sb-doped germanium showing the generation of four distinct defects. During measurement, the sample was pulsed for 5 ms from −5 V to 0 V and signal was collected for a 200 s^{-1} rate window.

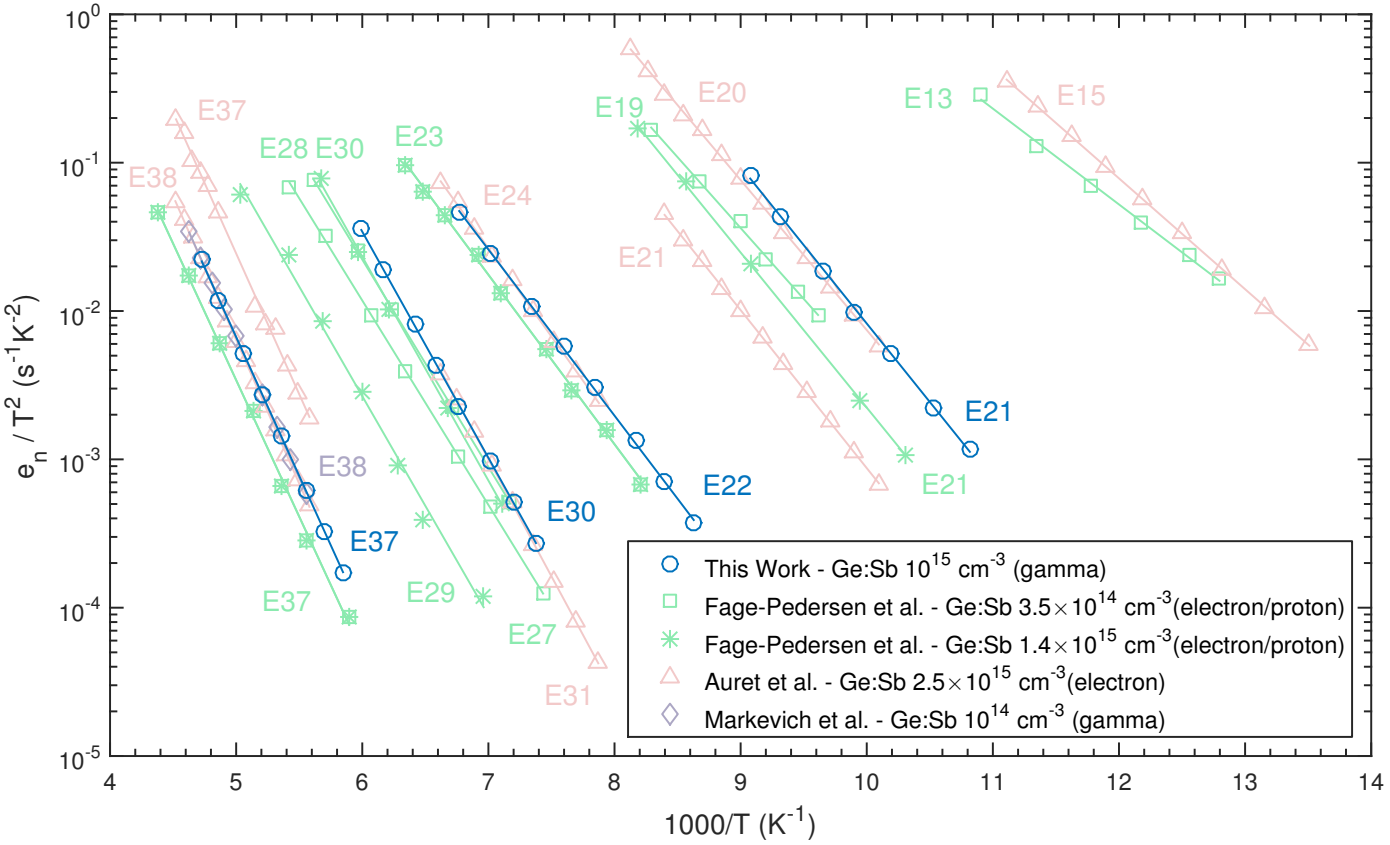

Figure 3-13: Defect states observed by different groups [30, 31, 33] in studies of Sb-doped n-type germanium irradiated by varying radiation sources. E_{37} is observed in all studies and has previously been assigned to the E-center, a donor-vacancy pair. Defects with states similar to E_{30}, E_{22}, and E_{21} have been seen in some studies but are not consistently detected.

Table 3.1: Summary of defect states in ^{60}Co irradiated Sb-doped germanium

Defect	Apparent Enthalpy (eV)	Free Energy of Ionization (eV)	Apparent Capture Cross Section (cm^2)	Real Capture Cross Section (cm^2)	Introduction Rate ($cm^{-3}\,Mrad^{-1}$)
E_{37}	0.37	$0.29 - 3.94kT$	3.9×10^{-15}	$7.6 \times 10^{-17} e^{-85\,meV/kT}$	2.2×10^{11}
E_{30}	0.30	NA[a]	1.2×10^{-14}	$>10^{-15}$	NA[b]
E_{22}	0.22	$0.22 - 1.53kT$	4.6×10^{-16}	1.1×10^{-16}	NA[b]
E_{21}	0.21	$0.16 - 8.29kT$	8.0×10^{-14}	$2.0 \times 10^{-17} e^{-54\,meV/kT}$	NA[b]

[a] The experimental apparatus was not fast enough to measure the real capture cross-section of E_{30} preventing calculation of the real enthalpy and entropy of ionization.

[b] Not quantifiable since defect concentrations evolve at 300 K.

The properties of a defect state are more than just an identifying tool and provide information about the physical nature of the defect. A temperature dependent capture cross section indicates the presence of an activation barrier to carrier capture or that capture requires phonons [43] due to rearrangement of bonds upon capture and emission of carriers. The entropy of ionization term in the free energy results from changes in configurational and/or vibrational (i.e. related to the strength of the bond) entropy after carrier capture, which is why it is frequently observed in conjunction with a temperature dependent capture cross section. We can therefore infer that E_{37} and E_{21} experience a structural rearrangement upon absorption of a carrier.

3.2.4 Defect Reactions

3.2.4.1 Irradiation at 77 K

Samples were irradiated with a 10 Mrad dose while submerged in liquid nitrogen (77 K) to study the diffusion of primary defects and the growth of associates. During and after irradiation, the samples were kept in the dark to prevent any effects from photogeneration of carriers. At the time of the first measurement (20 minutes spent above 200 K), only E_{30} and E_{37} are observable. The concentration of E_{30} is close to the noise level (10^9 cm^{-3} Mrad^{-1}) while the concentration of E_{37} is much higher at 1.7×10^{11} cm^{-3} Mrad^{-1}. Unlike E_{30}, E_{22}, and E_{21}, the concentration of E_{37} remains constant during the duration of the experiment with an introduction rate similar to room temperature irradiation levels. Similar fast formation kinetics were also observed after a 22 K electron irradiation of Sb-doped germanium by Mesli et al. [44]. E_{37} has been previously identified as the Sb donor-vacancy associate, also referred to as the E-center. The evidence for this will be discussed in Section 3.2.5.1. Ionized Sb atoms have a positive charge which can interact strongly with negatively charged mono-vacancies. The identification of E_{37} as the E-center is therefore consistent with the observed formation kinetics.

We expect that there are no competing sinks with Sb since no other impurity is present in as large concentrations in the tested material. In addition, the Sb concentration is much greater than the concentration of generated defects; therefore, the fast defect formation indicates that all of one type of the primary defects, most likely the vacancies, are quickly consumed by the formation of E_{37}. The introduction rate of E_{37} thus provides an estimate of the introduction rate of uncorrelated Frenkel pairs, the vacancy-interstitial pairs which do not recombine and annihilate shortly after generation by incident radiation.

If E_{37} accounts for all the vacancies in the material, then E_{30}, E_{22}, and E_{21} represent defect states of interstitial associates. Figure 3-14 shows the defect concentrations of E_{30}, E_{22}, and E_{21} plotted as a function of the time spent by the samples above 200 K after irradiation and removal from liquid nitrogen. E_{37} is not plotted because its introduction rate is higher and its concentration constant. The differences in annealing behavior show that none of the observed defect states are different charge states of the same defect. The annealing behavior in Figure 3-14 has two stages. During the first stage, all the defects grow, which shows that they form after irradiation and are secondary defects. E_{22} is the last defect to be observed, however, once detected, it has the fastest formation kinetics and outgrows E_{21} and E_{30}. This behavior will be addressed in greater detail in Section 3.2.5.2. The second annealing stage

starts after approximately four days of annealing when E_{22} continues growing at a slower pace, while the concentration of E_{21} is stable and E_{30} decays.

The existence of two stages in the evolution of the defects can be explained by accounting for the consumption of all the free self-interstitials in the material. During irradiation, interstitials and vacancies are created in equal proportions. All the mono-vacancies might quickly react with Sb to form E-centers, but perhaps self-interstitials cannot find sinks as quickly. They diffuse through the material until they form stable and observable defect associates. This corresponds to the first annealing stage. Note that this would indicate that the self-interstitial is not detectable by DLTS, likely because the defect state is in the lower half of the bandgap or outside the bandgap. If there are enough sinks, eventually all the self-interstitials will have reacted and the second stage begins where defects can only evolve by transforming into one another. The kinetics involved in the second stage are slower than in the first stage as the reactions involve defect associates which are not as reactive as the self-interstitial. The observed defect formation kinetics after irradiation at 77 K are consistent with observations in low temperature studies by Mesli et al. [44] and Kolhlerkovsky et al. [45].

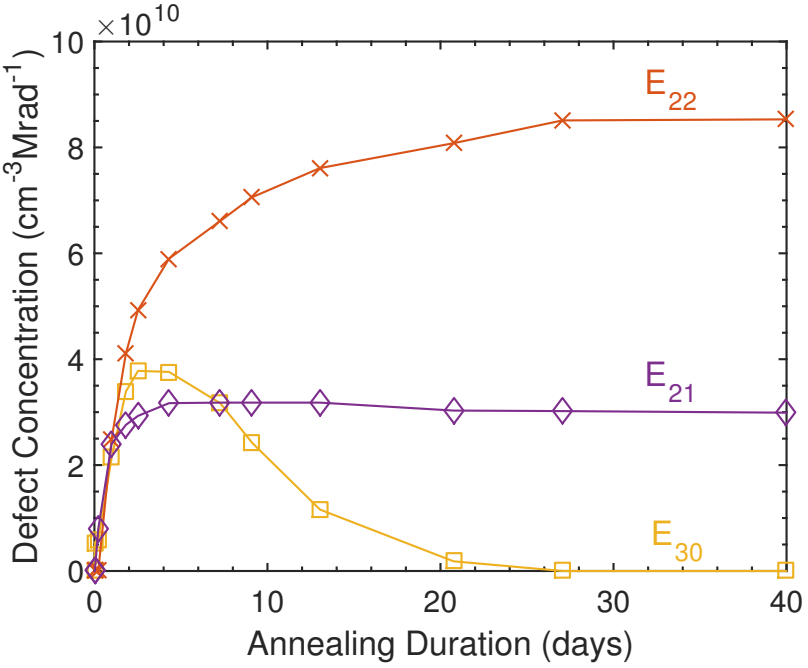

Figure 3-14: Interstitial containing defect concentrations during room temperature (300 K) annealing of Ge irradiated at 77 K by ^{60}Co. Annealing duration represents the time the sample spent above 200 K after irradiation. The concentration of E_{37}, which accounts for all the vacancies, is constant at 1.7×10^{11} cm^{-3} Mrad^{-1} for the entire annealing duration. Defect concentrations are normalized by the irradiation dose and are reported in units of cm^{-3} Mrad^{-1}.

3.2.4.2 Irradiation at 300 K

Irradiation at room temperature was followed by anneals at higher temperatures to provide additional information about the growth and decay of the defects. Defect concentrations after a series of 15 minute isochronal anneals at various temperatures are plotted in Figure 3-15. E_{37}, E_{22}, and E_{21} are all stable at room temperature. However, at room temperature, E_{30} will slowly decay over weeks, as was observed during room temperature annealing after irradiation in liquid nitrogen, and is already completely removed by annealing at 85 °C for 15 minutes. E_{37} is stable to ~100 °C and is only completely removed in 15 minutes at ~200 °C. At temperatures ~100 °C, E_{22} decays while E_{21} concomitantly grows. E_{21} is stable to ~150 °C.

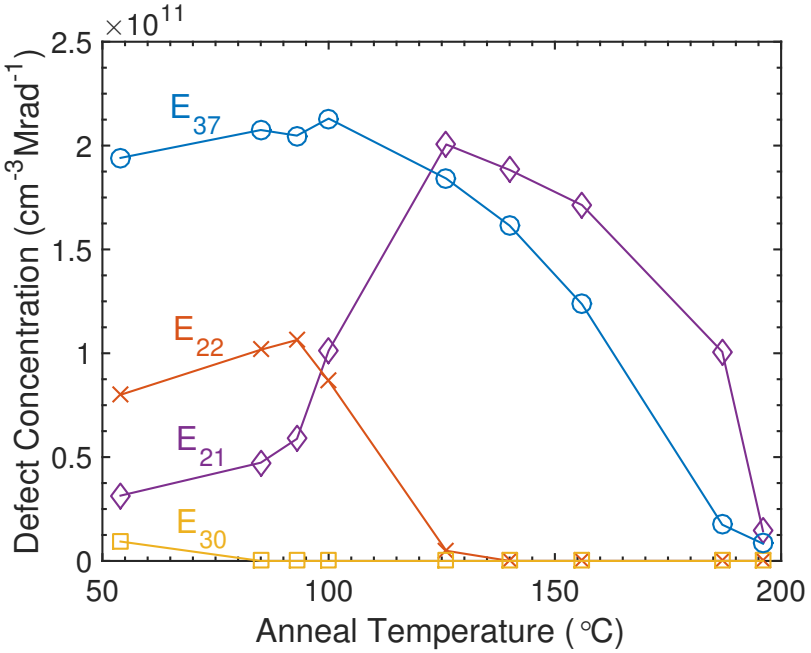

Figure 3-15: Defect concentrations after 15 minute isochronal anneals of ^{60}Co irradiated Sb-doped germanium. Defect concentrations are normalized by the irradiation dose and are reported in units of $cm^{-3}\,Mrad^{-1}$.

Isothermal anneals at multiple temperatures were used to extract annealing rates for each defect vs. temperature. Figure 3-16 shows defect concentrations vs. annealing durations for an isothermal anneal at 93 °C. All annealing reactions followed exponential trends indicating first-order reactions. Figure 3-17 shows a plot of the annealing rate vs. inverse temperature used to extract the frequency prefactors and activation energies of the annealing defect reactions. A summary of the extracted parameters are shown in Table 3.2. Spatial defect profiles were obtained before and after annealing reactions and showed that concentrations for all defects remained homogenously distributed throughout the material after annealing.

The isochronal and isothermal annealing data suggests a relationship between E_{21} and E_{22}. After 15 minutes at 100 °C (Figure 3-15), E_{30} has annealed out and E_{37} is stable, but

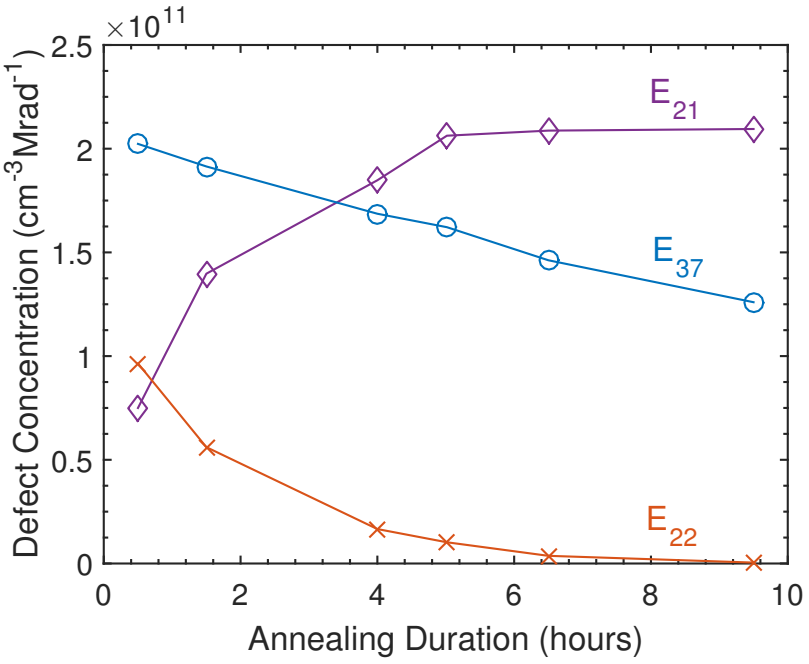

Figure 3-16: Defect concentration as a function of annealing duration at 93 °C. When E_{22} has annealed out, E_{21} stops evolving whereas the decay rate of E_{37} is not affected. Defect concentrations are normalized by the irradiation dose and are reported in units of $cm^{-3}\,Mrad^{-1}$.

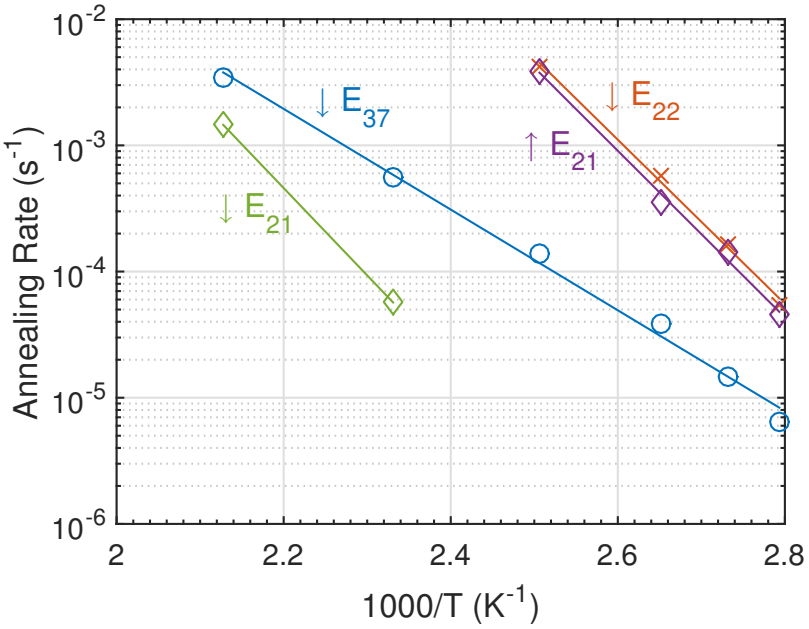

Figure 3-17: Annealing rate vs. temperature data extracted from isothermal anneals of ^{60}Co irradiated Sb-doped germanium. Up (↑) and down (↓) arrows next to defect labels indicate whether the defect concentration increases or decreases upon annealing.

Table 3.2: Summary of reaction parameters extracted from isothermal anneals

Annealing Reaction	Activation Energy (eV)	Frequency Prefactor (s^{-1})	R^2
E_{37} Decay	0.79	1.2×10^6	0.9943
E_{22} Decay	1.29	8.9×10^{13}	0.9956
E_{21} Growth	1.31	1.3×10^{14}	0.9961
E_{21} Decay	1.41	1.9×10^{12}	NA

the concentrations of both E_{22} and E_{21} change. The concentration of E_{22} decreases while the concentration of E_{21} increases. Eventually, the growth of E_{21} stops at ~125 °C which coincides with the removal of E_{22}. E_{37} is not coupled to the two defects as can be inferred from Figure 3-16 and isothermal anneals at other temperatures not shown here; the growth of E_{21} stops after E_{22} has fully annealed out, while the decay of E_{37} is unaffected and continues at a constant rate. This gives further evidence that E_{21} and E_{22} contain the same primary defect. The increase in the concentration of E_{21} when E_{22} decays shows that the decay reaction of E_{22} provides reactants for the growth of E_{21}. As seen in Table 3.2, the growth of E_{21} and decay of E_{22} have the same activation energy (~1.3 eV) and prefactor (~10^{14} s^{-1}). This indicates that the growth of E_{21} is favorable at these temperatures but is limited by the supply of reactants produced by the decay of E_{22}. The activation energy and prefactor for the growth of E_{21} would differ from the decay of E_{22} if an unobservable defect was providing reactants.

The prefactors in Table 3.2 also provide information about annealing mechanisms. The prefactor can be viewed as the attempt frequency (usually equal to the Debye frequency: 7.5×10^{12} s^{-1} at room temperature for germanium) divided by the number of jumps required to reach the sink:

$$\nu_0 = \frac{\nu_{\text{attempt}}}{N_{\text{jumps}}}. \tag{3.23}$$

The small annealing prefactor of E_{37} is consistent with a diffusion limited annealing reaction. The high annealing prefactors for the interstitial defect reactions indicate that the annealing process is a single jump event, such as dissociation or a configurational transformation of the defect.

3.2.5 Defect Assignments

3.2.5.1 Donor-vacancy associate: E_{37}

The defect with the largest introduction rate in ^{60}Co irradiated Sb-doped germanium is E_{37}. Its defect state properties match those measured by other groups [30, 32, 46] (Table 3.1). To date, it is the most studied defect in germanium and is associated in the literature to the second acceptor state of the Sb donor-vacancy associate. This identification is based on observations showing that the introduction rate scales with the doping level in oxygen lean samples [29] and by analogy to silicon, in which the E-center and the divacancy are the most predominate defects in oxygen-lean wafers. Other studies focused on the variability

of this defect depending on the group V impurity [31] and also confirmed that this peak is dopant related. The attribution to the second acceptor state is due to its small capture cross section (due to coulombic repulsion between the electrons) and the absence of a Poole Frenkel effect. However, there is no EPR confirmation of the identification of E_{37} as the E-center in germanium due to the difficulties of this technique in this material. The identification of E_{37} as a vacancy defect is therefore not as unambiguous as it is for the E-center in silicon. With this reserve in mind, we will keep using the ideas that E_{37} is the E-center and contains a vacancy in the following discussion, as we have until now. The properties of E_{37} measured in this work are compatible with its identification as the second acceptor state of the Sb-V pair. The high introduction rate and fast formation kinetics are a result of the large concentration of Sb sites as sinks for mono-vacancies. The high entropy of activation and temperature dependent cross-section indicate a bond rearrangement upon absorption/emission of a carrier which can result from the rearrangement of the defect to minimize the coulombic repulsion between two electrons upon transition from a singly to doubly occupied state. As shown in Figure 3-16, the decay of E_{37} proceeds at a constant rate regardless of fluctuations in the concentrations of the other defects confirming that it contains a primary defect different from the other observed defect associates.

The smaller than Debye frequency prefactor of E_{37} ($1.2 \times 10^6\,\mathrm{s}^{-1}$) indicates removal of the defect by diffusion to a sink. From Equation 3.23, the measured prefactor requires the defect to jump $\approx 10^7$ sites to reach a sink. For a 3D random walk model

$$\langle r^2 \rangle = 3a^2 N_{\mathrm{jumps}}. \tag{3.24}$$

Therefore, 10^7 jumps correspond to a migration distance of approximately $\sim$1 µm (with nearest neighbor distance, $a = 0.245\,\mathrm{nm}$). There are two possible sinks for E_{37}:

1. The surface can act as a sink as was proposed by Fage-Pedersen et al. [30]. However, diffusion to the surface would not result in first-order decay behavior nor the uniform depth profile observed after annealing.
2. The sink can be an impurity present in the bulk of the material which is more consistent with our observations. Based on the required migration distance of 1 µm, the concentration of the sink would have to be $\sim 10^{12}\,\mathrm{cm}^{-3}$, which is lower than the observed E_{37} concentration for doses higher than 5 Mrad. Our observation of a first order decay reaction likely means that the sink is not saturated after removal of E_{37}. Therefore, each sink site can possibly accommodate multiple reactants.

The measured activation energy for the decay of E_{37} is not compatible with the Sb migration activation energy measured by diffusion studies at higher temperatures [47]. Therefore, we can assume that it is not the E-center itself that diffuses, but the mono-vacancy, after dissociation of the E-center. Consequently, if we assume that the annealing of E_{37} is diffusion limited, it implies that the annealing coefficient is proportional to the diffusivity of the mono-vacancy times the probability of dissociation of the E-center. In this case, the annealing activation energy is the sum of the activation energy of diffusion (migration energy, E_{m}) plus the activation energy of dissociation (binding energy, E_{b}):

$$E_{\mathrm{a}} = E_{\mathrm{m}} + E_{\mathrm{b}}. \tag{3.25}$$

The binding energy contains a coulombic interaction as well as additional contributions. Therefore we can estimate a lower bound for the binding energy from just the coulombic interaction between the dissociating species from

$$E_{\mathrm{b}} = \frac{1}{4\pi\varepsilon}\frac{q_1 q_2}{r} \tag{3.26}$$

where q_1 and q_2 are the charges of Sb and the vacancy, ε is the dielectric constant, and r is the interatomic distance (0.245 nm), which we assume separates the charges. An upper limit on the value of the migration energy can then be roughly approximated from the difference in our measured activation energy and our estimated binding energy. At the temperature of annealing, the E-center is in the single acceptor state and density function theory (DFT) calculations [48] predict the mono-vacancy to be singly negatively charged. This yields two scenarios. If we assume that the vacancy is doubly negatively charged upon dissociation, then we find a value of 0.75 eV for the binding energy of the E-center which gives an experimental estimate for the migration energy of the mono-vacancy of < 0.04 eV. If before dissociation the E-center loses an electron, then the mono-vacancy is only single negatively charged during the dissociation, and the binding energy becomes 0.37 eV which yields an estimate of the migration energy of < 0.4 eV.

3.2.5.2 Interstitial associates: E_{30}, E_{22} and E_{21}

E_{30} is a defect that has been observed before but was not thoroughly characterized. Its measured energy level and annealing behavior are consistent with the defect $E_{0.30}$ reported by Fage-Pedersen et al. [30]. In addition, Auret et al. [46] and Roro et al. [49] also report defects with similar states but real capture cross sections and annealing behavior were not reported. No defects with matching properties have been reported by Nagesh et al. [29] or Markevitch et al. [32] E_{21} and E_{22}, similarly to E_{30} have been observed before but were not the focus of the studies. The measured defect state and annealing behavior of E_{22} is consistent with $E_{0.23}$ reported by Fage-Pedersen et al. and E1 reported by Mooney et al. [28]. Its defect state also matches $E_{0.24}$ reported by Auret et al. whose annealing behavior was not reported. It was not observed by Nagesh et al. E_{21} matches the defect state of $E_{0.20}$ reported by Auret et al. but its annealing kinetics were not reported. E_{21}'s defect state is close to Fage-Pedersen et al.'s $E_{0.19}$ and $E_{0.21}$ but the annealing kinetics do not match perfectly. In addition, Fage-Pedersen et al. does not observe $E_{0.21}$ for all doping concentrations tested. It is important to remember that Fage-Pedersen et al. reports more defects than other groups in the literature and does not systematically observe them in all the wafers tested. Due to their use of higher energy irradiation sources, different numbers of defect states would be expected when compared to this study. E_{21} is not observed by Nagesh et al. or Mooney et al.

Based on the assumption that the E-center captures all the mono-vacancies and the observation of coupled annealing reactions, we have concluded that these three defects contain interstitials. However none of these defects are likely the self-interstitial; they are not present immediately after the irradiation at 77 K and their concentrations initially grow after irradiation (Figure 3). Calculations have shown that self-interstitials can exist in multiple configurations [50] (D, H, T, hybrid, etc.) which can each have distinct defect states

in the bandgap. Defects associates containing interstitials can also undergo a change in configuration upon change of charge state which is why interstitial associates typically have a large entropy of ionization, as observed for E_{21}. Therefore, in addition to dissociation, transitions occurring in a single jump can possibly be transformation of an associate from one configuration into another with a different defect state. Studying the conversion these defects states undergo during anneals at various temperatures will allow us to investigate whether these states are different configurations of the same associate.

Transformation of E_{22} to E_{21}

From the series of high temperature isothermal anneals, we showed that the decay of E_{21} and the growth of E_{22} are coupled (similar activation energy and prefactor for growth and decay reactions as well as the saturation of E_{21} once E_{22} has annealed out). In order to further investigate the link between these defects, their conversion ratio, $(\Delta E_{21}/-\Delta E_{22})$, has been estimated as a function of the annealing temperature in Table 3.3. The data is noisy but appears to be temperature dependent. These ratios are: (a) more than one, (b) less than two, and (c) increase with increasing temperature. Point (a) shows that there is possibly more than one interstitial in E_{22} because there cannot be a conversion ratio higher than the ratio of primary defects per defect. Point (c) shows that there is an activation barrier to the conversion indicating that some interstitials are lost to sinks (surface, impurity, and/or vacancies from dissociation of E_{37}) upon annealing at lower temperatures. Point (b) suggests a saturation of the ratio at two which means that the conversion rate likely cannot be higher than two. It is therefore possible that E_{22} contains two interstitials and E_{21} only one. However, E_{22} containing two interstitials does not mean that E_{22} is the di-interstitial because this reasoning does not rule out the possibility that it is a di-interstitial impurity associate.

The conversion of E_{22} into E_{21} is characterized by a large prefactor, higher than the Debye frequency which is a sign that the limiting step of the transformation consists of a single jump. The larger than the Debye frequency magnitude can be caused by an entropic effect; if the defect transformation results in an increase in entropy, the measured prefactor contains an $\exp(\Delta S/k)$ term. A value of ~2.5k can explain the discrepancy between the annealing prefactor and the Debye frequency. This is consistent with the interpretation that E_{22} contains two interstitials, which implies a large change of configurational and vibrational entropy upon transformation into two E_{21}.

Further evidence that E_{22} contains two interstitials is presented in Figure 3-18 which shows the number of countable interstitials after room temperature annealing for the sample irradiation in liquid nitrogen, assuming that the E_{30} and E_{21} contain one interstitial and E_{22} contains two interstitials. During the second annealing stage, the total countable interstitial concentration does not vary as expected; if all interstitials are paired with defects, then changes in defect concentrations only occur due to transformations from one defect into another. In addition, the assignment that E_{22} contains multiple interstitials is consistent with its small entropy of ionization compared to E_{21}'s. We might expect that a defect containing multiple interstitials is more configurationally constrained compared to an associate which contains a single interstitial resulting in a smaller entropy of ionization for the multiple interstitial containing defect.

Table 3.3: Conversion ratio of E_{22} to E_{21}

$\Delta E_{21} / -\Delta E_{22}$	85 °C	93 °C	104 °C	114 °C	126 °C
Average	1.44	1.47	1.59	1.99	1.93
Std. Dev.	0.064	0.09	0.30	0.007	0.15

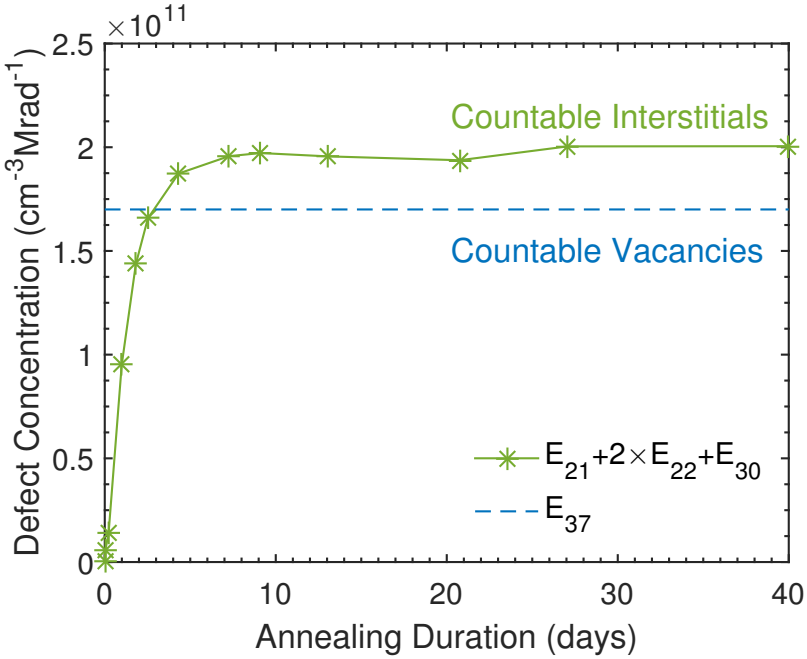

Figure 3-18: Concentration of interstitials contained in the defects we observe during room temperature (300 K) annealing of Ge irradiated at 77 K by ^{60}Co. If we assume that E_{21} and E_{30} only contain one interstitial and E_{22} contains two, after ~6 days the number of countable interstitials is constant as the defects evolve only by changing from one into another. Defect concentrations are normalized by the irradiation dose and are reported in units of $cm^{-3}\,Mrad^{-1}$.

Transformation of E_{30} to E_{22}

During the second annealing phase (Figure 3-14), E_{30} anneals out and fuels the growth of E_{22} but does not affect the concentration of E_{21}. If E_{30} dissociates and creates free self-interstitials, then both E_{22} and E_{21} should grow during the second annealing stage as occurs during the first stage. We propose two possible models to elucidate this problem: (a) dissociation then fusion: E_{30} releases its interstitials, they diffuse and, because of a higher activation barrier for the interstitial to form E_{21} rather than E_{22}, they associate with each other forming E_{22}; (b) diffusion then fusion: E_{30} transforms into E_{22} without dissociating. However, scenario (a) seems unlikely because E_{21} forms during the first stage of the growth when self-interstitials are available. Scenario (b) explains why E_{21} stops growing during the second phase of the annealing, but it also raises some questions. If E_{30} contains only one interstitial, then, assuming that E_{22} contains two interstitials, the transformation either requires one E_{30} to capture an interstitial or two E_{30} to fuse. The capture of interstitials by E_{30} is unlikely for the same reason that scenario (a) is unlikely; if self-interstitials are available for reaction, the concentration of E_{21} should also increase. The fusion of two E_{30} requires that the decay of E_{30} and the growth of E_{22} follow a second order reaction kinetics with the same reaction rate. Currently, there is not enough data to accurately determine the reaction orders for these defect reactions. However, the fact that E_{22} is initially absent during the first 10 hours of room temperature annealing following the liquid nitrogen irradiation but then outgrows both E_{21} and E_{30} indicates that the formation of E_{22} does not only involve self-interstitials. Therefore the presence of E_{30} might be necessary to the formation of E_{22}. This adds to the likelihood of requiring the fusion of two E_{30} in order to form E_{22}.

3.2.6 Formation of Secondary Defect Associates

Secondary formation of divacancies is rare in irradiated CZ silicon. The large concentration of background impurities including oxygen at approximately $10^{18}\,\mathrm{cm}^{-3}$ makes it unlikely that isolated primary defects in dilute concentrations will ever react with each other before finding an impurity with which it can associate. The environment in CZ germanium is unique due to its much lower concentration of background impurities. Germanium is grown in graphite crucibles instead of silica leading to low oxygen concentrations. Additionally, the solubility of carbon in germanium is low [51] leading to low carbon impurity concentrations. In CZ germanium, we expect the group V dopant to be the only impurity present in large concentrations. Therefore the probability that primary defects have time to diffuse to each other and react before finding an impurity sink is much higher in germanium than in silicon. However, in n-type germanium, vacancies are likely negatively charged [52, 53] meaning the formation of divacancies as secondary defects is prevented by coulombic repulsion. Consequently divacancies are not expected to form in n-doped germanium irradiated by ^{60}Co, neither as a primary nor secondary defect.

However, it is still worth assessing the feasibility of other species reacting in dilute concentrations. For diffusion-limited reactions in the case of uniform initial concentrations [54], the solution for the concentration of the second order reaction of X + X → P is given by

$$\frac{1}{X} = \frac{1}{X_0} + \kappa \left[1 + \frac{2r_0}{(2\pi D t)^{1/2}} \right] t \tag{3.27}$$

where

$$\kappa = 4\pi r_0 2D \tag{3.28}$$

and D is the diffusivity of X. Assuming $r_0 = 0.5\,\text{nm}$ (separation distance between reactants needed for bonding), the diffusivity, D, required for the concentration to change from $2 \times 10^{10}\,\text{cm}^{-3}$ to $1 \times 10^{10}\,\text{cm}^{-3}$ in one day, which corresponds to the changes observed for E_{30} during the second stage of room temperature annealing of samples irradiated at 77 K (Figure 3-14), is $4.6 \times 10^{-10}\,\text{cm}^2\,\text{s}^{-1}$.

The activation energy for diffusion can be approximated from

$$D = \frac{4a^2\nu_\text{D}}{6} \exp\left(-\frac{E_\text{a}}{kT}\right) \tag{3.29}$$

where a is the spacing between sites and ν_D is the Debye frequency (assuming there are four neighboring sites). Substituting in the previously calculated value for D results in a value of 0.4 eV for E_a. This value is not unphysical and second order defect associate formation is not ruled out by kinetic considerations.

3.2.7 Summary

The defects generated by ^{60}Co in $10^{15}\,\text{cm}^{-3}$ Sb-doped germanium were characterized using DLTS to determine their electronic properties. The observed defect assignments and annealing reactions are summarized in Figure 3-19. We observed four defects states which exhibit two distinct behaviors, which we attributed to their nature as either an interstitial containing or a vacancy containing defect. E_{37}, an Sb donor-vacancy associate, decays by dissociation and vacancy diffusion to a sink present in a concentration of $10^{12}\,\text{cm}^{-3}$. E_{30}, E_{22}, and E_{21} account for the interstitials created after irradiation based on the observed formation kinetics and coupled annealing behavior. The conversion ratios of E_{30} into E_{22} and E_{22} into E_{21} suggest that E_{22} contains two interstitials. The formation behavior of E_{22} after irradiation in liquid nitrogen indicates that E_{30} is required for formation of E_{22}. Neither the mono-vacancy nor the self-interstitial could be directly observed, but their introduction rate due to ^{60}Co irradiation was found to be $\sim 2 \times 10^{11}\,\text{cm}^{-3}\,\text{Mrad}^{-1}$.

3.3 Neutron and Alpha Irradiation of Germanium

In the previous section, gamma irradiation by ^{60}Co was used to create homogeneously distributed single displacement events. An understanding of the defects formed by reactions of isolated vacancies and interstitials was developed which can be the basis upon which more complicated defect associates and reactions can be interpreted. In this section, we use alpha and neutron irradiation to generate multiple displacement events in Ge. Similar to the last section, DLTS will be used to characterize the defects observed. Dose dependences and annealing reactions can provide addition insights into the chemical nature of the defects.

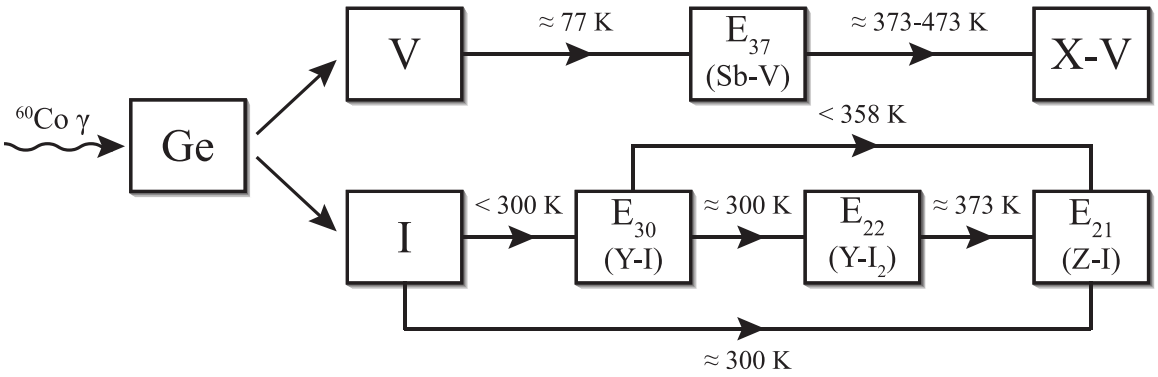

Figure 3-19: Schematic representation of defects in germanium generated by ^{60}Co irradiation and their reactions at various temperatures. X, Y, and Z stand for unknown sinks with which mono-vacancies, V, and self-interstitials, I, react.

3.3.1 Higher Mass Particle Irradiation Sources

During gamma irradiation, displacements are created by collision of compton scattered electrons with lattice atoms. Both neutrons (1.675×10^{-27} kg) and alpha particles (6.646×10^{-27} kg) have significantly larger masses than electrons (9.109×10^{-31} kg) allowing for much larger kinetic energy transfer during binary collisions. While compton scattered electrons from ^{60}Co can not impart sufficient energy to generate even two displacements (Section 3.2.1.2), both alpha and neutron irradiation sources in the energy ranges employed can impart enough energy to generate displacement cascades. In a cascade event, displaced atoms have enough kinetic energy to displace further atoms in the lattice through collisions (Figure 3-20). Successive generations of displacements will have a lower average kinetic energy and eventually displacements will stop once the transferred energies during collisions is reduced below the displacement threshold energy. Because collision cascades result in multiple displacements in close proximity, we expect higher mass particle irradiations to generate a wider variety of defect associates as primary defect associates (formed directly by irradiation) including associates which contain two or more vacancies or interstitials. In the previous gamma irradiation study, these types of associates were only produced through secondary formation processes.

Neutron Irradiation

Neutron particle radiation is dissimilar from both gamma radiation and alpha particle radiation. Unlike alpha particles, neutrons have no charge so there is no energy loss through Coulombic interactions with electrons in the target. Energy is transferred through nuclear collisions causing atomic displacements [55]. Without electronic stopping forces to lower the energy of the particle, collisions between neutrons and nuclei occur less frequently than between alpha particles and nuclei for the same particle energy. This requires the use of much higher fluences of neutrons in order to generate similar defect concentrations. Similar to gamma radiation, the penetration of neutrons into germanium is great enough to

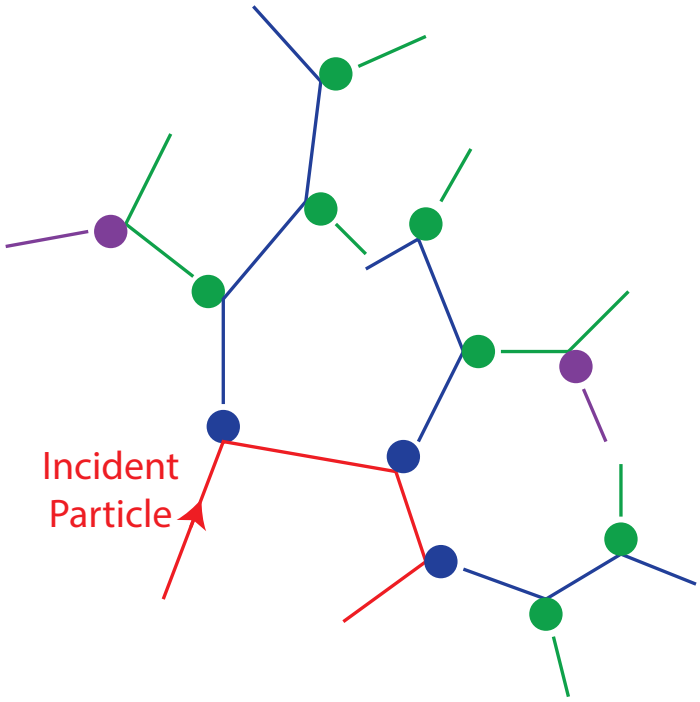

Figure 3-20: Schematic of a collision cascade event with differing colors representing successive generations (primary, secondary, and tertiary) of recoil atoms.

assume that collisions between neutrons and nuclei are homogenously distributed within the material (based on the thickness of Ge samples). However, neutrons are able to transfer a large amount of energy to the individual displaced atoms making collision cascades likely.

Alpha Irradiation

Unlike gamma rays and neutron radiation, alpha particles (He^{2+}) are charged causing a quicker loss of energy as they pass through matter; energy is slowly lost through inelastic scattering with electrons in the medium. As the incident particle slows down, the probability of elastically colliding with nuclei in the material increases and eventually becomes the primary energy loss mechanism. These collisions will create displacements if the energy transferred is greater than the displacement threshold energy. Often, the transferred energy is large enough that the recoiled atom can undergo further collisions with atoms thus displacing multiple atoms per incident alpha particle. Because the majority of displacements are generated by nuclear collisions some distance into the material (after sufficient energy has been lost to electronic interactions), alpha irradiation results in a non-homogeneous defect distribution. Defect distributions can be simulated using SRIM[1] to calculate the distribution of displacement events [56]. Figure 3-21 shows a SRIM simulation for the defect distribution generated by the irradiation energy used in this work (6 MeV). SRIM does not account for any self annihilation of Frenkel pairs and is therefore not suitable for

[1]Available at www.SRIM.org

determining accurate introduction rates of stable defects.

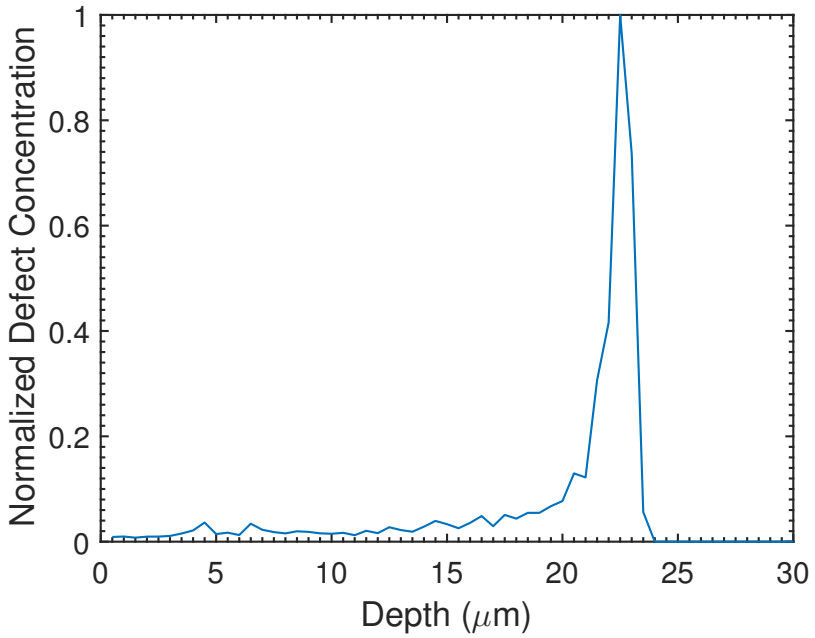

Figure 3-21: SRIM simulation for defect distribution produced by irradiation of Ge with 6 MeV alpha particles.

3.3.2 Experimental Parameters

This work uses the same materials (1×10^{15} cm^{-3} Sb-doped Ge) and procedures used for fabrication and annealing of Schottky diodes in Ge in Section 3.2.2. Neutron irradiations were performed by the MIT Nuclear Reactor Laboratory in the MITR-II experimental fission reactor facility. Samples were irradiated at two different locations within the reactor. The first reactor location bombards the samples with both fast (~1 MeV) and slow/thermal (<1 eV) neutrons. Slow neutrons cannot directly displace atoms creating defects but are easily captured by atoms causing transmutation which is often accompanied by high energy gamma irradiation. Samples are also irradiated in a location where they are bombarded by only slow neutrons. The dose of slow neutrons is matched at both locations so that the defects which are related to fast neutrons only can be calculated.

Alpha irradiations in this work were performed using an ion accelerator at the Pacific Northwest National Laboratory (PNNL). Samples were irradiated with particle energies of 6 MeV for doses of 1×10^8 cm^{-2}, 5×10^8 cm^{-2}, 1×10^9 cm^{-2}, and 5×10^9 cm^{-2}. 1×10^8 cm^{-2} was the lowest dose available in the ion accelerator facility. The end of range damage is located ~20 µm from the surface. During DLTS measurements, the voltage pulses used only modulate the depletion width a few micrometers. Therefore, the presented alpha irradiation studies probe a region of the sample where electronic stopping forces create most of the damage. These parameters were chosen for two reasons. First, the end of range damage for the lowest available dose of 1×10^8 cm^{-2} generates more defects than the

dopant concentration leading to compensation and inaccuracy of DLTS measurements (no longer operating in the small signal regime). Secondly, while collision cascades are more prevalent at the end of range, they still occur within the probed region. Therefore, we can investigate the difference between defects (and their concentrations) generated by neutron irradiation in which collision cascades are more dominant and electronic stopping range alpha irradiation.

3.3.3 Defect States

DLTS spectra for 1×10^{15} cm^{-3} Sb-doped germanium irradiated with fast + slow neutrons and only slow neutrons at room temperature (300 K) are shown in Figure 3-22. A third line is plotted from the difference of the two irradiations to show the portion of the fast + slow neutron spectra resulting from only fast neutron damage. The fast neutron fluence was 10^{13} cm^{-2} which is the lower limit of doses with which the irradiation facility can accurately bombard samples. The slow neutron only spectrum is very similar to those generated by ^{60}Co gamma irradiation and the electronic signatures of the defects match indicating that the same defects are generated by both radiation types. The spectrum for damage created by fast neutrons also contains the defects seen after ^{60}Co gamma irradiation, however, new peaks appear indicating the generation of new defect states. Because fast neutron damage is expected to generate collision cascades, it is likely that the new defect states are related to the presence of multiple vacancies or multiple interstitials. The new features observed in the fast neutron spectrum are relatively broad making visual identification of individual defect states by conventional DLTS difficult. One way to improve the ability to visually distinguish overlapping defects in a DLTS conventional spectra is to compare spectra with different filling pulses (varying capture cross sections will show varying rates of signal saturation). Because Laplace DLTS gives the highest resolution, we have used that to identify 11 distinct defect states whose locations are roughly signified on a plot of conventional spectra taken with varying pulse widths (Figure 3-23). Of the 11 observed defect states, 3 were previously generated by gamma irradiations (E_{37}, E_{22}, and E_{21}). The newly observed defects are also named based on their apparent enthalpies but have been given a prefix of N to signify that they were observed after neutron irradiation. Figure 3-24 shows emission rate vs. temperature data for defect states observed after neutron irradiation. This data was analyzed to extract apparent activation enthalpies and apparent capture cross sections. Pulse-filling measurements were performed at various temperatures to measure real capture cross sections and determine temperature dependencies if present for 5 of the newly observed defects. Accurate capture cross section measurements for 3 of the defects were not possible due to difficulty of deconvolution of defect states even with Laplace DLTS. A summary of properties extracted from DLTS measurements for the observed defect states after neutron irradiation at 300 K is listed in Table 3.4. Measurements of alpha irradiated samples show the generation of the same defects as after neutron irradiation but in lower concentrations relative to the defects generated by single displacements after gamma irradiation. This is consistent with our expectation that the depth of the material probed in alpha irradiated samples have less collision cascades than the bulk of the neutron irradiated material.

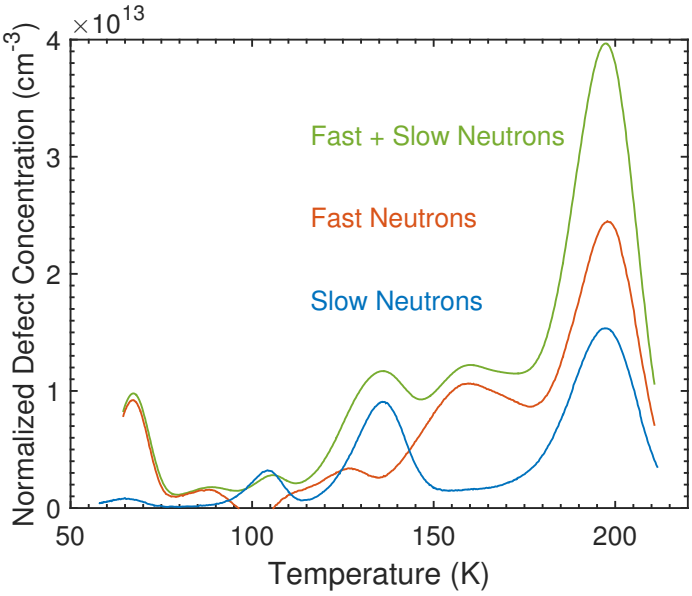

Figure 3-22: DLTS spectra for neutron irradiated Sb-doped Ge samples.

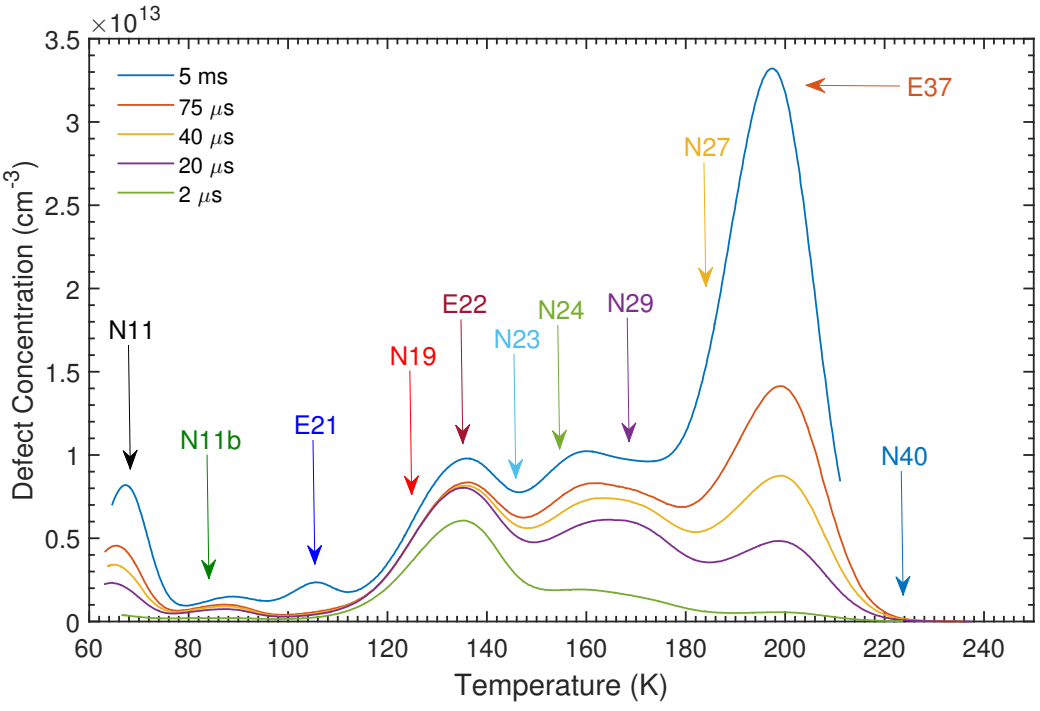

Figure 3-23: Conventional DLTS spectra obtained with varying pulse widths after fast + slow neutron irradiation labeled with the names of distinct defect states identified using Laplace DLTS.

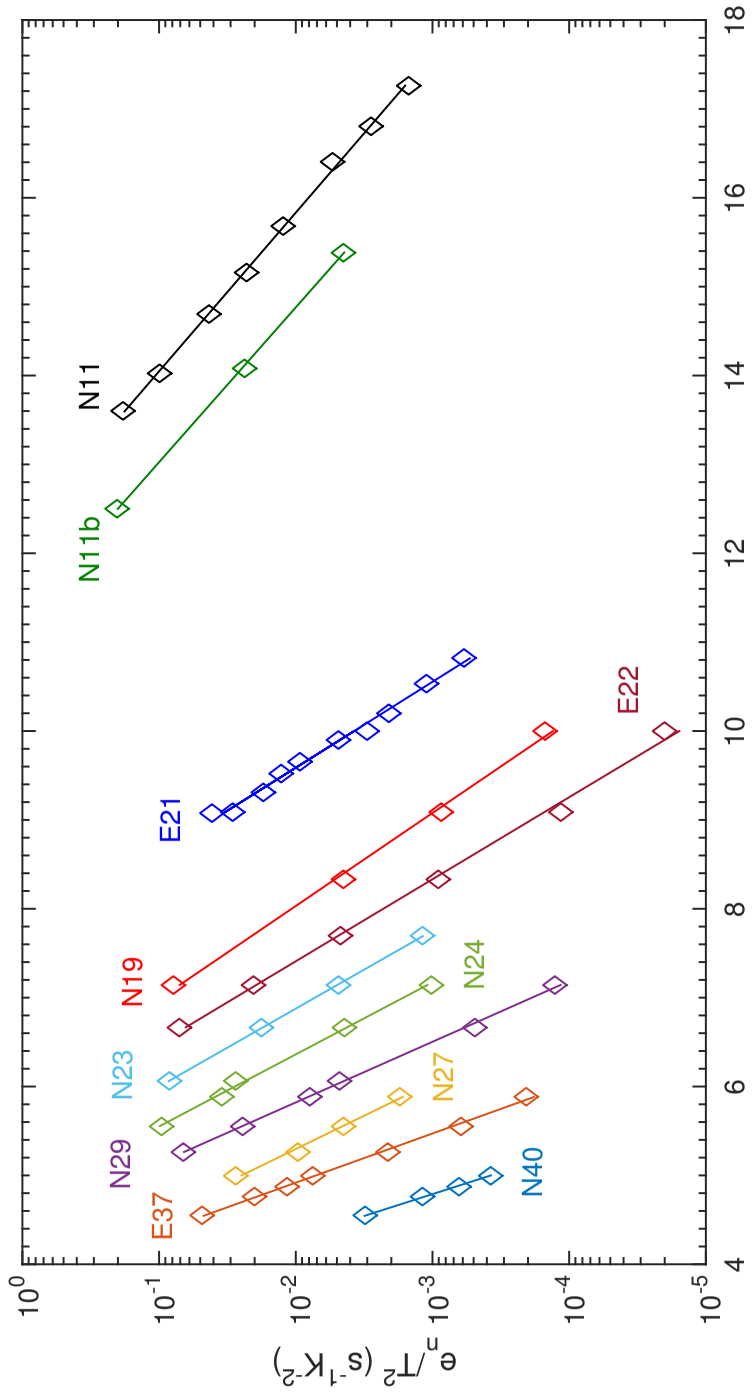

Figure 3-24: Defect states observed after neutron and alpha irradiation of Sb-doped n-type germanium.

Table 3.4: Summary of defect states observed after neutron and alpha irradiation of Sb-doped germanium

Defect	Apparent Enthalpy (eV)	Free Energy of Ionization (eV)	Apparent Capture Cross Section (cm^2)	Real Capture Cross Section (cm^2)
N_{40}	0.40	NA[a]	1×10^{-15}	NA[a]
N_{27}	0.27	$0.13 + 6.22kT$	3×10^{-17}	$1.5 \times 10^{-14} e^{-142\,meV/kT}$
N_{29}	0.29	$0.29 - 4.4kT$	9×10^{-16}	1.1×10^{-17}
N_{24}	0.24	$0.22 - 1.29kT$	2×10^{-16}	$5.5 \times 10^{-17} e^{-16\,meV/kT}$
N_{23}	0.23	$0.20 - 0.43kT$	2×10^{-16}	$1.3 \times 10^{-16} e^{-24\,meV/kT}$
N_{19}	0.19	$0.17 + 1.44kT$	1×10^{-16}	$4.2 \times 10^{-16} e^{-17\,meV/kT}$
N_{11}	0.11	NA[a]	2×10^{-15}	NA[a]
N_{11b}	0.11	NA[a]	8×10^{-16}	NA[a]

[a] Unknown due to difficulty of deconvolution from nearby peaks by Laplace DLTS

3.4 Future Work

We have characterized the electronic properties of defects generated by neutron and alpha irradiation. This information is useful for predicting the impact of these defect states on devices. However, more information is required to make defect assignments. As mentioned previously, the large number of defect states generated by higher mass particle irradiation sources complicates analysis and is one of the reasons for lack of agreement about defect assignments in the literature. The following sections describe preliminary results from two experiments which can potentially help determine the chemical nature of defects in the future with more data.

3.4.1 Concentration Dependence on Alpha Dose

Looking at the dependence of defect concentrations on dose can provide information about defect formation mechanisms. Samples were sent for alpha irradiation at four doses (Section 3.3.2). Unfortunately, the highest dose creates too much damage making defect concentration measurements not possible. In addition there may have been experimental issues during bombardment at the second highest dose making those samples untrustworthy. Figure 3-25 shows a plot defect concentration vs dose showing a linear relationship for four of the defects associated with generation by collision cascades in alpha and neutron irradiations indicating that these are defects scale with the generation of collision cascades. N_{23} does not show a strong linear fit indicating that it's formation may be diffusion limited like E_{22}. The other defects were present in concentrations too close to the noise level to analyze. However, this data is far from conclusive since measurements from only two doses exist and the linear fits are made with only three points. A greater range of doses are required to ensure that there really is a linear dependence on dose for these defects.

3.4.2 Alpha/Neutron Generated Defect Reactions

Similar annealing studies on alpha and neutron irradiated samples as performed on gamma irradiated samples would provide a great deal of data which could lead to defect assignments. Determining annealing reaction parameters would enable determination of links between defect states including if multiple observed states are related to the same defect association. Figure 3-26 shows some preliminary for alpha irradiated germanium annealed for 1 min at various temperatures. Unlike after gamma irradiation of germanium, a 1:2 conversion of E_{22} into E_{21} is no longer observed. However, there is what initially appears to be a large decrease in E_{37} that quickly saturates which is unusual. One possibility is that the apparent decrease in E_{37} is due to a decrease in N_{27}. It is also possible that the decay of N_{27} may also be related to the difference in conversion ratio of E_{22} into E_{21} compared to gamma irradiation. More detailed experiments (including isothermal anneals) are required to measure the reaction kinetics and determine if these processes are actually related.

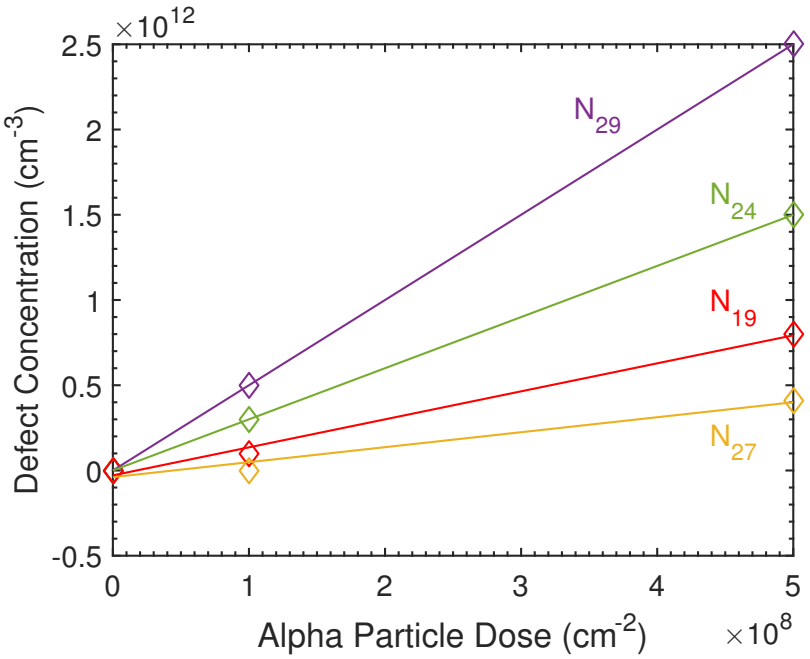

Figure 3-25: Linear concentration dependence on dose for defects generated by 6 MeV alpha irradiation of Ge.

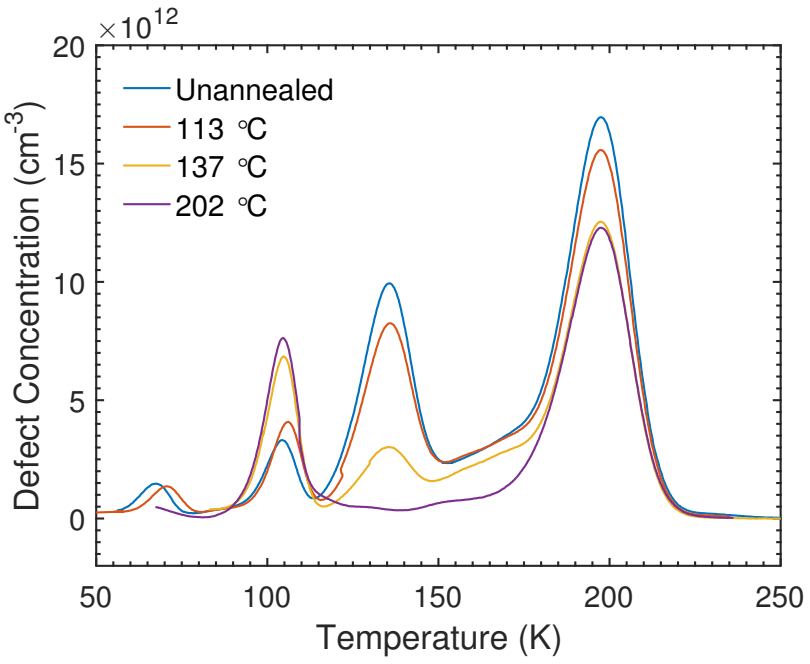

Figure 3-26: DLTS spectra from isochronal annealing of 6 MeV alpha irradiated germanium.

Chapter 4

Germanium-on-Silicon Laser

A key application for an on-chip light source is in high performance computing. For decades, the microelectronics industry has been driven to continually scale down components in order to follow Moore's Law [58] which states that the number of transistors on a microprocessor chip will double approximately every two years. In the past, the shrinking of component sizes has lead to equally impressive gains in computing performance. However, continued scaling has become increasingly difficult. Eventually fundamental limits will be reached requiring innovation beyond component scaling for performance improvements in the future. 2016 is the first year that the International Technology Roadmap for Semiconductors (ITRS) is not centered around continuation of Moore's Law.

As seen in Figure 4-1, while the number of transistors per chip has steadily increased over time, clock speeds saturated in the early 2000s [59] due to limitations imposed by the excess heat generated at high clock speeds. A large factor for the increased power dissipation is the increase in the RC delay of the electrical interconnects. When scaling components, shrinking wire diameters increase resistance while decreasing wire pitches increase capacitance. In order to continue increasing performance, chips are now manufactured with multiple processors (also referred to as "cores"). However, this method also cannot scale indefinitely as communication between distant components requires increasing bandwidth and power consumption requirements which cannot be satisfied by electrical interconnects. One potential solution is to switch to optical interconnects which can provide higher bandwidth density at lower energy costs [1, 2].

Building CMOS compatible optical interconnect systems using a silicon microphotonics platform will facilitate integration of optical interconnects with established microelectronics architectures . Furthermore, fabrication of silicon microphotonic components can leverage processing techniques and equipment developed by the microelectronics industry to reduce costs [3]. A complete optical interconnect system requires all the components needed to make electrical to optical (EO) and optical to electrical (OE) signal transformations. For systems operating in the near-IR, silicon itself provides a satisfactory material for fabrication of passive components such as waveguides and ring resonator filters. Single mode silicon waveguides can be fabricated with optical losses less than 1 dB cm^{-1} [60]. Additionally, high

The work in this chapter is partially adapted from [57] and was done in collaboration with R. Camacho-Aguilera and Y. Cai, also members of the Kimerling group at MIT.

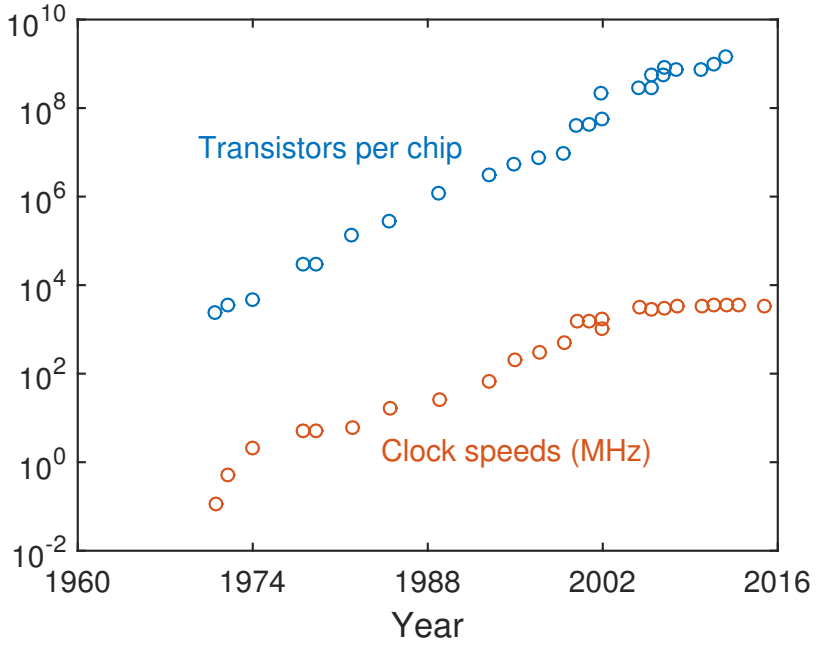

Figure 4-1: The number of transistors per chip has steadily increased demonstrating a continuation of Moore's law over time. However, clock speeds saturated in the early 2000s. *Reproduced from [59]*

performance active germanium devices for signal modulation [21] and detection [17] have been demonstrated which are easily integrated onto a silicon platform due to the ability to epitaxially grow germanium on silicon.

However, integration of a light source has proven more difficult [61]. Within silicon, a variety of approaches have been proposed for development of silicon light sources including stimulated Raman scattering [62, 63], Si nanocrystals [64], and rare earth doping [65]. However, these devices are not entirely suitable for optical interconnect systems where efficient operation under electrical pumping is required. Another approach which enables electrical pumping is to integrate III-V active materials with a silicon platform either through epitaxial growth on Si (large lattice mismatch requires thick buffer layers) or hybrid integration through chip-bonding processes (high cost, low yield) [66–69]. The ability to use germanium as the material for all active devices (light sources, modulators, and photodetectors) on a Si microphotonics platform would significantly simplify integration of photonic components with CMOS electronics. In this chapter, we demonstrate that germanium, which is typically considered a poor candidate for light emission applications due to its indirect bandgap, can form the basis of a monolithically integrated electrically pumped light source for silicon microphotonics. In addition, we model the impact of dislocations on device performance due to increased SRH recombination.

4.1 Background

The band structures of semiconductor materials can be classified as either direct or indirect depending on whether the conduction band minimum and valence band maximum are located at the same (direct) or different (indirect) values of crystal momentum (or **k**-vector). Radiative recombination through annhilation of an electron in the conduction band with a hole in the valence band requires conservation of both energy and crystal momentum. Conservation of crystal momentum is easily achieved for carriers at the band minimum and maximum for direct bandgap materials. However, for recombination to occur in an indirect bandgap material, the difference in crystal momentum between electrons and holes must be made up by absorption or emission of a phonon (Figure 4-2). The requirement of a phonon makes radiative recombination a less probable event and therefore a significantly slower, less efficient process in indirect bandgap materials compared to direct bandgap materials. For this reason, semiconductor diode laser active regions are typically fabricated from direct bandgap materials.

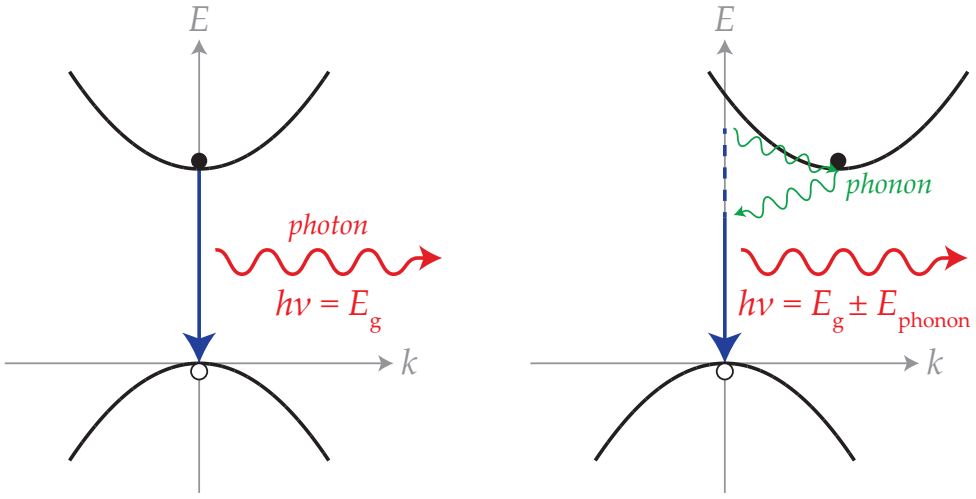

(a) Direct bandgap (b) Indirect bandgap

Figure 4-2: Comparison of radiative recombination for (a) direct vs. (b) indirect bandgap materials.

While germanium is technically an indirect bandgap material, the energy difference between the Γ valley (direct) and L valley (indirect) is only 136 meV (Figure 4-3a). This small difference has lead to proposals of lasing in Ge by injection of carriers into the Γ valley as early as 1963 [70]. However, many decades passed before optical gain was was first achieved through a combination of tensile strain and n-type doping (observed in 2009 [71] by Liu et al.). Biaxial tensile straining of Ge leads to the shrinking of both the direct and indirect bandgaps (Figure 4-3b) but the Γ valley shrinks quicker than the L valley due to the smaller effective mass of the carriers in the Γ valley [72]. Therefore, strained germanium can be made into a direct bandgap material with 2 % strain. This amount of strain is difficult to achieve and also results in a bandgap of ~0.5 eV which would correspond to emission

at a wavelength of ~2500 nm. It is more desirable to have emission in a wavelength range closer to standard communications wavelengths of ~1550 nm where mature technologies for modulation and detection exist. In addition, photodetectors designed for operation at longer wavelengths would need smaller bandgaps which would significantly increase leakage current. Instead, germanium can be slightly strained (0.2 % to 0.3 %) and highly n-type doped to yield a pseudo-direct bandgap (Figure 4-3c). When the n-type doping concentration is ~10^{19} cm^{-3}, the lower energy states in the L valley become occupied. When electrons are now injected, some electrons will occupy the Γ valley and can thus efficiently radiatively recombine with holes in the valence band. In addition, the higher recombination rate of electrons in the Γ valley leads to inter-valley scattering of electrons from the L valley to the Γ valley in order to maintain quasi-equilibrium in the conduction band. This further increases the efficiency of radiative recombination from the Γ valley. Theoretically predicted gain spectra for 0.25 % strained mid-1 × 10^{19} cm^{-3} doped germanium show broad net gain is possible from 1550 nm to 1600 nm. This would suggest that a germanium laser would be suitable for on-chip wavelength division multiplexing (WDM) applications.

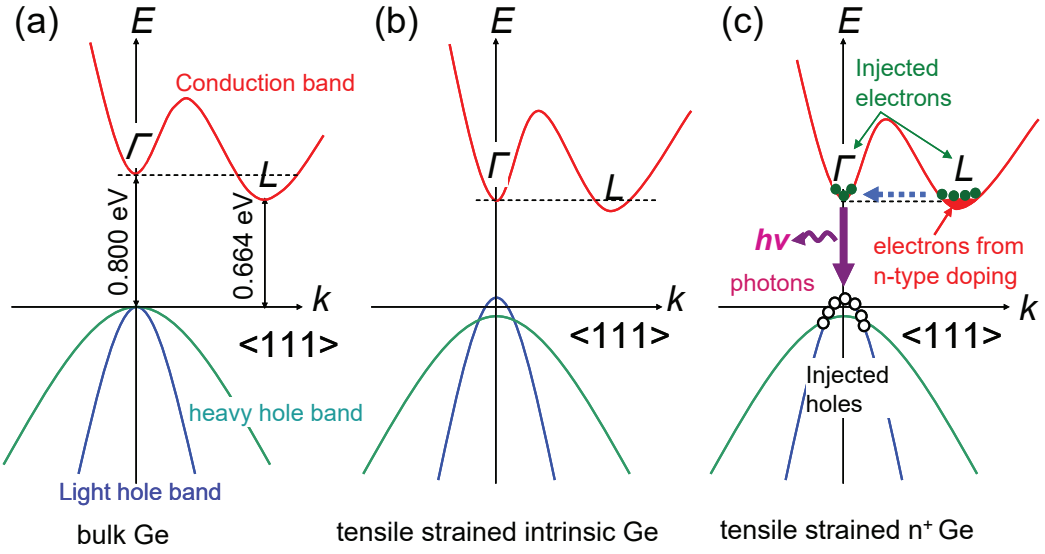

Figure 4-3: Schematic band structure of (a) bulk germanium, (b) tensile strained intrinsic Ge, and (c) tensile strained n^+ Ge. *Reprinted from [73] with permission*

4.2 Ge Laser Fabrication and Design

This section contains a brief overview of processes crucial to the development of a Ge laser largely developed by collaborators, primarily R. Camacho-Aguilera [74] and Y. Cai [75] (see the referenced theses for more details).

4.2.1 Epitaxial Growth of Ge on Si via UHVCVD

Integral to implementation of an integrated germanium laser on silicon is the growth of high quality germanium on silicon. Heteroepitaxy of Ge on Si can be challenging due to the difference of lattice constants between Si (5.431 Å) and Ge (5.658 Å). The 4 % lattice mismatch leads to islanding of Ge when the thickness reaches a critical thickness (Stranski–Krastanov growth). One approach to fabricating uniform films is to gradually grade the composition of a SiGe buffer layer so that the strain is never large enough to force islanding [76]. However, this method requires thick buffer layers which can be time consuming and costly to fabricate. In addition, for many integrated microphotonic applications, it is desirable to be able to fabricate the germanium devices close to the silicon (without a thick buffer) in order to couple light from passive to active components and vice versa. Another approach, which is used in this work, is to instead use a two-step ultra-high vacuum chemical vapor deposition (UHVCVD) growth process whereby an initial low temperature (360 °C) growth is used to make a continuous and thin (40 nm to 60 nm) buffer layer which accommodates strain in the germanium [77]. As previously mentioned, Ge will island to relieve strain that builds up the film thickness increases. However, during a low temperature growth, Ge is not mobile enough to island. Strain is instead released through the nucleation of misfit dislocations (Section 2.2.2). Once the strain has been completely relaxed, the growth temperature is increased (650 °C to 780 °C) to grow high quality Ge via homoepitaxy. Threading dislocation densities after growth are typically as high as $10^8\,\mathrm{cm}^{-2}$ to $10^9\,\mathrm{cm}^{-2}$. However, annealing or cyclic annealing of films at high temperatures can reduce threading dislocation densities down to $\sim 2 \times 10^7\,\mathrm{cm}^{-2}$ for 1 µm thick blanket films or $\sim 1 \times 10^6\,\mathrm{cm}^{-2}$ for 10 µm × 10 µm mesas selectively grown in SiO_2 trenches [77].

High temperature growth and annealing steps also play a crucial role in introducing tensile strain to the film which is necessary for a pseudo-direct bandgap (Section 4.1). A common misconception is that Ge will be placed into compressive strain due to its larger lattice constant compared to Si. This would be true for very thin films which would grow pseudomorphically. However, for practical Ge devices, in order to confine light at ~1550 nm, film thicknesses would need to be at least a few hundred nanometers. This is much thicker than the critical thickness for pseudomorphic growth and instead during the high temperature anneal (or high temperature Ge growth step), the material becomes completely strain relaxed through nucleation of misfit dislocations. However, upon cooling to room temperature, germanium will shrink more than silicon due to a larger coefficient of thermal expansion. This places the germanium film into a state of biaxial tensile strain which can be calculated from

$$\varepsilon = \int_{T_\mathrm{f}}^{T_\mathrm{i}} (\alpha_\mathrm{Ge} - \alpha_\mathrm{Si})\,\mathrm{d}T \tag{4.1}$$

where T_i and T_f are the initial and final (room) temperatures, α_Ge is the linear expansion coefficient of Ge ($5.9 \times 10^{-6}\,^\circ\mathrm{C}^{-1}$), and α_Si is the linear expansion coefficient of Si ($2.6 \times 10^{-6}\,^\circ\mathrm{C}^{-1}$). Experimentally, annealing temperatures between 650 °C to 850 °C will lead to measured tensile strains of 0.2 % to 0.25 %.

UHVCVD growth of Ge occurs selectively on Si but not on SiO_2 which has two significant

benefits. The first is that Ge structures can be defined in the material without first depositing a blanket film and then etching. Dry etching of Ge can lead to rough sidewalls (optical scattering) and dangling bonds (carrier recombination) which would contribute to poor device performance. Instead of requiring passivation after etching, Ge grown within trenches are already passivated by the oxide trench walls. The second benefit is that the oxide walls provide a surface for threading dislocations to annihilate at during annealing. Therefore, lower threading dislocation densities can be achieved for confined Ge structures vs. blanket films.

4.2.2 Germanium n-type Doping

Net optical gain (which is a requirement for lasing) is observed when the optical gain exceeds the losses in the system, a major loss being free carrier absorption (FCA). Previously, both net optical gain and optically pumped lasing [78] have been demonstrated from 10^{19} cm^{-3} n-type doped, tensile-strained germanium showing that overcoming FCA is possible in order to attain net gains of ~50 cm^{-1}. However, electrically pumped laser designs contain significant additional losses (>100 cm^{-1} from free carrier absorption in heavily doped electrodes (required for efficient carrier injection). To overcome these additional losses, increased n-type doping levels are required in order to boost the optical gain from Ge [79].

Germanium can be doped *in situ* with phosphorous during UHVCVD growth by use of PH_3. However, the maximum activated phosphorous concentration is limited to ~2×10^{19} cm^{-3} for growth temperatures 600 °C to 700 °C [80]. Above ~750 °C, phosphorous out diffuses and evaporates reducing n-type doping concentrations. Greater concentrations can be achieved during low temperature Ge growths but results in poorer quality Ge material [81]. Ion implantation is commonly used process for introduction of dopant atoms in microelectronics circuits. However, implantation requires bombarding the material with high energy ions which creates significant numbers of defects which will act as non-radiative recombination centers reducing device performance. Annealing can be used to remove implantation damage but can also result in dopant out-diffusion ultimately limiting the doping concentration.

In our work, we use a delta-doping approach to obtain n-type doping concentration >4×10^{19} cm^{-3} while maintaining good material quaility [82]. After CVD growth of the active layer Ge film, alternative layers of P monolayers and intrinsic Ge are grown at low temperatures (450 °C and 400 °C respectively) to form a delta layer stack with a large P concentration which can act as a P source for indiffusion (Figure 4-4). The diffusivity of P atoms varies quadratically with concentration which allows for in-diffusion during annealing to beat out-diffusion to the Ge surface and Ge/Si interface creating uniform doping profiles in the active Ge region [83].

4.2.3 $p^+Si/n^+Ge/n^+Si$ Double Heterostructure

The overall device structure must be designed in order to allow for efficient electron and hole injection throughout the active germanium region. Most common III-V diode lasers implement a double heterostructure design where a lower bandgap material (active device layer) is sandwiched between a larger bandgap material [84]. This allows for confinement

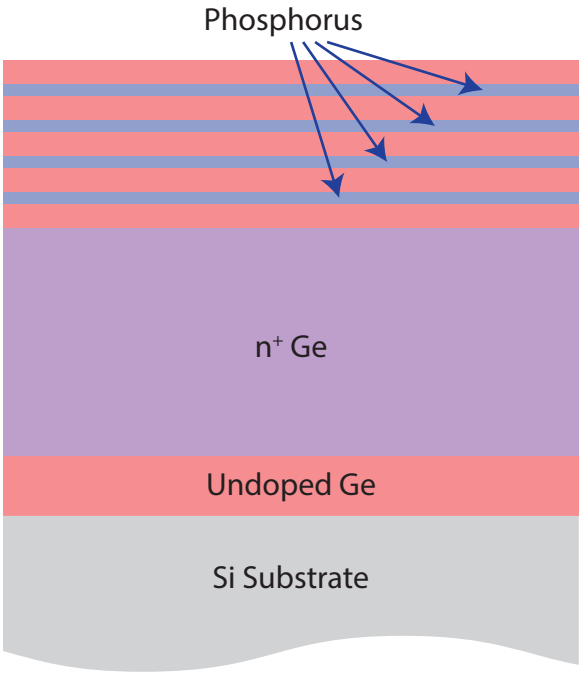

Figure 4-4: Schematic of delta doping layers which act as a dopant reservoir for phosphorous atoms

of both free carriers and light to the active region improving laser efficiency. Our work also utilizes a double heterostructure design by confining carriers and photons to Ge by sandwiching it between the n^+Si substrate on which Ge is grown and a p^+ plasma enhanced CVD (PECVD) deposited film of amorphous silicon into which boron is implanted. In addition to the active region being composed of an indirect bandgap material, our laser design is different from typical III-V heterostructure designs in two significant ways. First, typical double heterostructure devices utilize a p-i-n diode whereas we employ a p-n-n structure. This may lead to concerns that a junction only forms at the n^+Ge/p^+Si interface. However, simulations show that the heavy doping of silicon leads to built-in voltages at both interfaces allowing for injection of electrons and holes throughout the entire Ge region[79]. Second, in III-V lasers, the two different semiconductors are chosen such that the heterostructure has a Type-I band alignment where as Si/Ge interfaces typically show Type-II band alignment. This may lead to concerns that sufficient injection of carriers into this structure is not possible. Figure 4-5 shows a simulation of the heterostructure bands which predicts that due to the heavy n-type doping of Ge, under forward bias, band bending creates a pseudo Type-I alignment [73]. Furthermore, predicted carrier concentrations shows that large hole concentrations can be achieved in the active region despite its heavy n-type doping. Therefore, a p^+Si/n^+Ge/n^+Si double heterostructure is a suitable design for development of an electrically pumped laser.

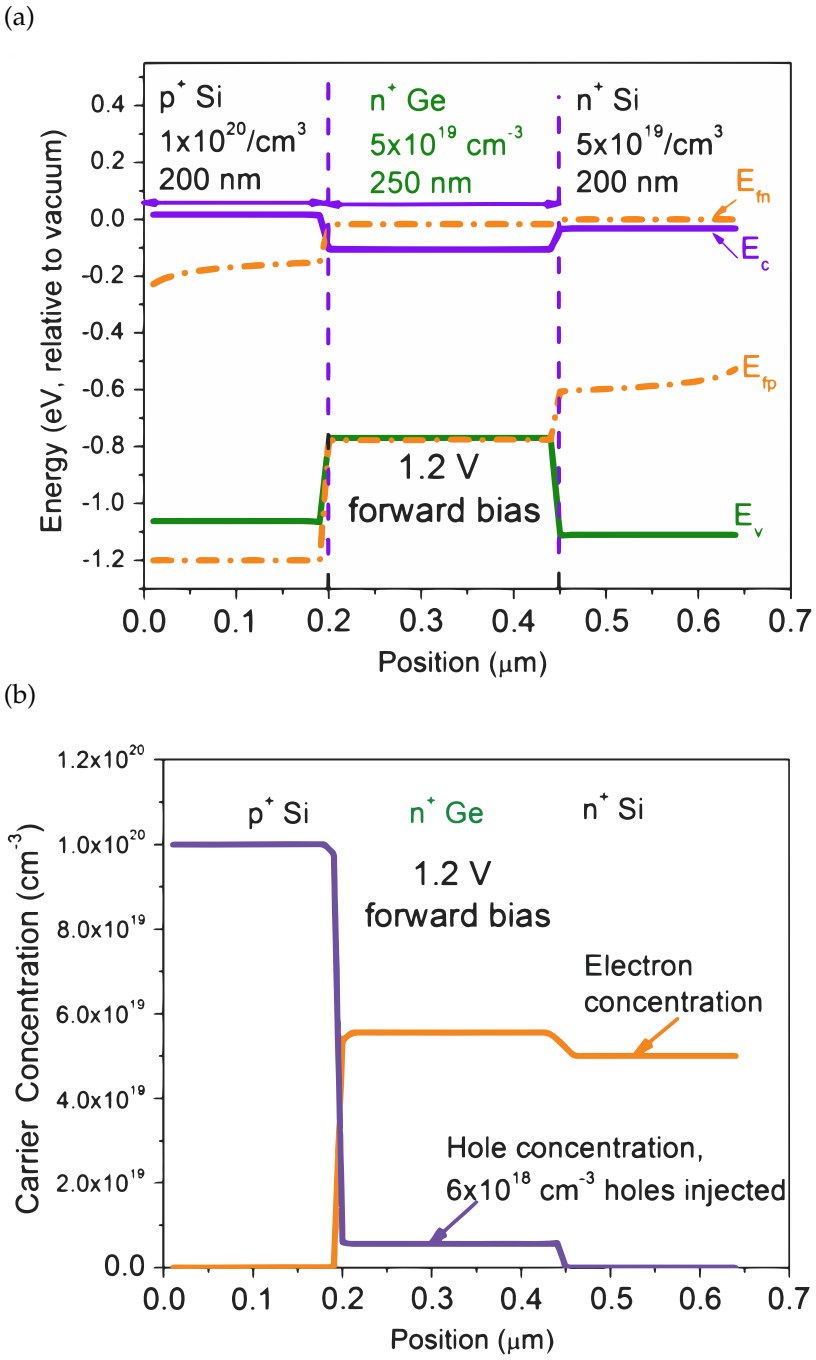

Figure 4-5: Simulation of $p^+Si/n^+Ge/n^+Si$ double heterostructure (a) bands and (b) carrier concentrations during electrical injection at 1.2 V. *Reprinted from [73] with permission*

4.2.4 Laser Structure

Now that we have a process for making a gain medium from germanium, in order to demonstrate lasing, the gain medium needs to be placed within a resonant optical cavity. For demonstration of the feasibility of lasing from germanium, we implemented a Fabry-Pérot cavity (two mirrors placed parallel) which is the simplest design to fabricate and test. In this case, a straight waveguide is fabricated in Ge and the ends act as mirrors due to the large change in refractive index between Ge and the surrounding environment. Samples are cleaved to expose the Ge facets at one end of the waveguide in order to collect emission for measurements and forms one mirror. The lithographically defined Ge/oxide interface at the other end of the waveguide acts as the second mirror. Devices were fabricated with cavities ranging from a few hundred micrometers to several millimeters.

Figure 4-6 contains a schematic of the cross-section of the complete Ge Fabry-Pérot laser structure including a metal contact stack of Ti-Al-Ti (100 nm-1 µm-100 nm) which cover the entire length of the p^+ polySi layer (180 nm thick) in order to provide uniform electrical injection into the underlying Ge. Not shown in the schematic is a similar Ti-Al-Ti stack which is deposited directly onto the n^+ substrate from the top in order to fabricate the second contact. Al was sandwiched between Ti layers in order to minimize failure from electromigration.

Ge was grown into 1 µm oxide trenches. Chemical mechanical polishing (CMP) is required to remove the poor quality Ge grown on the surface during delta doping. Imprecision of the Ge CMP process resulted in devices with Ge thicknesses ranging from approximately 100 nm to 500 nm. After cleaving samples, a thin 15 nm oxide film is deposited onto the exposed Ge facet mirror in order to protect it from failure due to high optical fields generated during device testing.

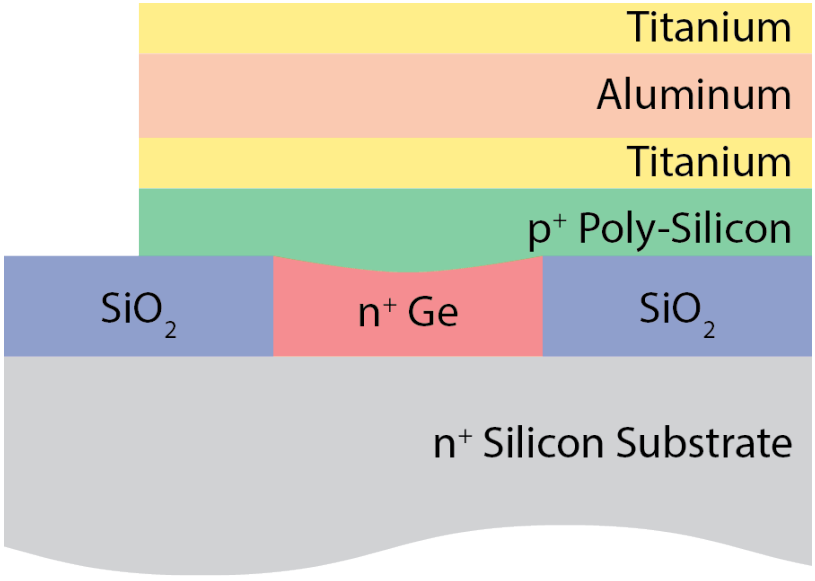

Figure 4-6: Schematic cross-section of the Fabry-Pérot germanium laser structure.

4.3 Electrical Pumping of Ge Laser Diodes

4.3.1 Experimental Apparatus

Emission from the laser devices was collected and measured using a Horiba micro-photoluminescence (PL) system equipped with a LN_2 cooled InGaAs photodetector. The micro-PL system collects light through a microscope objective and passes it through a diffraction grating which acts as a monochromator before being collected at the detector. Emission spectra are obtained by sequentially varying the wavelengths allowed through the monochromator. The resolution of the obtained spectrum is determined by the step size and slit width and has been calibrated using a narrow linewidth commercial 1550 nm laser. In our experiments, the resolution varies from approximately 10 nm (wide slit width for maximum signal intensity) to 1 nm.

After cleaving to form mirror facets, chips containing a row of lasers were mounted to a metal block which is cooled by a thermoelectric cooler whose hot-side is actively cooled using a LN_2 cooling system. A thermocouple is used to measure the temperature of the metal block as close to the sample as possible and provide feedback for the thermoelectric cooler. The temperature was maintained at 15 °C for electrical pumping measurements. Nitrogen gas was gently flown over the samples to prevent any condensation that may from due to cooling.

Samples are oriented such that the emission is directed into the microscope objective of the micro-PL system. The system contains a switch to allow for light collected from the objective to be fed to a camera which aids in alignment of the Ge facets for efficient collection. A second camera is oriented perpendicular to the microscope objective and is used to give a top-down view of the chip for contacting to the metal pads with tungsten probe tips using XYZ micromanipulator stages. Electrical injection is supplied by a constant current pulsed laser driver whose pulsed signal is sent to a lock-in amplifier to be used as a reference for improving signal/noise from the photodetector. A schematic of the laser emission measurement setup is found in Figure 4-7.

4.3.2 Demonstration of Electrically Pumped Lasing

Initial testing of devices at large duty cycles (~50 %) yielded ambiguous results regarding whether lasing was occurring. At low injection current densities, no emission was detectable but for some devices a threshold was seen where a brief but intense signal detection was observed followed quickly by device failure. The time before failure was quick enough that spectra and accurate determination of emission center wavelengths were unobtainable. Some devices failed before observation of emission which was likely a result of the monochromator never sweeping the emission wavelength before device failure.

Even though samples are cooled to 15 °C with a thermoelectric cooler, local heating in the device can be much greater and possibly leading to the observed failure. To reduce heating due to the injection current, shorter duty cycles (~4 %) were implemented. Initially, similar brief intense emission events were not observed even though devices were not exhibiting failure. The current was then directly measured using an inductive sensor connected to an oscilloscope in order to verify that the intended pulses are being generated. For the

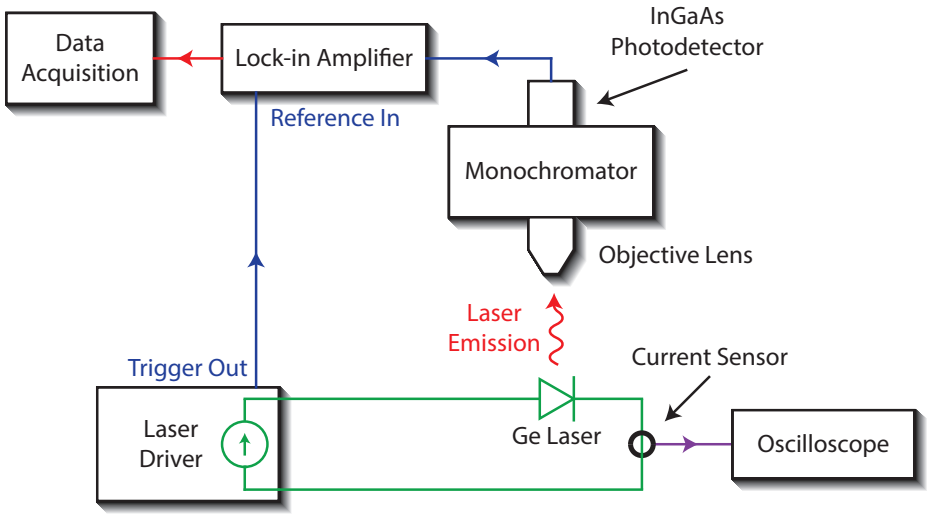

Figure 4-7: Schematic of the experimental setup used to measure the emission spectra from Ge laser devices

tested short duty cycles with pulses below 100 µs, the pulse were not well formed indicating that emission was not observed due to insufficient current injection. The entire electrical signal line was then impedance matched to 50 Ω in order to reduce reflections and enabled well-formed square injection pulses at short pulse widths.

With proper current injection at low duty cycles, emission events lasted several minutes and allowed for measurement of emission spectra. Figure 4-8 shows emission spectra for varying current densities for a device injected at 800 Hz with a 4 % duty cycle (50 µs pulse width). At 90 kA cm^{-2}, no emission is observable above the noise level of the measurement. However, as soon as emission appears around injection at 511 kA cm^{-2}, the observed spectrum has a linewidth consistent with lasing and significantly narrower than the broad spectra (from 1500 nm to 1700 nm) observed from previous electroluminescence measurements from lower n-typed doped Ge LEDs [85]. The spectra interestingly shows two peaks (1533 nm and 1535 nm) which are possibly related to mode hopping between or multimode emission from two different cavity modes (consistent with the estimated free spectral range of 1 nm for the device cavity). The individual linewidths correspond to the resolution limit for the slit width during measurements indicating that the actual emission linewidths from our Ge laser devices are <1.2 nm.

Due to variations in Ge thickness (from poor control of CMP) and mirror quality (from poor control of facet quality when cleaving), tested devices showed a wide range of emission wavelengths, threshold currents, and operating lifetimes. In general, shorter operating lifetimes were observed for devices which showed larger threshold currents. A device which showed stable operation after observation of emission at 1650 nm was used to generate the L-I (light intensity vs. current) plot seen in Figure 4-9. A clear change in slope can be see at ~280 kA cm^{-2} indicating lasing threshold behavior as gain surpasses the optical losses and further injection leads to stimulated emission. Ultimately, the device failed limiting our ability to measure optical output for larger current densities. The signal

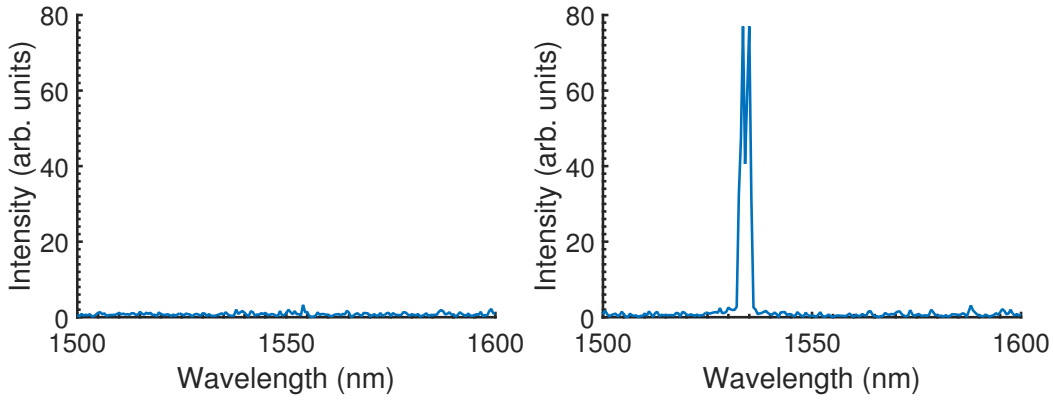

Figure 4-8: Ge laser emission spectra for varying current densities of a) 90 kA cm^{-2} and b) 511 kA cm^{-2} showing threshold behavior when injected at 800 Hz with a 4 % duty cycle (50 µs pulse width). Slit width corresponds to a spectral resolution of ~1.2 nm. Sample had a cavity length of 333 µm and a waveguide height of ~100 nm.

intensity measured by our InGaAs photodetector was calibrated using a commercial laser in order to correlate measured intensities to output powers. This particular device showed a maximum power output of ~1 mW before device failure. However, this is not typical for all Ge laser devices tested. Testing of other devices resulted in a maximum observed output of ~8 mW at 1680 nm before laser failure.

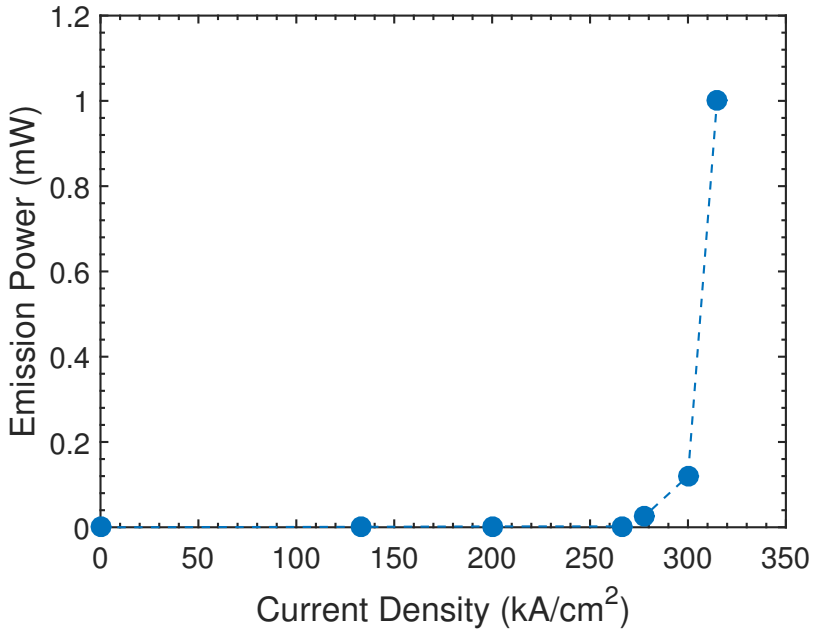

Figure 4-9: L-I curve showing lasing threshold for 270 µm long Ge laser device (λ = 1650 nm) injected at 1000 Hz with a 4 % duty cycle (40 µs pulse width).

Testing of many devices has resulted in observation of lasing from Ge over a large wavelength range of 1520 nm to 1700 nm. Figure 4-10 shows some of the various laser lines seen from samples with varying cavity lengths and Ge thicknesses. This wide range of observed lasing emission wavelengths is partially due to our inconsistent CMP processing which resulted in a samples with a variety of Ge thicknesses. For our devices, the cavity losses are highly dependent on the Ge thickness due to differences in the amount of optical mode confined to the Ge material. For thinner Ge waveguides, the mode is less confined to the Ge and losses from absorption in the cladding and contacts increases. Therefore, the thinner Ge waveguides require more injection in order to overcome cavity losses increasing the threshold current. Under lasing conditions, the optical gain is clamped to the value of the cavity losses and emission occurs where gain is maximum. For our Ge devices, the wavelength which corresponds to maximum gain varies with injection level as modeled by collaborators Sun et al. [79] and Cai et al. [86]. Figure 4-11 shows how gain clamping results in the observed varying laser emission across the Ge gain bandwidth for devices with varying thicknesses. A 100 nm thick device has a modal loss of ~1000 cm^{-1} meaning a relatively high carrier injection level is needed and lasing would be expected to occur at ~1520 nm. On the other hand, a 500 nm thick device only has a modal loss of ~90 cm^{-1} leading to a lower required injection level and emission at ~1600 nm. Moreover, observation of lasing at 1520 nm indicates that we have achieved optical gain of >1000 cm^{-1} in our Ge material.

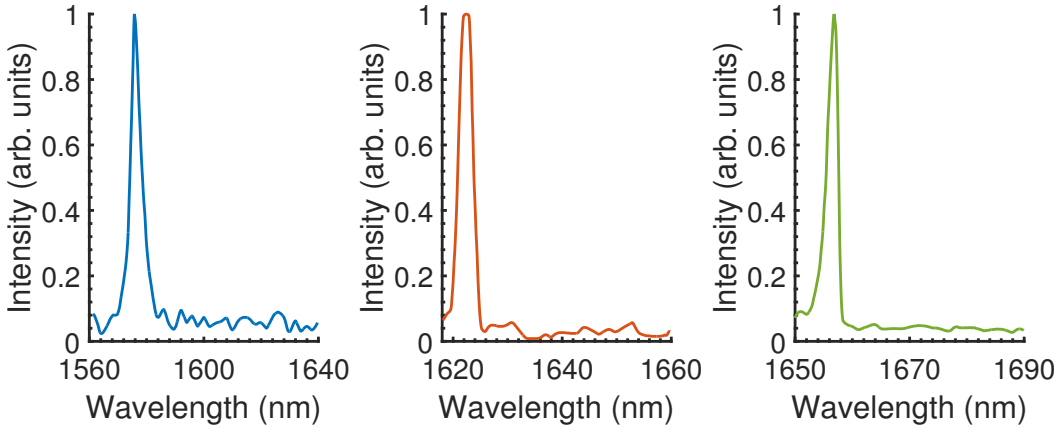

Figure 4-10: Emission spectra for various Ge laser devices showing lasing over a wide wavelength range at (a) 1579 nm, (b) 1622 nm, and (c) 1656 nm.

The observed large gain bandwidth was surprising because lasing past 1630 nm was not thought to be possible by initial models [79]. Subsequent models factoring in bandgap narrowing (BGN) of Ge at high n-type doping levels have since explained the observed large gain bandwidths [86]. A summary of specifications obtained from measurements of the first electrically pumped Ge lasers are contained in Table 4.1.

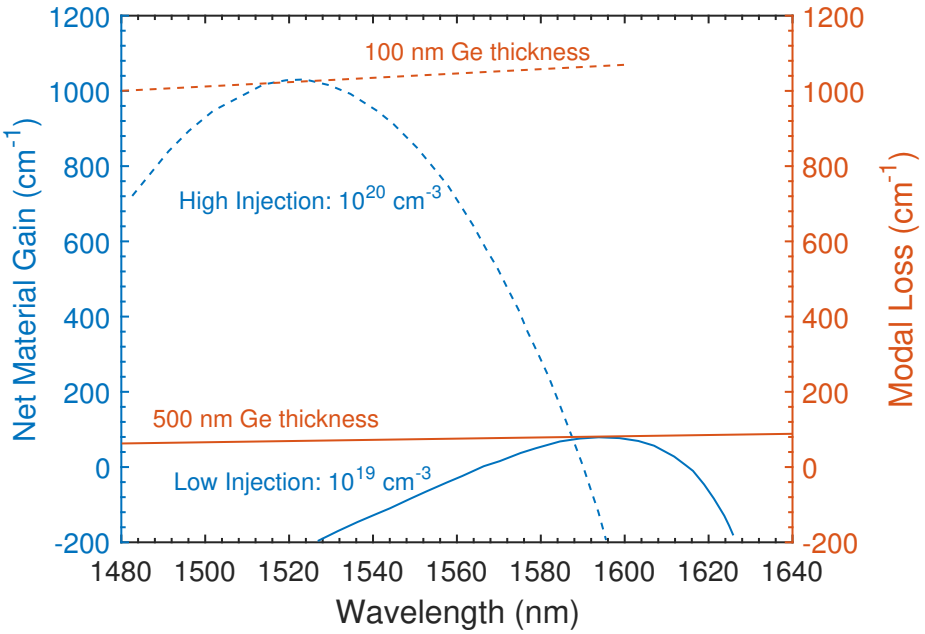

Figure 4-11: Simulation of gain clamping conditions for Ge Fabry-Pérot lasers showing how the lasing wavelength changes for varying Ge thicknesses due to different injection levels being required to overcome modal losses.

Table 4.1: Summary of Electrically Pumped Ge-on-Si Laser Specifications

Specification	Value
Doping Concentration	4.2×10^{19} cm^{-3}
Tensile Strain	0.2 %
Laser Linewidth	<1.2 nm
Gain Spectrum Bandwidth	~200 nm
Optical Gain	>1000 cm^{-1}
Max Output Power	~8 mW
Threshold Current Density	>280 kA cm^{-2}

4.4 Impact of Dislocations on Threshold Current

Our Ge laser devices show fairly high threshold currents compared to III-V laser diodes ($J_{th} \approx 1\,kA\,cm^{-2}$). Modeling has predicted that threshold currents as low as $0.53\,kA\,cm^{-2}$ (comparable to III-V lasers) should be achievable from a double heterojunction Ge laser [86].

A potential source of increased threshold current is non-radiative recombination due to threading dislocations within our Ge laser material. While previous studies have obtained threading dislocation densities (TDD) of $\sim 1 \times 10^6\,cm^{-2}$ from selective two-step Ge growth via UHVCVD, the studies were conducted on intrinsic Ge grown without any *in situ* doping [77]. Because dopant out-diffusion was not a concern, a cyclic annealing process at higher temperatures and longer times was used. Laser devices only receive a quick anneal step in order to diffuse and activate dopants. A longer annealing step would drive dopants out of the active region and prohibit lasing due to insufficient gain during injection. Figure 4-12 shows a plan-view TEM of the Ge material in our devices after dopant drive-in showing an average TDD of $\sim 1.9 \times 10^9\,cm^{-2}$ [75]. Therefore, it is worthwhile to develop a model to determine the effect of threading dislocations on the threshold current for our Ge laser devices.

Threading dislocations primarily impact the device by increasing carrier recombination through a non-radiative trap-assisted/SRH process. For lasers, recombination of carriers that does not contribute to stimulated emission is undesired. This includes spontaneous emission which is not coupled into the lasing mode. Therefore, during lasing, the lifetime of carriers should ideally be as long as possible. Similar to Equation 2.10, we can describe the lifetime (τ) as containing contributions from radiative (spontaneous) and non-radiative processes

$$\frac{1}{\tau} = \frac{1}{\tau_{rad}} + \frac{1}{\tau_{nr}} \tag{4.2}$$

where τ_{rad} is the radiative lifetime and τ_{nr} is the non-radiative lifetime. For our pseudo-direct bandgap Ge, the direct transition radiative lifetime is $\sim 10\,ns$ [87]. If we assume that non-radiative recombination is dominated by dislocations, based on Equation 4.2, the impact of dislocations on the overall lifetime is negligible when $\tau_{nr} \gg 10\,ns$ and becomes significant when $\tau_{nr} \approx 10\,ns$.

We can estimate the non-radiative lifetime using an SRH model assuming that the dislocations primarily introduce mid-gap ($E_t = E_i$) states at charged kink sites [88]:

$$\tau_{nr} = \frac{1}{\sigma_p v_p N_{kink} N_{dis}} \tag{4.3}$$

where N_{kink} is the density of kink sites along a dislocation and N_{dis} is the dislocation density. A doping dependence on the number of kink sites is expected based on the doping dependence of dislocation velocity in highly doped Ge [89]. The experimental data for dislocation velocities in Ge have been fit by Y. Cai [75] to determine the following empirical relationship between the number of kink sites and dopant concentration:

$$N_{kink} = 2.5 \times 10^5 \left[1 + \left(\frac{n}{10^{18}} \right)^{0.63} \right]\ cm^{-1}. \tag{4.4}$$

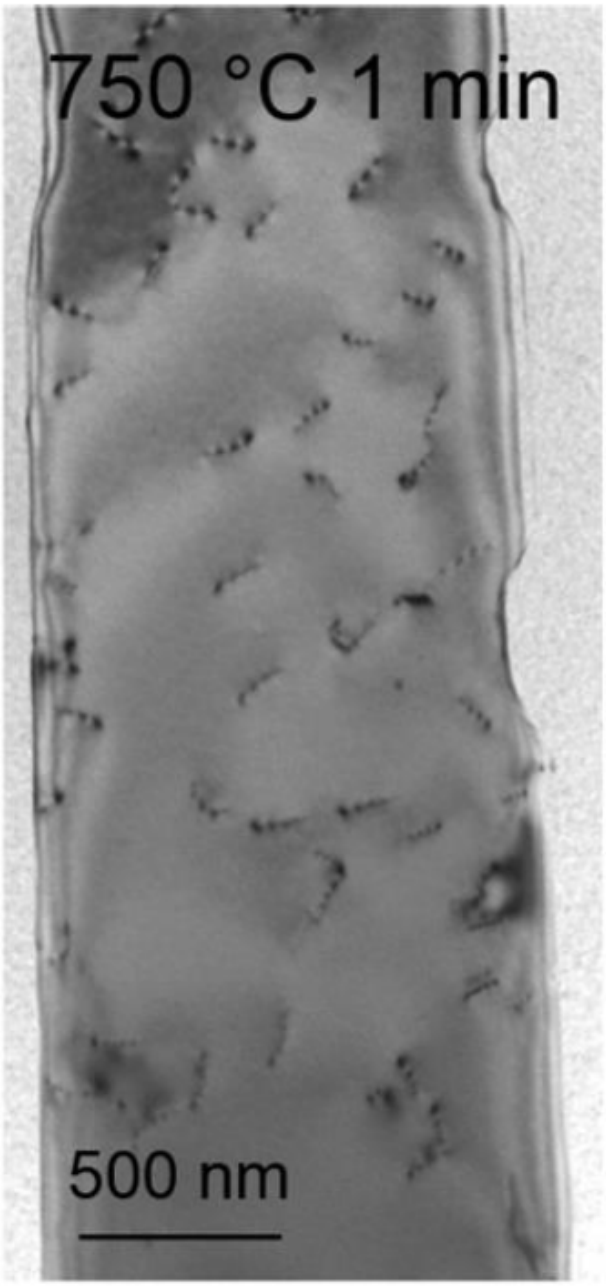

Figure 4-12: Plan-view TEM of the Ge material in laser devices after dopant drive-in thermal treatment of 750 °C for 1 min showing an average threading dislocation density of $\sim 1.9 \times 10^9$ cm^{-2}. *Courtesy of T. Milakovich [75]*

Therefore, for the observed TDD of $\sim 1.9 \times 10^9\,\mathrm{cm}^{-2}$, we estimate that the non-radiative lifetime is ~0.2 ns. This is calculated based on a device with an n-type dopant concentration of $4.5 \times 10^{19}\,\mathrm{cm}^{-3}$ where the thermal velocity of holes (v_p) is $1.9 \times 10^7\,\mathrm{cm\,s}^{-1}$ and the capture cross section for holes is assumed to be $4 \times 10^{-14}\,\mathrm{cm}^2$ at 300 K [88]. Because the estimated non-radiative lifetime is much smaller than the radiative lifetime, we can expect that the measured dislocation densities are sufficient to impact device performance.

We can also make a quantitative estimate of the increase in threshold current due to dislocation recombination. For a laser, the net carrier concentration is influenced by generation due to current injection and recombination due to radiative and non-radiative processes. Assuming uniform injection, the generation rate can be described by

$$G = \frac{\eta_\mathrm{inj} J}{q d} \tag{4.5}$$

where η_inj is the injection efficiency, J is the current density, q is the elementary charge constant, and d is the thickness of the active Ge region. Using the arguments from Section 2.1.1, we can describe the recombination rate in terms of the carrier lifetime

$$R = \frac{\Delta n}{\tau}. \tag{4.6}$$

At threshold, generation and recombination are in steady-state ($G = R$) allowing for calculation of the threshold current density (J_th) from

$$J_\mathrm{th} = \frac{q d \Delta n_\mathrm{th}}{\eta_\mathrm{i} \tau}. \tag{4.7}$$

where Δn_th is the injected carrier concentration when material gain surpasses losses leading to lasing. Using Equation 4.2, we can separate out of the magnitude of the threshold current density which is specifically related to non-radiative recombination by dislocations:

$$\Delta J_\mathrm{dis} = \frac{q d \Delta n_\mathrm{th}}{\eta_\mathrm{i} \tau_{nr}}. \tag{4.8}$$

Assuming no injection losses ($\eta_\mathrm{i} = 1$) and some common values for device parameters (d = 300 nm and $\Delta n_\mathrm{th} = 2 \times 10^{19}\,\mathrm{cm}^{-3}$) we estimate that the observed TDD of $\sim 1.9 \times 10^9\,\mathrm{cm}^{-2}$ increases the threshold current by $\sim 400\,\mathrm{kA\,cm}^{-2}$. This is in the range of experimentally observed threshold current densities indicating that dislocations account for a significant amount of the observed large threshold current densities (relative to theoretical lower limits close to $\sim 1\,\mathrm{kA\,cm}^{-2}$).

Figure 4-13 shows a plot of non-radiative lifetime and threshold current increase (ΔJ_dis) due to varying TDD. A red line is superimposed where $\tau_\mathrm{rad} \approx \tau_\mathrm{nr}$ showing that reducing the TDD to $\sim 4 \times 10^7\,\mathrm{cm}^{-2}$ would drastically reduce the impact of dislocations on the threshold current density ($\Delta J_\mathrm{dis} \approx 10\,\mathrm{kA\,cm}^{-2}$). Reducing the TDD another order of magnitude to $\sim 4 \times 10^6\,\mathrm{cm}^{-2}$ would further raise the non-radiative lifetime making the contribution of dislocations to threshold current density negligible ($\Delta J_\mathrm{dis} < 1\,\mathrm{kA\,cm}^{-2}$).

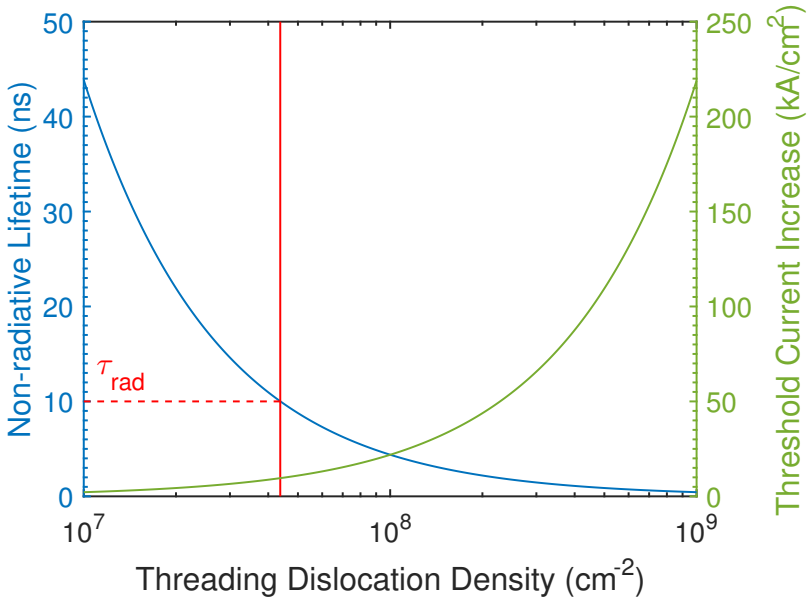

Figure 4-13: Estimation of non-radiative lifetimes and threshold current increases due to varying threading dislocation densities. Non-radiative lifetime is approximately equal to the radiative lifetime for a TDD of $\sim 4 \times 10^7$ cm^{-2}.

4.5 Future Work

We have successfully demonstrated electrically pumped lasing from Ge. Tested devices have fairly high threshold currents which we have determined to largely be a result of the high TDD in the active region. Further studies should focus on reducing the TDD in order to reduce the threshold current density and increase the output power. If failure is indeed related to the high threshold current, reducing TDD should also lead to increased reliability of Ge lasers which is crucial for these devices to ever be used in a commercial application. Furthermore, it is also possible that the recombination of carriers at dislocations is leading to enhanced defect reactions also contributing to device failure (Section 2.2.2).

Reducing the TDD will be challenging, but as previously mentioned, desired values ($\sim 4 \times 10^6$ cm^{-2} for negligible impact to threshold current density) have been achieved in lower doped Ge grown via two-step UHVCVD. Potentially, additional annealing processes could be developed which reduce the TDD before doping or delta doping of Ge.

In addition to reducing TDD, there are two obvious areas of improvement in our Ge laser devices:

1. Non-optimal cavity design. In our work, Fabry-Pérot cavities were used to simplify fabrication and testing. These structures were not completely optimized for reducing modal overlap with the heavily doped Si layers and metal contacts. Moreover, one of the mirrors was formed simply by cleaving of the samples. Better optimization of the laser structure should lead to greatly reduced modal losses and mirror losses.
2. Severe dishing of Ge due to poor CMP. As previously mentioned, CMP of the Ge after delta doping was not well controlled and lead to dishing of the Ge altering

the supported modes and possibly increasing carrier recombination at the surface. Subsequent CMP process optimization has lead to a Ge CMP procedure with much better uniformity and control [90].

These factors largely influence Δn_{th} meaning that they could also lead to further reductions in threshold current.

Chapter 5

Colloidal Quantum Dot Chalcogenide Glass Films

Integrated light sources are also a key component for enabling the fabrication of small-footprint, high sensitivity system-on-chip optical based chem-bio sensors. For optical sensing schemes, the optical path length determines the overall sensitivity and ideally should be as large as possible. However, for a tabletop spectrometer, this requires increasing the overall footprint of the system. Using microphotonic resonators on chip, the path length can be increased significantly while simultaneously reducing the overall footprint of the system through integration of components (e.g., sensing elements, photodetectors, and read-out circuitry). The drastic reduction in the size of sensor systems can enable novel applications where real-time constant monitoring is needed.

Excluding the light source, a variety of components required for fabrication of system-on-chip optical based chem-bio sensors have been fabricated for silicon and chalcogenide glass platforms [5]. Optical resonator sensors can operate in two modes of sensing, each based on observing changes in a different component of the complex refractive index (Figure 5-1). Cavity-enhanced absorption spectroscopy (absorption sensing), relies on measurement of extinction ratio changes in a resonant peak due to optical absorption by the analyte [91]. Chemicals can be identified by their "fingerprint" in the mid-IR due to absorption by molecular vibrational modes. Refractive index spectoscopy (index sensing) instead correlates a shift in resonant peak wavelength to a change in effective index resulting from the presence of the analyte being sensed [92, 93]. In this sensing mode, the signal is often increased through the use of a functional layer which reacts with the analyte creating a larger shift in the effective index than would been seen by the presence of the analyte alone. The choice of source wavelength is less restrictive than for cavity-enhanced absorption spectroscopy.

In this chapter, we investigate the optical properties and morphology of thin films containing colloidal quantum dots incorporated into a chalcogenide glass matrix. Unlike

The work in this chapter was done in collaboration with Prof. Moungi Bawendi's group at MIT (synthesis and preparation of quantum dots) and Prof. Kathleen Richardson's group formerly at Clemson University now at University of Central Florida (synthesis of bulk chalcogenide glasses) with mentorship from Prof. Clara Dimas at Masdar Institute of Science and Techonology.

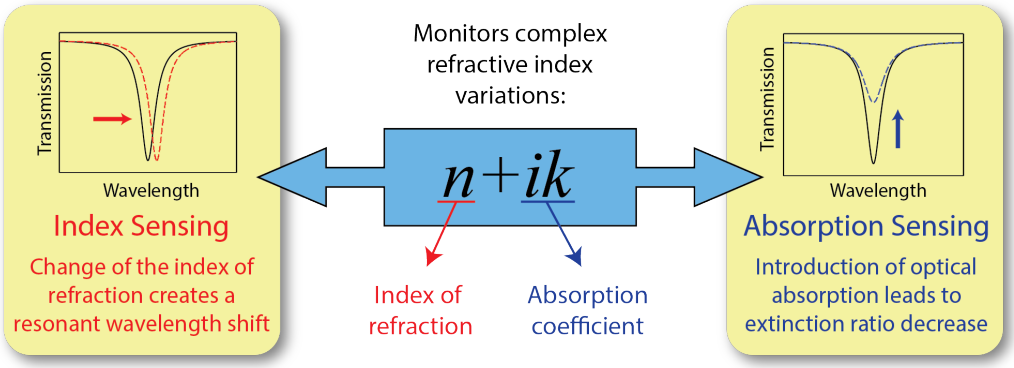

Figure 5-1: Schematic illustrating the two methods of resonant optical sensing based on observing changes in the complex refractive index.

the previous work on developing a Ge-on-Si laser, this system does not require a crystalline substrate and can be integrated onto any substrate and into a wider variety of potential applications. The overall aim of this work is to provide a platform for the fabrication of low-cost light sources which can be integrated with a chalcogenide glass photonics platform for optical sensing applications (Figure 5-2).

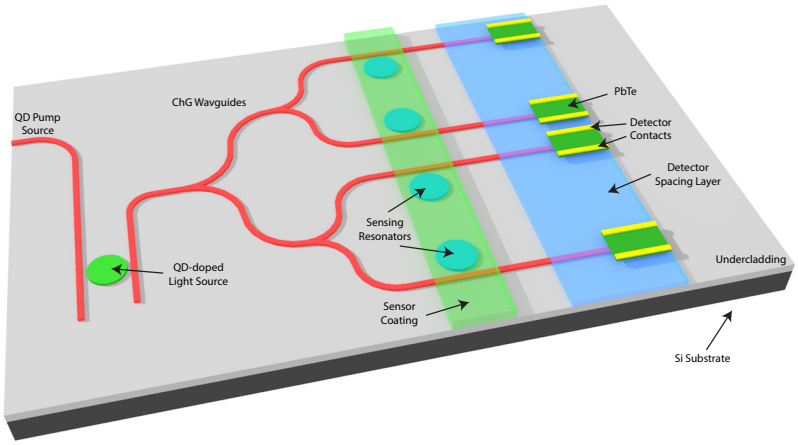

Figure 5-2: Schematic representation of a QD-doped ChG light source integrated with an optical sensor system built on a ChG platform.

5.1 Background

5.1.1 Quantum Dots

Semiconductor light sources based on nanostructures provide greater electronic confinement which leads to unique optoelectronic properties such as improved temperature stability

and greater emission wavelength tunability. Quantum effects become significant when the size of a semiconductor material approaches the exciton Bohr radius (the distance between an electron-hole pair) [94]:

$$a_{\mathrm{B}} = \frac{\hbar^2 \varepsilon}{\mu q^2} \tag{5.1}$$

where ε is the dielectric constant of the semiconductor and μ is the exciton reduced mass. For materials confined in all three spatial dimensions, such as in quantum dots, energy levels are quantized with values directly related to the size and composition of QDs. By approximating a quantum dot as a spherical particle in a potential well with a minor Coulombic correction, the effective band edge as a function of particle size can be described by

$$E_{\mathrm{eff}}(a) \approx E_{\mathrm{g}} + \frac{\hbar^2 \pi^2}{2a^2}\left(\frac{1}{m_{\mathrm{e}}^*} + \frac{1}{m_{\mathrm{h}}^*}\right) - \frac{1.8q^2}{\varepsilon a}\ \mathrm{eV} \tag{5.2}$$

where E_{g} is the bandgap of the bulk material and m_{e}^* and m_{h}^* are the electron and hole effective masses [94]. Therefore, the absorption and emission spectra for a particular material system can be tuned by varying quantum dot size. There are two primary methods for fabrication of quantum dots. Quantum dots can be epitaxially grown in certain situations through MBE (molecular beam epitaxy) and CVD (chemical vapor deposition) processes by growth of materials onto substrates which are not lattice matched. Islands of the deposited material can spontaneously form in order to relive strain forming quantum dots. Epitaxially grown QDs have been used to fabricate optoelectronic devices such as lasers and photodetectors [95–97]. However, epitaxial growth involves high-temperature and high-cost processing which are often not compatible with a CMOS platform. Controlled positioning of quantum dots during growth is also a challenge.

The other fabrication method is the low-cost synthesis of colloidal quantum dots through a solution based organometallic route [98, 99]. These methods involve the combination of precursor reagents into a solvent containing surfactants or ligands. These ligands bind to the surface of the quantum dots as they nucleate and grow making the quantum dots soluble in the solvent. Quantum dot sizes are controlled by careful selection of solution temperature and ligand chemistry. In addition to low-cost synthesis, colloidal quantum dots can be deposited by low-temperature and low-cost methods such as drop casting, spin coating, contact printing, and inkjet printing which are back-end CMOS-compatible.

Even though colloidal quantum dots are fabricated in a relatively "dirty" process (compared to the ultrahigh vacuum environments required for MBE and CVD) they can be considered nearly defect-free in the bulk. Moreover, DFT calculations predict that QDs are inherently tolerant of intrinsic defects [100]. However, QDs have a large surface to volume ratio which significantly increases the likelihood of carriers interacting with the QD surface. If the surface is not well passivated, it can introduce defect states which facilitate non-radiative recombination of excited carriers. For this reason, QDs for light emission applications are commonly over-coated (also via solution-based processing) with a wider bandgap material [101] to form a shell over the core narrow bandgap material. Well chosen shell materials provide much better passivation of surface states than the organic ligands which passivate the surface during fabrication. In addition, carriers are confined to the core

providing shielding from the potentially weaker passivation at the outer shell surface.

Using various materials systems, colloidal quantum dots have be fabricated which emit from ultraviolet [102] to mid-IR regimes [103, 104]. Previous studies have shown demonstration of lasing from colloidal quantum dots coupled to microspheres [105, 106] and microcapillary tubes [107, 108]. However, these device designs are not suitable for integration with other components hindering their application in photonic circuit applications. In this work we will focus on infrared sources for the reasons outlined earlier with the overall goal of developing a light source which can be integrated with other photonic components. Studies of IR emitters show that a strong quantum confinement regime can be achieved by narrow-bandgap IV–VI QDs (e.g., PbS and PbSe) due to large electron, hole, and exciton Bohr radii in IV–VI semiconductors compared with II–VI or III–V materials [109, 110]. Although mid-IR emission out to 4.1 µm has been shown for PbSe quantum dots, the quantum yields are significantly reduced from near-unity for near-IR quantum dots to $\lesssim$10 % for mid-IR emitting PbSe quantum dots [103]. The synthesis of well passivated mid-infrared quantum dots is still an outstanding problem. In this work, we use PbS quantum dots overcoated with CdS shells (Figure 5-3) which emit efficiently in the near-IR in order to reduce any possible issues related to poor quantum yields. However, our goal is to develop a platform for making light sources through incorporation of quantum dots into chalcogenide glasses and is largely independent of the specific quantum dot material used. This work can potentially be replicated with other quantum dot systems to produce light sources which emit from the UV to the mid-IR regimes.

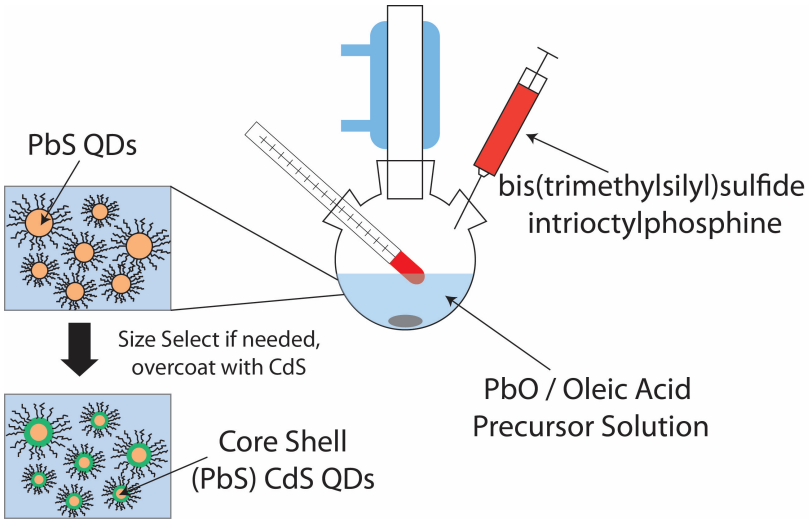

Figure 5-3: Schematic of PbS colloidal quantum dot synthesis through hot injection. Bis(trimethylsilyl)sulfide intrioctylphosphine is quickly injected into a carefully temperature controlled precursor solution containing PbO and oleic acid. The PbO reduces and reacts to nucleate PbS QDs whose growth quickly self terminates through passivation of the QDs by oleic acid ligands. Further materials can be added to the solution after QD nucleation to grow semiconductor shells to tailor electronic properties and provide extra surface passivation.

5.1.2 Chalcogenide Glasses

Chalcogenide glasses (ChGs) are amorphous compounds composed of metals and non-metals bonded with chalcogen elements (sulfur, selenium, and tellurium). Due to their phase change properties, ChGs have been used in non-volatile memory applications for a number of years [111, 112]. More recently, ChGs have found applications in microphotonic systems due to a number of desirable optical properties. ChGs have a wide optical transparency window encompassing visible to far infrared regimes [113]. This makes them a promising material for chemical sensing applications because many of the vibration absorption lines for molecules lie in the mid-infrared [5] where silicon-on-insulator (SOI) systems are lossy [114]. The index of refraction for ChGs can be tuned by variation of element choice and composition. In addition, the index of refraction is relatively high ($n \approx 2$–3) allowing for greater confinement in photonic circuit elements. This has the benefit of reducing the overall footprint of ChG photonic circuits. The wide tunablility of ChGs also allows for index contrasts as high as $\Delta n > 1$ from a single ChG alloy system. Previous studies have already shown potential for ChG photonics by successful demonstration of low loss waveguides and high quality factor (high-Q) resonator cavities using ChG materials [115–117].

One of the greatest advantages to using a ChG platform for photonics applications is that their amoprhous nature allows for low temperature deposition of thin films on most substrates regardless of substrate lattice constant. This facilitates easy integration of ChG components with other photonic components and materials platforms (including being Si CMOS-backend compatible). ChGs can be deposited by a number of different deposition techniques including thermal evaporation, chemical vapor deposition (CVD), pulsed laser deposition (PLD), and RF magnetron sputtering. Our collaborators at Clemson University have developed an alternative method where bulk ChGs are dissolved and deposited through solution based techniques such as drop casting and spin coating [118]. We have primarily focused on using two ChG compositions which can be solution-processed: As_2S_3 and $Ge_{23}Sb_7S_{70}$. The experiments carried out in this section have been performed using both ChG compositions.

The general procedure for deposition of ChG thin films by spin coating used in this work is as follows:

1. Bulk ChGs are prepared by our collaborators at Clemson University using a traditional melt-quench technique starting with high purity elemental constituents. Materials are vacuum sealed inside quartz ampoules and heated to several hundred degrees Celsius for several hours in a rocking furnace. The ampoule is air-quenched and subsequently annealed at sub glass transition (T_g) temperatures.
2. In order to accelerate the dissolution process, mortar and pestle are used to crush the bulk glass into particles ~1 mm in diameter.
3. Crushed glass is added to the solvent in a small vial with a stir bar. The vial is sealed to prevent solvent evaporation and the mixture is stirred for ~2 days in order to completely dissolve the ChG. Because dissolution is altered by the presence of moisture, solution processing of ChGs is carried out inside a glovebox where H_2O and O_2 are removed by circulation of the inert N_2 atmosphere over a copper catalyst bed.
4. Solutions are filtered through a 0.1 µm syringe filter and spun onto substrates with

spin speeds and times determined by the ChG composition and desired thickness.
5. Samples are soft baked at 95 °C for 5 min while still in glove box.
6. Samples are then hard baked at 180 °C ($Ge_{23}Sb_7S_{70}$) or 150 °C (As_2S_3) for 2 hrs in a vacuum oven.

As_2S_3 and $Ge_{23}Sb_7S_{70}$ are readily dissolved by several amine-based solvents with some slight differences as compared in Table 5.1. Each solvent has a different maximum concentration of ChG which can be dissolved before precipitates form resulting in off-stoichiometric thin films. Ethanolamine (ETA) is the least sensitive to moisture and thus the easiest solution to prepare. However, the viscosity of ETA solutions is relatively high making fabrication of thinner (<1 μm) films difficult. For thinner films, propylamine (PA) is a good alternative. PA evaporates quickly so films must be prepared and spun quickly (<5 s total time) to ensure film uniformity.

Table 5.1: Comparison of solvents for ChG solution processing

Solvent	$[Ge_{23}Sb_7S_{70}]$ ($mg\,mL^{-1}$)	$[As_2S_3]$ ($mg\,mL^{-1}$)	Viscosity	Sensitivity to Moisture
Propylamine (PA)	25	50	Low	Medium
Ethylenediamine (EDA)	50	100	Medium	High
Ethanolamine (ETA)	100	200	High	Low

5.2 Dissolution of QDs and ChGs in a Common Solvent

Incorporation of quantum dots into a matrix is desired for increased mechanical and chemical stability as well as providing a platform for device fabrication. A key requirement for the matrix is that it should provide good passivation of the QD surface in order to maintain the luminescence properties colloidal QDs possess in solution. Previous studies have shown that some polymers, including polymethyl methacrylate (PMMA), can provide adequate surface passivation thereby maintaining high QD emission quantum yields for luminescence applications [119]. However, the low index of refraction of most polymers ($n \approx 1.5$) makes fabrication of optically confining structures difficult. In addition, PMMA has a more limited transparency window limiting QD/PMMA composites from mid-infrared applications.

Previous attempts to incorporate QDs into glass matrices have largely focused on two approaches. In the first approach, a glass melt contains constituents in concentrations above the room temperature solubility limit so that QDs with nucleate upon quenching. This approach leads to the production of well passivated QD-doped bulk materials but is not easily adapted to on-chip device fabrication. Bulk glasses formed this way have been used as sputtering targets for thin film fabrication, but the sputtering process induces defects which lead to poor film morphology and luminescence. The second approach involves use

of sol-gel processing techniques to embed QDs into oxide glasses. This approach may be useful for some applications, but the wider transparency window and higher indices of refraction make ChGs a more desirable matrix for QDs.

Our first approach for incorporation of QDs into ChGs was to look for a solvent in which both our QDs and ChGs could be dissolved. Once mixed together in a common solvent, we can spin coat the solution and bake to form a QD-doped ChG thin film. PbS QDs are typically dissolved in chlorobenzene after fabrication but can be "crashed out" of the solvent using a centrifuge and redissolved in other solvents. PbS QDs capped with oleic acid ligands were mixed in ~5 wt% with all three solvents used in Section 5.1.2 to prepare ChG solutions. Dissolution of QDs in EDA resulted in a brown, cloudy mixture with sediment at the bottom indicating that QDs were not well dispersed in the solvent. QDs also did not dissolve well in ETA and floated on top of the solvent. However, mixtures of QDs in PA formed dark but clear solutions indicating that PA was a good solvent for both QDs and ChGs. In parallel, we also attempted to dissolve ChGs in butylamine (BA) which is a common solvent for oleic acid capped QDs. Despite its chemical similarity to PA, EDA, and ETA, we were unable to completely dissolve As_2S_3 or $Ge_{23}Sb_7S_{70}$ in BA. A summary of these experiments is contained in Table 5.2.

Table 5.2: Comparison of ChG and QD solubility in amines

	Propylamine (PA)	Ethylenediamine (EDA)	Ethanolamine (ETA)	Butylamine (BA)
ChGs	Good	Good	Good	Bad
QDs	Good	Bad	Bad	Good

Based on the observations that PA was the only solvent in which both ChGs and QDs were soluable, we attempted to dissolve both species into a PA solution. Solutions were prepared by two processes:

1. Separately prepare well dissolved solutions of ChGs in PA and QDs in PA and mix them together.
2. "Crash" QDs out of solution and add them to a solution of ChGs dissolved in PA.

Both processes resulted in the immediate and visibly noticeable segregation of QDs within the ChG/PA solution. Reducing QD and ChG concentrations by a factor of 2 showed no change in behavior. Optical micrographs of films fabricated from spin coating solutions of As_2S_3 with and without PbS QDs are shown in Figure 5-4. The films containing no QDs are smooth and uniform whereas the films fabricated from solutions containing QDs have dark inclusions as large as ~20 µm in diameter which are assumed to be aggregates of PbS QDs within the ChG matrix.

In order to characterize the luminescence properties of QD-doped ChG films, we measured photoluminescence (PL) from films after excitation by visible light. For comparison, we also obtained photoluminescence spectra for QDs (from the same fabrication batch) embedded in PMMA which, as previously mentioned, provides good passivation of QDs. Figure 5-5 shows a comparison of the spectra obtained from QDs embedded in ChG and

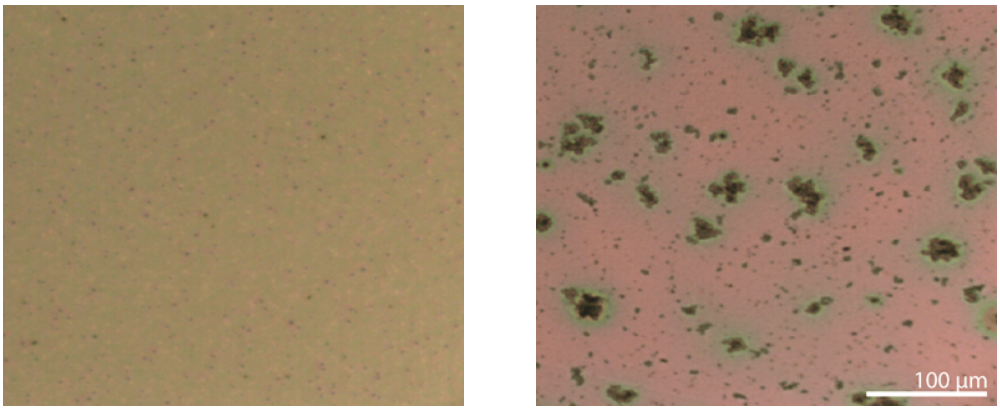

(a) (b)

Figure 5-4: Optical micrographs of thin films fabricated from solutions of As_2S_3 in PA (a) without and (b) with PbS QDs

PMMA matrices. While it is difficult to quantitatively compare the intensities of the two spectra due to uncorrected variations in surface reflections and roughness, the measurements were obtained using the same excitation intensity, monochromator slit width, and photodetector integration times. Therefore, it is promising that the PL intensity from the QDs embedded in ChGs is of the same order of magnitude as the PL intensity from the QDs embedded in PMMA. This result is a bit surprising since, for luminescent applications, aggregation of QDs is avoided due to the increased likelihood of electron-hole pair quenching at a non-radiative recombination centers (due to defects) as carriers transfer across adjacent QDs from higher energy states (smaller diameter QDs) to lower energy states (larger diameter QDs). While shells help to reduce recombination of carriers at surfaces, the efficiency of core/shell QDs drops from close to unity in solution to only 10 % to 20 % in close-packed films [101].

The PL spectra in Figure 5-5 were obtained using a excitation laser whose spot size was ~1 mm in diameter. Therefore, the spectra obtained represent the overall emission from areas of the film with and without aggregates. It is uncertain whether or not aggregates are completely quenched (reducing quantum yield of the film) or are still contributing to emission. A wide size distribution of QD aggregates is observed in Figure 5-4b leading to the possibility that not all QDs formed into aggregates and that the film luminescence is due to non-aggregated regions. Information about the luminescence from individual aggregates can be obtained through the use of micro-PL measurements. In micro-PL, the emission laser is focused to a spot size ~10 µm in diameter thereby allowing separate PL measurement of areas with and without aggregates as seen in Figure 5-6. Note that the peak emission wavelength has changed due to the use of a different batch of QDs (with a different center wavelength) when fabricating new samples for micro-PL measurements. The lack of signal from areas without aggregates most likely indicates that all of the QDs added to the ChG solution have clustered into aggregates. If there are any isolated QDs left in the film, they are present in concentrations too low to be measured by our PL setup. On the other hand, we see clear signal when directly exciting aggregates indicating that

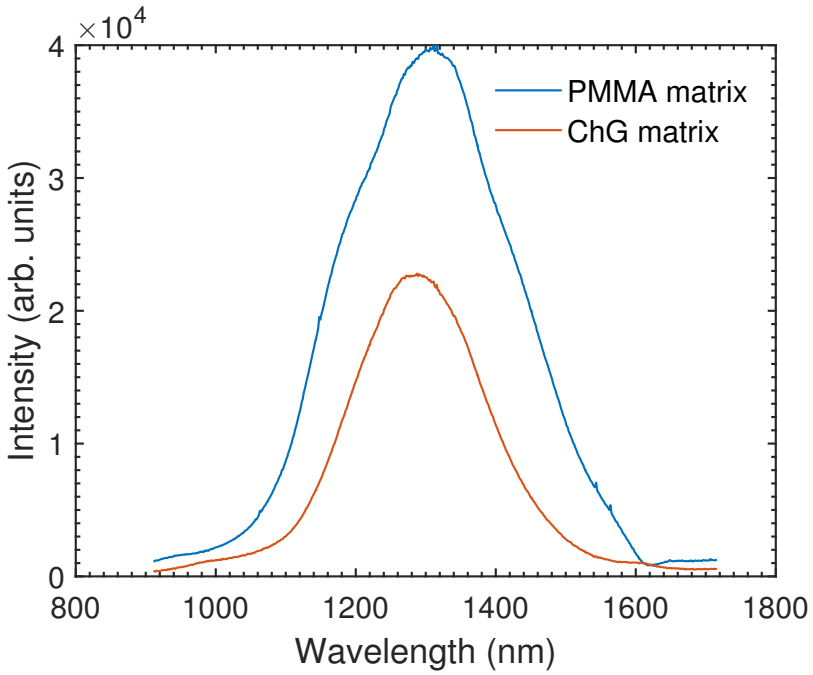

Figure 5-5: Photoluminescence spectra comparing PbS QDs ($\lambda_c \approx 1300$ nm) embedded in PMMA and ChG ($Ge_{23}Sb_7S_{70}$) matrices. Samples were excited by a CW 633 nm laser.

the formation of aggregates has not completely quenched luminescence. The observed luminescence from aggregates also helps explain how comparable PL intensities were seen from aggregated QD-ChG films as were seen from QD-PMMA films (Figure 5-5).

By dissolving ChGs and QDs in a common solvent, we have shown the first demonstration of luminescence from colloidal QDs embedded in a ChG matrix. The observation of luminescence indicates that ChG matrices can provide suitable passivation for QD surfaces making QD-doped ChGs a suitable materials platform for building on-chip light sources.

5.3 Inorganic Ligand Exchange

While aggregated films fabricated from dissolution of QDs and ChGs in a common solvent show luminescence, aggregated films do not have an ideal structure for building integrated light sources. Devices fabricated out of these films could suffer high losses from scattering due to the large index of refraction difference between the PbS aggregates and the surrounding matrix. In addition, photonic device dimensions are typically on the same order as those of the aggregates meaning control of aggregate placement would be necessary. It would be highly desirable to develop films of QDs homogeneously distributed in a ChG matrix.

Aggregation is likely due to the interaction between the ChG species in solution the oleic acid ligands which cap and passivate the surface of the QDs. A possible route to preventing QD aggregation in solution is to find a more suitable capping agent for the QDs. Methods have been developed for the passivation of QDs surfaces with completely inorganic metal

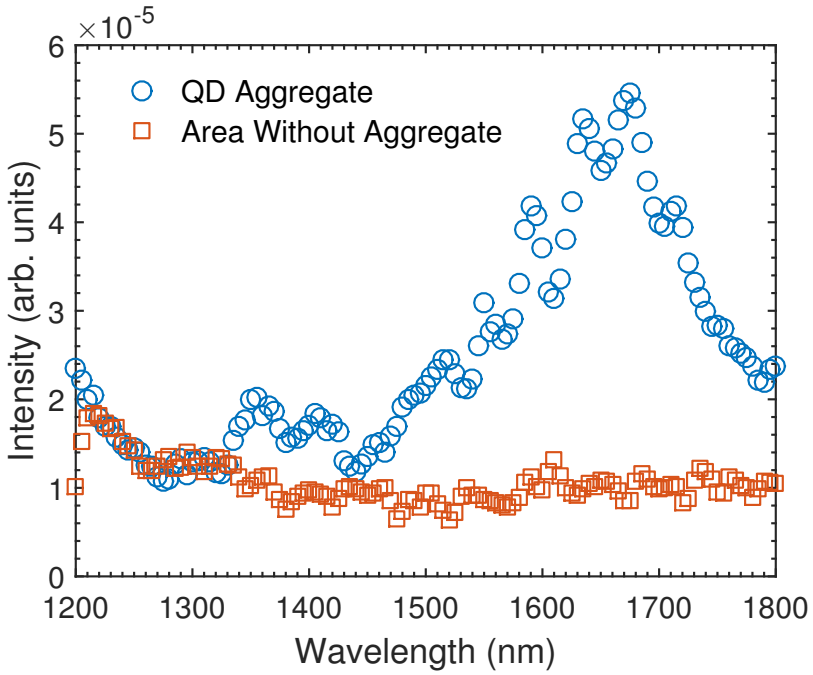

Figure 5-6: Micro-PL spectra comparing emission from areas containing QD aggregates to areas without QD aggregates in films of PbS QDs ($\lambda_c \approx 1650\,\text{nm}$) embedded in As_2S_3.

chalcogenide complexes (MCC) for the fabrication of highly conductive close-packed QD composite films [120]. We expect to see greater stability of QDs in ChG solutions due to the chemical similarity between MCC ligands and ChGs. In addition, the use of MCC ligands avoids the need for organic molecules which would reduce significant losses if the system is scaled to the mid-infrared.

The procedures outlined in [121] were followed to replace the oleic acid ligands on PbS QDs with AsS_3^{3-}. We then repeated the procedures from the previous section to fabricated QD-doped ChG films. Upon mixture of AsS_3^{3-} capped QDs and As_2S_3/PA solutions, no immediate aggregation was noticeable. When inspecting the solution after ~1 day, sediment was observed on the bottom of the vial indicating some aggregation had occured. Optical micrographs showing films fabricated from solutions made using AsS_3^{3-} ligands are shown in Figure 5-7. The homogeneity of this film is much better than films fabricated using QDs with oleic acid ligands; furthermore, the surface of the film has an appearance similar to that of undoped ChG films. Figure 5-8 shows micro-PL spectra from films of AsS_3^{3-} capped QDs in As_2S_3 to QDs from the same batch with oleic acid ligands (QD solution was drop casted onto Si substrates). The spectra are roughly identical showing that the ligand exchange process has not altered the emission spectra and that AsS_3^{3-} provides suitable passivation for luminescence.

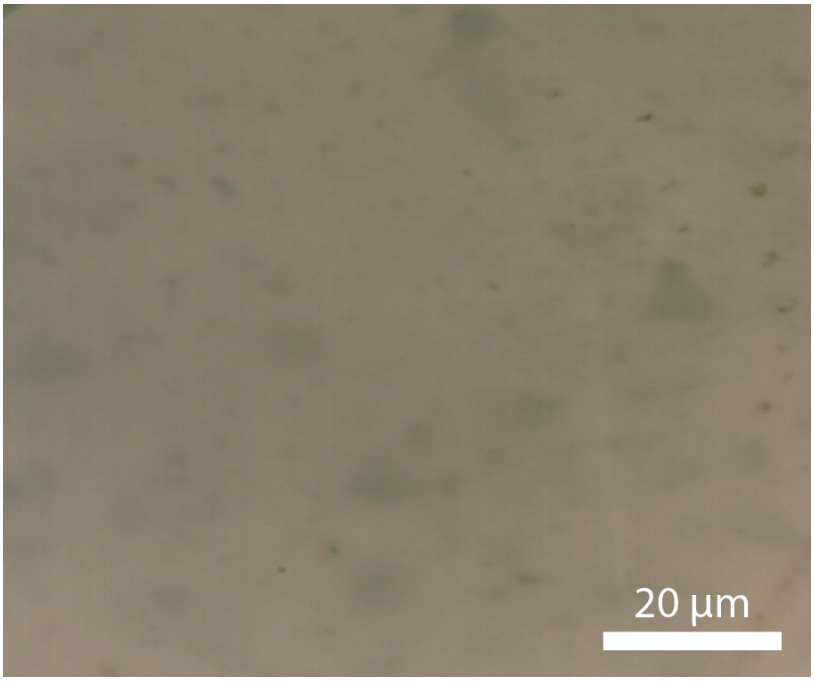

Figure 5-7: Optical micrograph of a thin film fabricated from AsS_3^{3-} capped QDs embedded in As_2S_3.

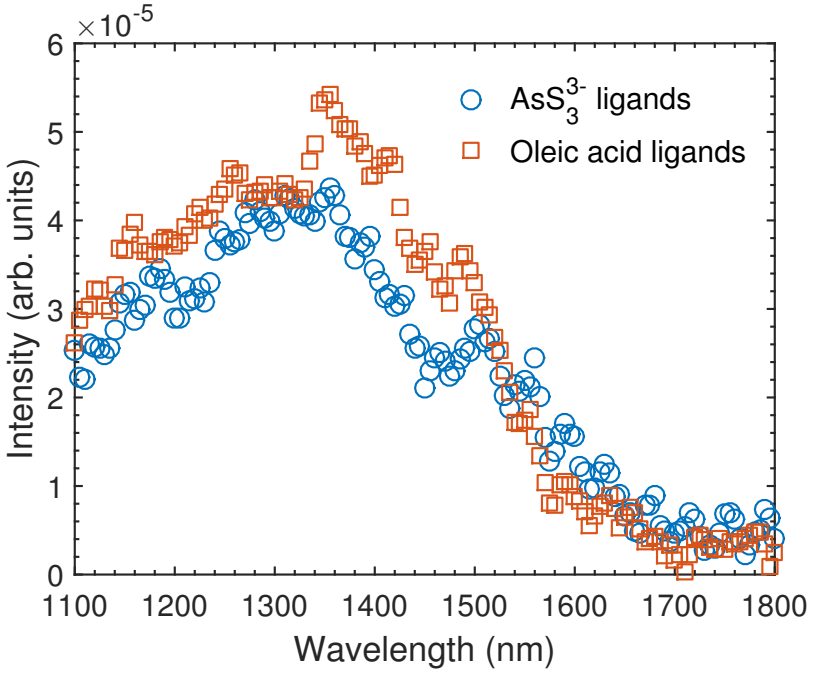

Figure 5-8: Micro PL spectra comparing emission from QDs with AsS_3^{3-} ligands embedded in As_2S_3 vs drop casted solutions of QDs with oleic acid ligands.

5.4 Future Work

We have demonstrated the feasibility of incorporating colloidal QDs into ChGs for light source applications. ChGs are able to provide a mechanically robust, high index of refraction matrix while adequately passivating the surface retaining the luminescent properties of QDs. We have identified a pathway towards obtaining films with homogeneously distributed QDs using mixing QDs with $AsS_3{}^{3-}$ ligands into solutions of ChGs dissolved in PA. While an inorganic ligand approach has yielded homogeneous films that are suitable for device fabrication, we have observed some issues preventing its adoption for immediate use in device fabrication:

1. Successful fabrication of uniform films is a low yield process. This is possibly due to the process being very sensitive to the environment in which QDs are mixed with ChGs. However, even when conditions are kept as similar as possible in a glovebox which has low O_2 and H_2O concentrations, ~50 % of the time, $AsS_3{}^{3-}$ capped QDs will aggregate when mixed with ChG solutions.
2. Solutions must be fabricated into films immediately. QDs are homogeneously distributed immediately after mixing of $AsS_3{}^{3-}$ capped QDs with ChGs but will start to aggregate soon after. Films fabricated from solutions made ~1 day previously, showed aggregates as large as ~40 µm in diameter. These films also showed significant red-shifting of emission spectra indicating that $AsS_3{}^{3-}$ ligands allow easier (relative to oleic acid) transfer of carriers from small QDs to large QDs. We expect that this red shift would also be accompanied by a reduction in quantum yield but have not attempted to experimentally verify that.
3. Even with films fabricated quickly after adding QDs to ChG solutions, stability is an issue. We have observed a significant drop off of luminescence of films over time and typically cannot measure any emission after ~1 month.

The mechanism behind the observed instability and quenching is unknown at this time. It is possible that the ChG matrix or remnant solvent in the matrix is reacting with the inorganic ligands stripping them from the QDs. Another possibility is that the ligand exchange process is incomplete and leaves unpassivated sites on the shell surface which can be attacked by the matrix or solvent in the matrix. If $AsS_3{}^{3-}$ capped QDs in ChGs are to be used in practical devices, the mechanism behind quenching will need to be understood and mitigated.

Chapter 6

Triplet Energy Transfer To Silicon

The impact on global climate change due to CO_2 emissions from energy generation via the burning of fossil fuels has created strong motivation for moving to alternative energy sources [122]. Solar power holds promise for providing a large amount of clean and sustainable energy. However, in 2014, solar power only accounted for 0.8 % (United States) and 1.0 % (global) of all electricity generated [123]. High cost relative to other energy sources is a large reason for poor adoption to date. In 2011, the U.S. Department of Energy launched the SunShot initiative to reduce the cost of solar energy 75 % by 2020 which is predicted to increase solar market penetration to 14 % by 2030 and 27 % by 2050 greatly reducing CO_2 emissions by the electric-sector [124]. Currently, 91 % of the energy generated by solar cells are based on silicon materials (either single crystalline or multi-crystalline) [123].

Silicon solar cell efficiency improvements can help play a role in reducing solar cell costs and reaching those goals. Shockley and Queisser used a detailed balance calculation to determine that Si single junction solar cells are limited to theoretical max efficiency of ~32 % which is very close to the maximum for any single junction solar cell [125]. Currently, the best single junction silicon solar cells (non-concentrated) have efficiencies of ~25 % [126] with the difference largely being a result of recombination processes not accounted for in the original detailed balance model [127]. The two largest loss mechanisms are (1) non-absorption of photons with energies below the bandgap and (2) thermalization of carriers to the band edges after absorption by photons with energies above the bandgap. Figure 6-1 shows a plot of the solar spectrum with the amount of power lost to these components for a silicon solar cell. The fraction of the total power for a particular wavelength lost to thermalization is superimposed to illustrate that for blue and green light, over 50 % of the power is lost to thermalization.

One way to increase efficiencies by reducing thermalization losses is to build a multi-junction solar cell which contains multiple semiconductors, each with a different bandgap. The solar cell is structured so that each semiconductor absorbs the portion of the solar spectrum where it is most efficient at power extraction. Multijunction solar cells have been fabricated which show overall efficiencies >40 % [126]. However, due to difficulty of fabrication, multijunction solar cells are very expensive and are primarily used in niche applications where efficiency is valued above cost (e.g., satellites in space).

The experimental work in this chapter was done in collaboration with Prof. Marc Baldo's group at MIT.

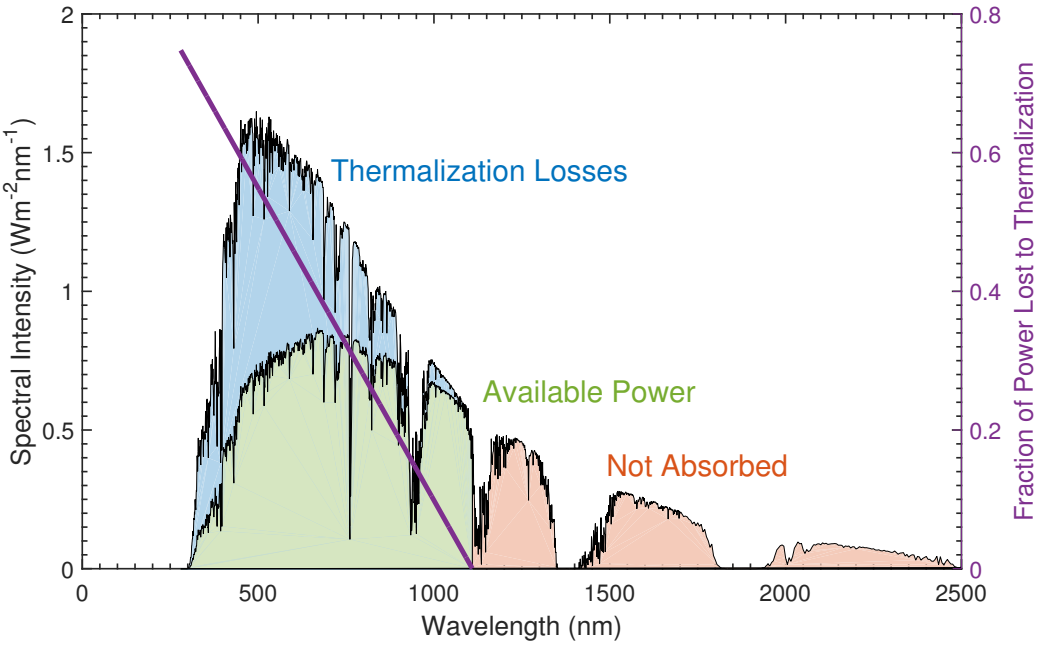

Figure 6-1: Theoretical solar spectrum losses for a single junction Si solar cell.

Another potential way to reduce thermalization losses is through the use of downconversion process to generate two electron-hole pairs with energies above the Si bandgap ($E > E_g$) from high energy photons whose energies are at least twice as large as the Si bandgap ($h\nu > 2E_g$). If these carriers can be transfered to silicon, the photocurrent output from high energy photons can be doubled. This work is focused on assessing the feasibility of reducing the thermalization losses (thereby increasing efficiencies) by combining conventional silicon solar cells with an organic semiconductor which undergoes singlet fission to generate two triplet excitons after absorption of one high energy photon. Emphasis will be placed on understanding the importance of the quality of the interface between the organic and inorganic semiconductor materials.

6.1 Background

6.1.1 Excitons in Organic Semiconductors

Excitons are bound electron-hole pairs which are attracted by Coulombic forces [128, 129]. In inorganic semiconductors, the dielectric constant is relatively large screening the attraction between electrons and holes resulting in binding energies on the order of ~0.01 eV (Wannier excitons). Therefore, except at very low temperatures, the charges can easily separate. Organic molecules, however, have lower dielectric constants leading to exciton binding energies of ~0.5 eV (Frenkel excitons), which is much greater than kT at room temperature and excitons in these materials are treated as quasiparticles. Like atoms in a conventional semiconductor, organic molecules can be arranged into crystalline solids. However, the molecules within the solid are weakly bound by Van der Waals bonds. Therefore, excitons

in organic semiconductors are often localized to single (or a few at most) molecules.

The energy levels of organic molecular models are best described by molecular orbital theory where molecules form a set of complex molecular orbitals which are filled by electrons according to the Pauli exclusion principle. Let's consider the creation of an exciton by excitation of an electron from the highest occupied molecular orbital (HOMO) to the lowest unoccupied molecular orbital (LUMO). An important feature of this two level system containing two electrons is the total spin. In the lowest energy state, both electrons occupy the HOMO and since they are fermions they cannot have the same spin. One has spin $s = +\frac{1}{2}$ (represented by $\uparrow$) and the other has spin $s = -\frac{1}{2}$ (represented by $\downarrow$) and the total spin is zero ($s_{\text{tot}} = 0$). For an excited state (one electron in HOMO and one in LUMO), there is one anti-symmetric spin configuration where $s_{\text{total}} = 0$ (referred to as a singlet state)

$$\frac{1}{\sqrt{2}}\left(|\uparrow\downarrow\rangle - |\downarrow\uparrow\rangle\right) \qquad s = 0 \text{ (singlet)} \tag{6.1}$$

and three symmetric spin configurations where $s_{\text{total}} = 1$ (referred to as triplet states)

$$\begin{matrix} |\uparrow\uparrow\rangle \\ \frac{1}{\sqrt{2}}\left(|\uparrow\downarrow\rangle + |\downarrow\uparrow\rangle\right) \\ |\downarrow\downarrow\rangle \end{matrix} \qquad s = 1 \text{ (triplet)} \tag{6.2}$$

when accounting for the indistinguishability of electrons [130].

The distinction between singlet and triplet states is important because during interactions with light, singlet states cannot couple into triplet states and vice versa (due to the requirement that electric transition dipole moment be nonzero). Therefore, if the ground state is a singlet (true for most materials including those involved in this work) then upon absorption of a photon, the only allowed transition is into the excited singlet configuration (and not into any of the three triplet configurations). The reciprocal is also true, meaning that triplet states cannot relax to the singlet ground state and thus have long lifetimes. In addition, because electrons are indistinguishable fermions and thus have exchange symmetry, when the spin state is symmetric (triplet) the spatial component of the wavefunction is anti-symmetric, and when the spin state is anti-symmetric (singlet) the spatial component of the wavefuntion is symmetric. A consequence of an anti-symmetric spatial wavefuntion for triplet states is a reduction in electron-electron repulsion which lowers the overall energy of the state relative to the excited singlet state for most materials. The difference in energy between excited singlet and triplet states depends on geometry and varies considerably from molecule to molecule [131].

6.1.2 Singlet Exciton Fission

While transitions from an excited singlet state to a triplet state are forbidden and require a spin flip, in materials where the singlet state energy is approximately twice as large as the triplet state energy, both energy and spin conservation can be upheld by generation of two triplet states (T_1) from an excited singlet state (S_1) and a ground singlet state (S_0) in a

process called singlet exciton fission (Figure 6-2)

$$S_0 + S_1 \underset{k_2}{\overset{k_{-2}}{\rightleftharpoons}} {}^1(TT) \underset{k_1}{\overset{k_{-1}}{\rightleftharpoons}} T_1 + T_1 \tag{6.3}$$

where ${}^1(TT)$ represents an intermediate triplet-triplet pair state with zero net spin (singlet character) and k_{-2}, k_2, k_{-1}, and k_1 represent the various rate constants [132, 133].

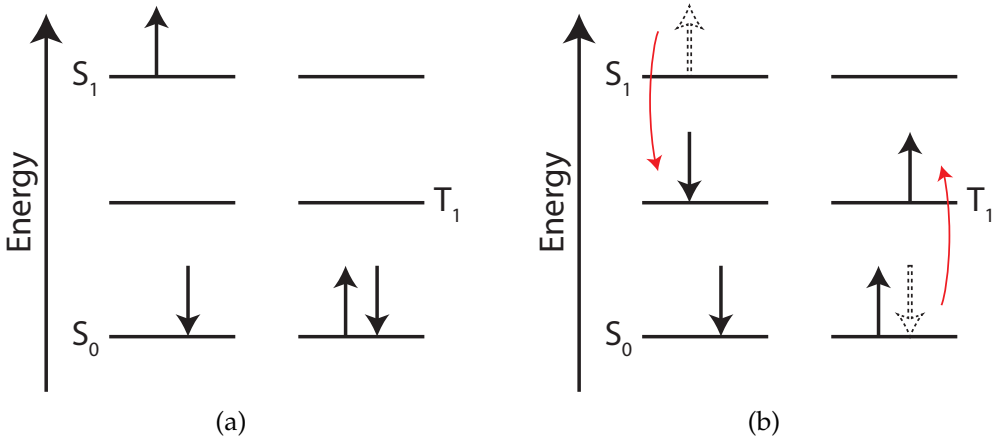

Figure 6-2: Schematic of singlet exciton fission process where (a) initial excitation of a chromophore generates S_1 which (b) subsequently shares its energy with a nearby chromophore in S_0 state to generate T_1 triplet states on both.

Singlet fission provides an opportunity for increasing solar cell efficiencies by potentially doubling the photocurrent from high energy photons. External quantum efficiencies (EQE) above 100 % at $\lambda = 670$ nm have been observed for organic-based solar cells where pentacene is the singlet fission material with triplet yields approaching 200 % [134]. However, the organic-based solar cells have much poorer efficiencies compared to conventional inorganic semiconductor solar cells [126]. This motivates the desire to pair organic singlet fission materials with an inorganic semiconductor. Figure 6-3 shows a schematic of an organic singlet fission material deposited on top of an inorganic solar cell. For a suitably chosen organic material, long wavelength light would be absorbed and collected by the inorganic solar cell in a typical manner. Higher energy photons with $h\nu > 2E_g$ would be absorbed by the organic material generating singlet states which would undergo fission to form two triplet states with approximately half the energy of the absorbed photon. Since the energy of the triplet states would be $\geq E_g$, it seems feasible that the energy could be transferred into the inorganic solar cell as two electron-hole pairs which could be collected like any other photon generated electron-hole pair to do work.

This scheme was first proposed in 1979 [135] but to date has not been successfully demonstrated. Although a theoretical quantum mechanical framework exists for the non-radiative transfer of energy from excited molecule states to nearby semiconductors via dipole-dipole interactions [136], poor agreement with experimental data has left open the question of how energy transfer actually occurs [137–141]. Furthermore, those previous experimental studies rely on verification of energy transfer via indirect methods (without

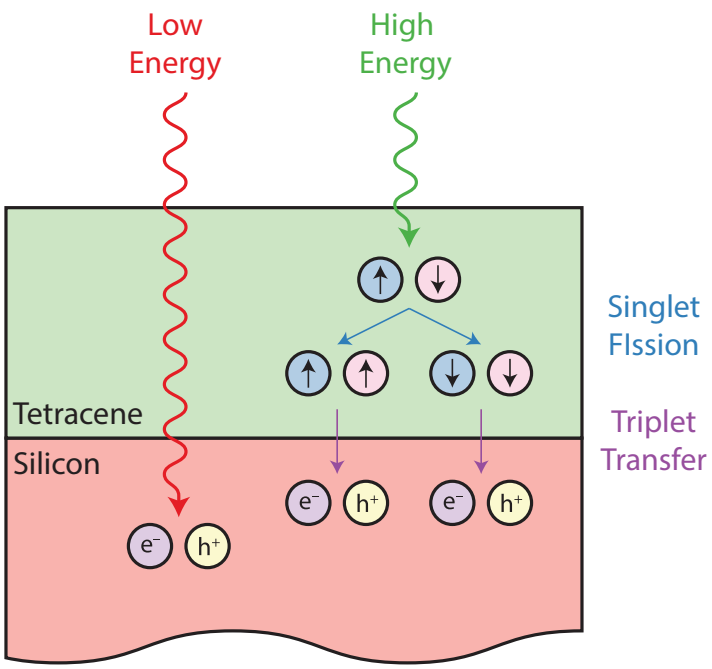

Figure 6-3: Schematic illustrating the potential benefit of adding a singlet exciton fission layer (e.g., Tetracene) to a Si solar cell.

accounting for surface recombination effects); therefore, while there is some evidence of transfer from singlet states to bulk semiconductors, no conclusive evidence exists showing that transfer of triplet states into bulk semiconductors is even possible. Due to uncertainty about direct energy transfer, many studies have looked at mechanisms to transfer triplet energy into bulk semiconductors via intermediates. Direct transfer of triplet states from tetracene to colloidal PbS quantum dots has been seen with transfer efficiencies of (90 ± 13)% [142]. Other experiments have show non-radiative exciton transfer from colloidal quantum dots into bulk silicon [143]. Together, these results show a possible path to increased efficiencies of inorganic cells via singlet fission.

Instead, this work investigates the direct transfer of triplet energy into an inorganic semiconductor which simplifies device design and limits potential losses. We focus our efforts on silicon; due to its dominance in the solar cell market, any improvements to Si solar cell efficiencies would have great impact. Of known singlet fission materials, tetracene is currently the most promising candidate for pairing with silicon. Tetracene has an S_1 energy of 2.32 eV and an T_1 energy of 1.25 eV [132]. This does indicate that tetracene (unlike pentacene) has an activation barrier to singlet fission of 0.18 eV. However, even at room temperature, the rate of singlet fluorescence is slow relative to the fission rate allowing for large fission efficiencies [144–146].

6.2 Modeling SRV Requirements

While the exact mechanism for energy transfer is unknown, it is reasonable to expect that energy from photons absorbed by tetracene and transferred into Si likely generates carriers located closer to the Si surface than if tetracene was absent and the photon had been absorbed directly by Si. Non-radiative energy transfer of excited states within molecules are primarily thought to occur by either (1) dipole-dipole coupling interactions also known as Förster resonance energy transfer (FRET) or (2) electron exchange via wavefunction overlap also known as Dexter energy transfer [147, 148]. FRET rate constants are proportional to $1/R^6$ where R is the separation distance. This leads to relatively efficient transfer over distances up to 100 Å in many molecular systems. However, triplet-triplet transfers are spin forbidden from FRET leading to the (speculative) assumption that transfer of triplets from tetracene to silicon will occur through a Dexter-like process. Because Dexter transfer requires wavefunction overlap, the transfer rate exponentially decays with separation distance and typically requires much shorter separations than for FRET. It should also be noted that at present, it is unclear what physically acts as the acceptor state in Si.

Because the surface acts as a recombination center, it is worth determining what surface conditions are required to see benefits from the addition of tetracene to a Si solar cell. In this section, we model what surface recombination velocity (SRV) is required for transfer to be useful assuming that transfer of energy from tetracene to silicon generates two electron hole pairs per incident photon (of sufficient energy) but places those carriers close to a surface which increases carrier recombination.

Solar cell simulations were made using PC1D[1] which solves the two-carrier semiclassical semiconductor transport equations coupled with Poisson's equation using a finite-element method. Figure 6-4 shows a representative plot of internal quantum efficiency (IQE) vs wavelength for Si solar cells with varying front SRV. The IQE is defined as

$$\text{IQE} = \frac{\text{\# of collected carriers}}{\text{\# of absorbed photons}} \tag{6.4}$$

and thus represents the fraction of generated carriers which are collected before recombination (minority carriers successfully diffuse to the junction). The IQE is maximum for wavelengths where carriers are primarily generated within a diffusion length of the junction (~900 nm). The decrease in IQE for shorter wavelengths results from the fact that high energy photons are absorbed closer to the surface and are therefore more influenced by the front surface recombination velocity. Similarly, the drop in IQE for longer wavelengths is related to the fact that carriers are generated throughout the wafer and longer diffusion distances are required for collection (bulk and rear surface recombination can reduce the number of collected carriers).

We assume that a benefit is received from addition of tetracene due to generation of triplet pairs from singlet fission if the IQE for carriers generated within ~10 nm of the surface

[1]PC1Dmod6.2 and PC1D for Matlab are available at https://www2.pvlighthouse.com.au/resources/PC1D/PC1Dmod6/PC1Dmod6.aspx

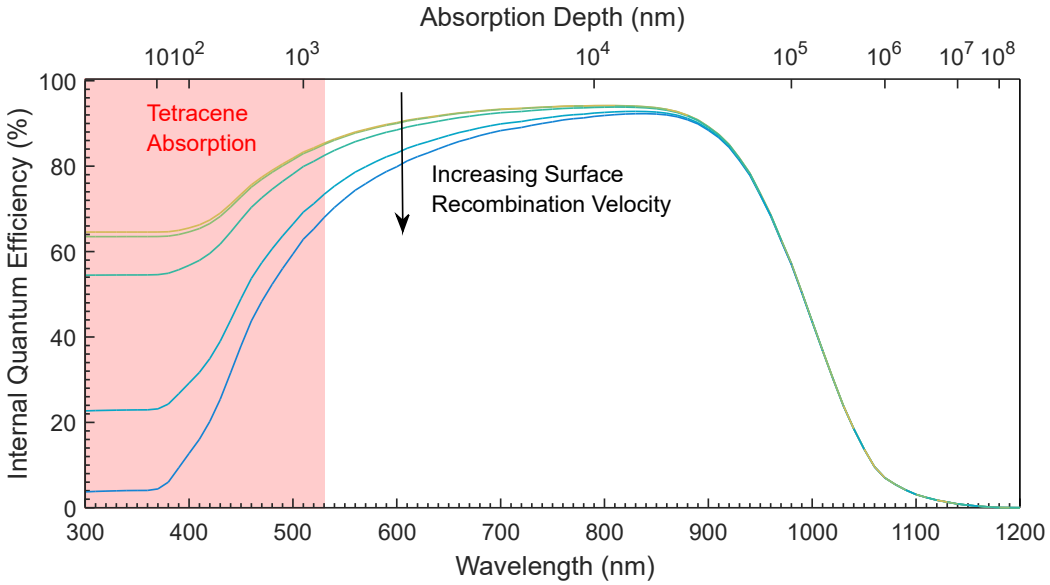

Figure 6-4: Sample representation of internal quantum efficiency (IQE) vs. wavelength for a typical Si solar cell with varying front surface recombination velocities ($10^2\,\mathrm{cm\,s^{-1}}$ to $10^6\,\mathrm{cm\,s^{-1}}$). Corresponding absorption depths for light in Si are plotted on the top x-axis. The red region represents the wavelength range that is absorbed by tetracene.

is at least half of the IQE at $\lambda = 530\,\mathrm{nm}$ which is approximately the tetracene bandedge:

$$\mathrm{IQE}_{\mathrm{surface}} > \frac{\mathrm{IQE}_{\lambda=530\,\mathrm{nm}}}{2}. \tag{6.5}$$

This qualification is useful for supplying an upper limit for the required SRV because the qualification that surface carrier IQEs be half as large as the IQE at $\lambda = x$, is easier to satisfy for all $x < 530\,\mathrm{nm}$ regardless of the SRV. In addition, as shown in Figure 6-4, the IQE for absorption depths less than 10 nm are approximately constant. Therefore, even though the exact mechanism for transfer is unknown, our estimates for SRV requirements should hold even if transfer occurs over a relatively long range of 10 nm.

For simplicity, uniform doping profiles are simulated (rather than ion implantation diffusion profiles) so that the solar cell regions have uniform diffusion lengths to allow for more intuitive interpretation of results. In addition, no mirror losses are assumed because standard anti-reflection coatings are designed with large losses from blue and green photons. An optimized tetracene on silicon solar cell would likely benefit from maintaining greater transmission in that wavelength range by using a different anti-reflection scheme.

6.2.1 Standard Solar Cell Design

For simulating a simple standard solar cell (200 µm thick), we have assumed an n-type emitter with $4 \times 10^{19}\,\mathrm{cm^{-3}}$ which corresponds to a diffusion length of ~1 µm. The base is p-type doped to $1 \times 10^{16}\,\mathrm{cm^{-3}}$ and no surface recombination at the backside is simulated. 1D simulations do not take into account lateral current flow to contacts and thus end up

optimizing for very thin emitter thicknesses which would result in losses due to high resistances. Therefore, our calculations of IQE for surface carriers and at $\lambda = 530\,\text{nm}$ are made as a function of emitter thickness (Figure 6-5). Two expected trends become apparent: (1) IQE drops drastically for both cases when the emitter thickness is longer than the average diffusion length and (2) the carriers at the surface are most effected by SRV.

Figure 6-6 shows a plot twice the IQE of surface carriers minus the IQE from carriers generated by $\lambda = 530\,\text{nm}$. This shows the effective increase or decrease in efficiency (in percentage points) due to generation of two electron hole pairs via singlet fission in tetracene with the trade-off being carriers are now located close to the surface which acts as a recombination center. As a general design rule, the emitter should be as thick as possible to reduce resistance while still being limited to approximately the diffusion distance of carriers in the emitter. From the result, we can determine that for an ideal device the emitter thickness should be no more than ~1 µm limiting the SRV to $10^4\,\text{cm}\,\text{s}^{-1}$ for optimal efficiency gains.

Slight relaxation of the SRV requirement can be accomplished by reducing the thickness of the emitter layer. In turn, this would require a closer contact spacing on the front surface in order to minimize resistance losses. This either (1) increases shading of the cell by the metal contacts or (2) requires thinner grid lines which in practice raises costs. Depending on the overall cell design and emitter resistance, if a more relaxed SRV requirement is needed, these trade-offs might be worthwhile to make. An overall optimization of the cell design requires knowledge of how SRV and transfer efficiency are related to cost (e.g., the best passivation is expensive but 80 % of the performance can be gained for a 10 % of the cost). At this early stage of research, these parameters are unknown making determination of an optimal cell design for commercial applications impossible. Currently, we are primarily concerned with understanding how SRV of the interface will impact the utility of adding tetracene to a silicon solar cell. Eventually, this work will be an integral part of determining the optimal design for a tetracene on Si solar cell.

The previous plots assume that the transfer efficiency of triplets is 100 %. Figure 6-7 shows how the efficiency changes when accounting for varying transfer efficiencies for two fixed emitter thicknesses (100 nm and 1 µm). Efficiency gains are only plotted as a function of triplet transfer efficiency down to 50 % because below that point there is no gain from generation of two triplets via a single photon compared to generation of a single electron hole pair in silicon. As expected, lower triplet transfer efficiencies reduce efficiency gains. In addition, the SRV requirements become slightly stricter for obtaining a net efficiency gain from when the triplet transfer efficiency decreases. Again, the SRV should be at most $10^4\,\text{cm}\,\text{s}^{-1}$ in order to extract the most efficiency gains.

We can also see that a greater transfer efficiency is required for significant benefit (>20 % increase) when the emitter thickness is close to the diffusion length. This implies that if the maximum transfer efficiency cannot reach near unity, then devices will need to be designed with shorter emitter lengths (potentially limiting the overall reduction to $/kWh as a result of adding tetracene to Si solar cells).

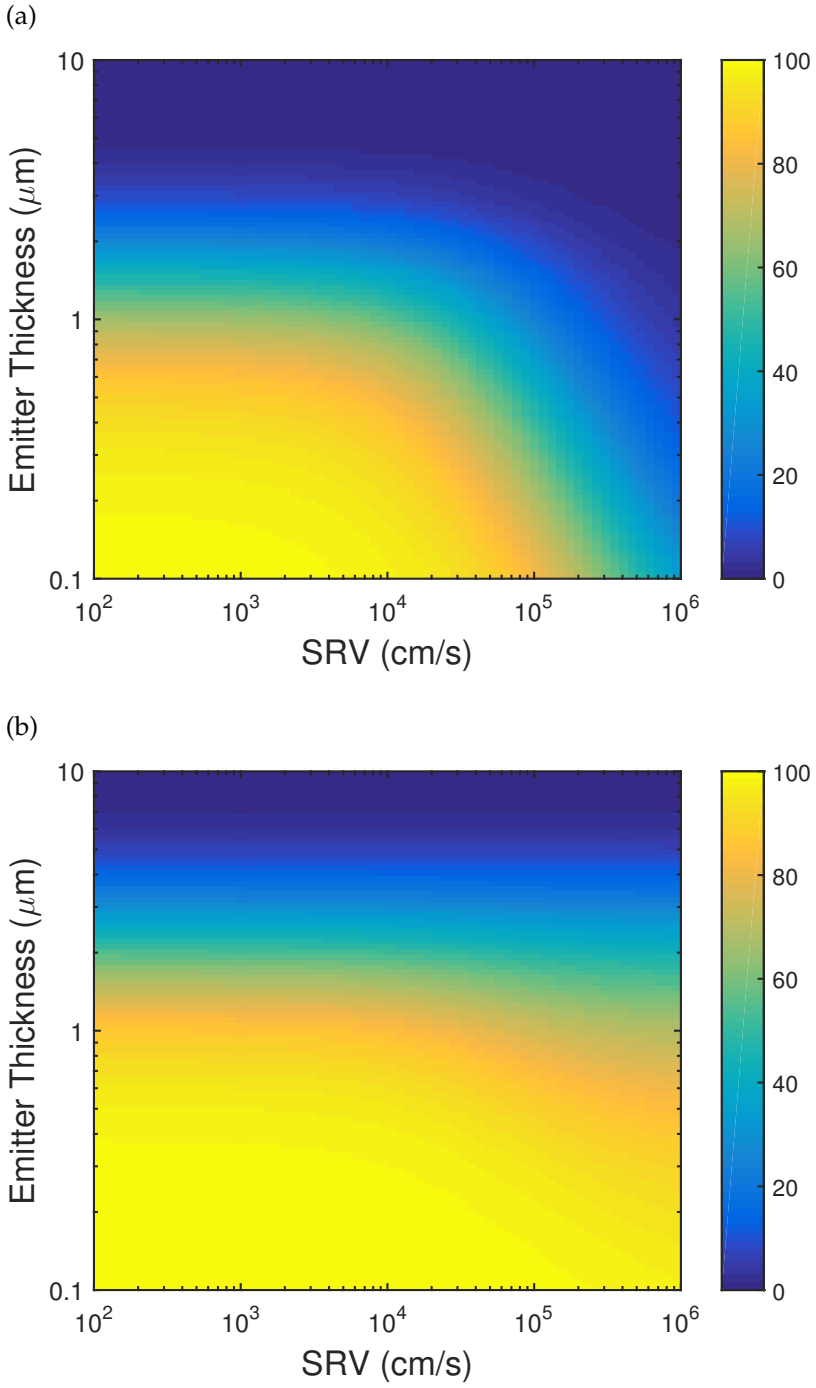

Figure 6-5: IQE for (a) surface carriers and (b) $\lambda = 530\,\text{nm}$ for varying emitter thicknesses and front surface SRV for a conventional Si solar cell design.

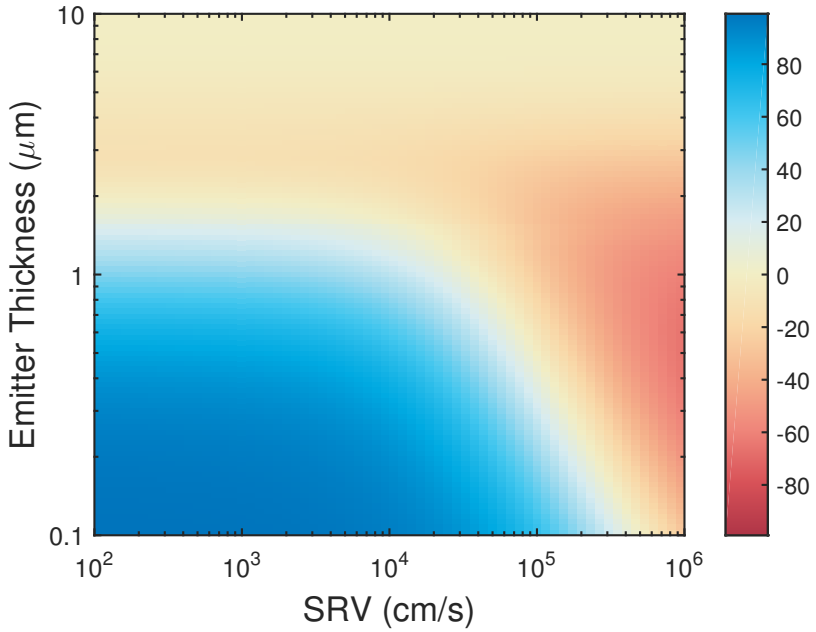

Figure 6-6: Changes in IQE resulting from addition of tetracene for varying emitter thickness and SRV for a conventional Si solar cell design.

6.2.2 Backside Illuminated Solar Cell

An alternative structure is a backside illuminated solar cell where illumination of the cell occurs on the surface of the base (the backside of a conventional cell). This design relies on diffusion of carriers a relatively long distance through the base to the junction. Therefore, these cells require well passivated surfaces and long bulk lifetimes to prevent carriers from recombining before reaching the junction. However, this is feasible in practice and is similar to the principle behind commercially produced solar cells fabricated by SunPower which currently hold the record for single crystalline Si solar cell efficiencies [126].

The Si doping concentration into which tetracene would transfer energy is a key difference between front illumination and backside illumination schemes. Even though the transfer mechanism is unknown, it is not unreasonable to expect that the Si doping concentration may have an effect on the transfer efficiency. If a specific band alignment is required for transfer, then changes in doping concentration will alter the Fermi level in Si changing its energy levels relative to tetracene.

Furthermore, as previously stated, it is unclear what acts as the acceptor state in Si. We can hypothesize that transfer is mediated by virtual acceptor states in Si which are induced by electrostatic interaction with excited states in tetracene. Because mobile charges can dampen the electric field (electric-field screening), the dopant concentration plays an important role in determining the extent of electrostatic interaction with silicon. We can estimate the distance into Si in which the interaction is still significant from the Debye

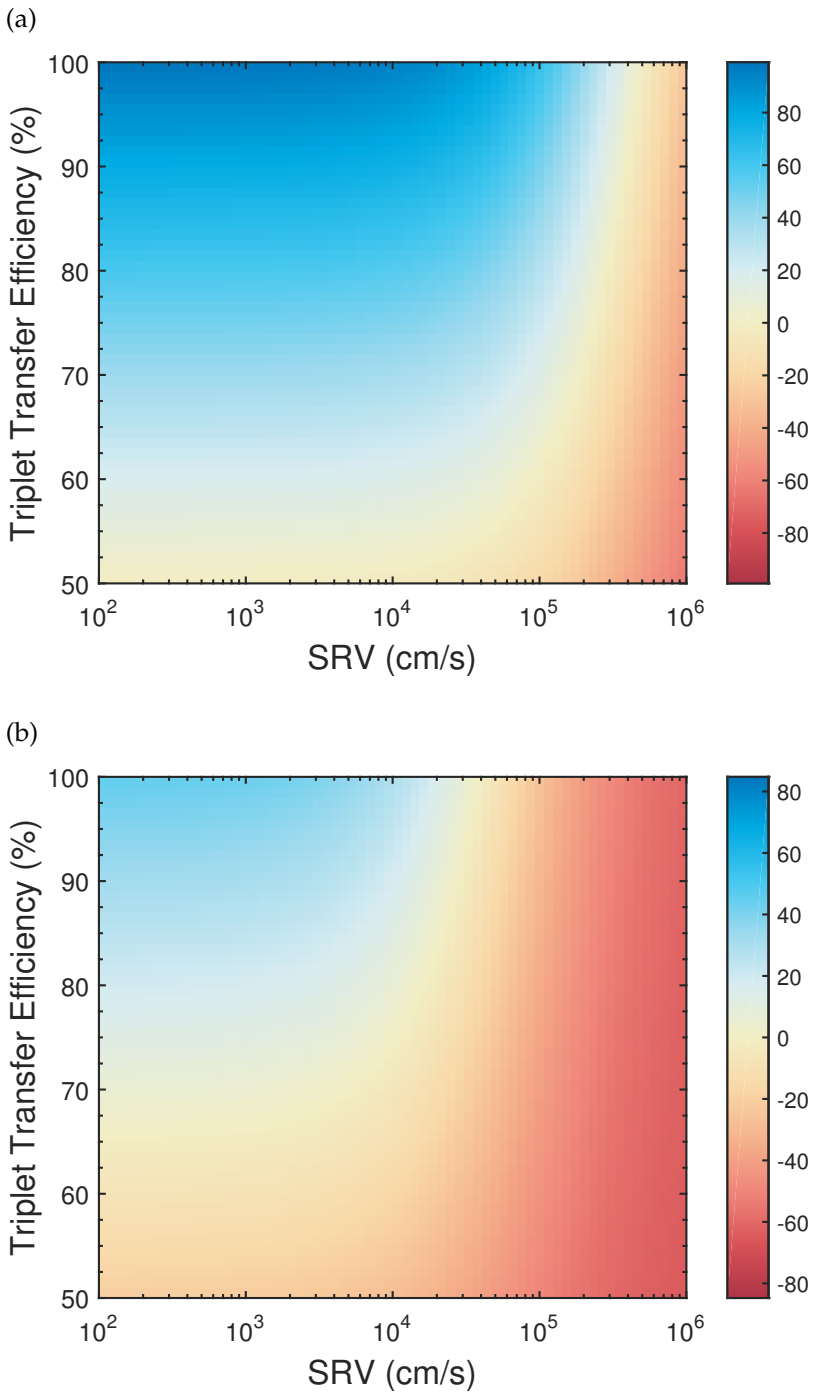

Figure 6-7: Changes in IQE for (a) 100 nm and (b) 1 µm emitter thickness for varying triplet transfer efficiencies and SRV for a conventional Si solar cell design.

length, L_D:

$$L_D = \sqrt{\frac{\varepsilon k_B T}{q^2 N_D}} \tag{6.6}$$

where N_D is the dopant concentration. At room temperature in Si, the Debye length varies from ~130 nm when $N_D = 10^{15}\,cm^{-3}$ to ~1 nm when $N_D = 10^{19}\,cm^{-3}$. Therefore, lower doping concentrations may improve transfer efficiencies. Because the emitter requires relatively high doping concentrations, this would favor combining tetracene with a backside illuminated solar cell.

Similar simulations as the previous section were run but the emitter thickness is now fixed. The emitter thickness only needs to be optimized for resistance rather than diffusion lengths. Furthermore, lateral conduction is no longer an issue as shading of the backside is not a concern. IQE simulations were instead run as a function of both SRV and bulk lifetimes which are more important now that the carriers have to diffuse a relatively large distance in order to be collected (Figure 6-8). Compared to a conventional solar cell, the absolute IQE is more sensitive to SRV in a backside illuminated solar cell. This holds true for both surface carriers and those generated by 530 nm light, even when the bulk lifetime is relatively long.

Similar to before, we can generate a plot of twice the IQE of surface carriers minus the IQE from carriers generated by $\lambda = 530$ nm (Figure 6-9). For this design, efficiency is never lost by the addition of tetracene. However, for long bulk lifetimes, there is a drastic decrease in the efficiency gain from ~100 % near $S = 10^2\,cm\,s^{-1}$ to ~0 % near $S = 10^4\,cm\,s^{-1}$. Therefore, even though the presence of tetracene will not decrease the efficiency, the SRV needs to be below $10^4\,cm\,s^{-1}$ for any practical efficiency gains. Figure 6-10 shows how the efficiency changes when accounting for varying transfer efficiencies assuming a bulk lifetime of 1000 µs. Compared to the conventional cells, the SRV requirements for efficiency gains increase more sharply as transfer efficiency decreases. In addition, the transfer efficiency needs to exceed ~60 % for any significant gains.

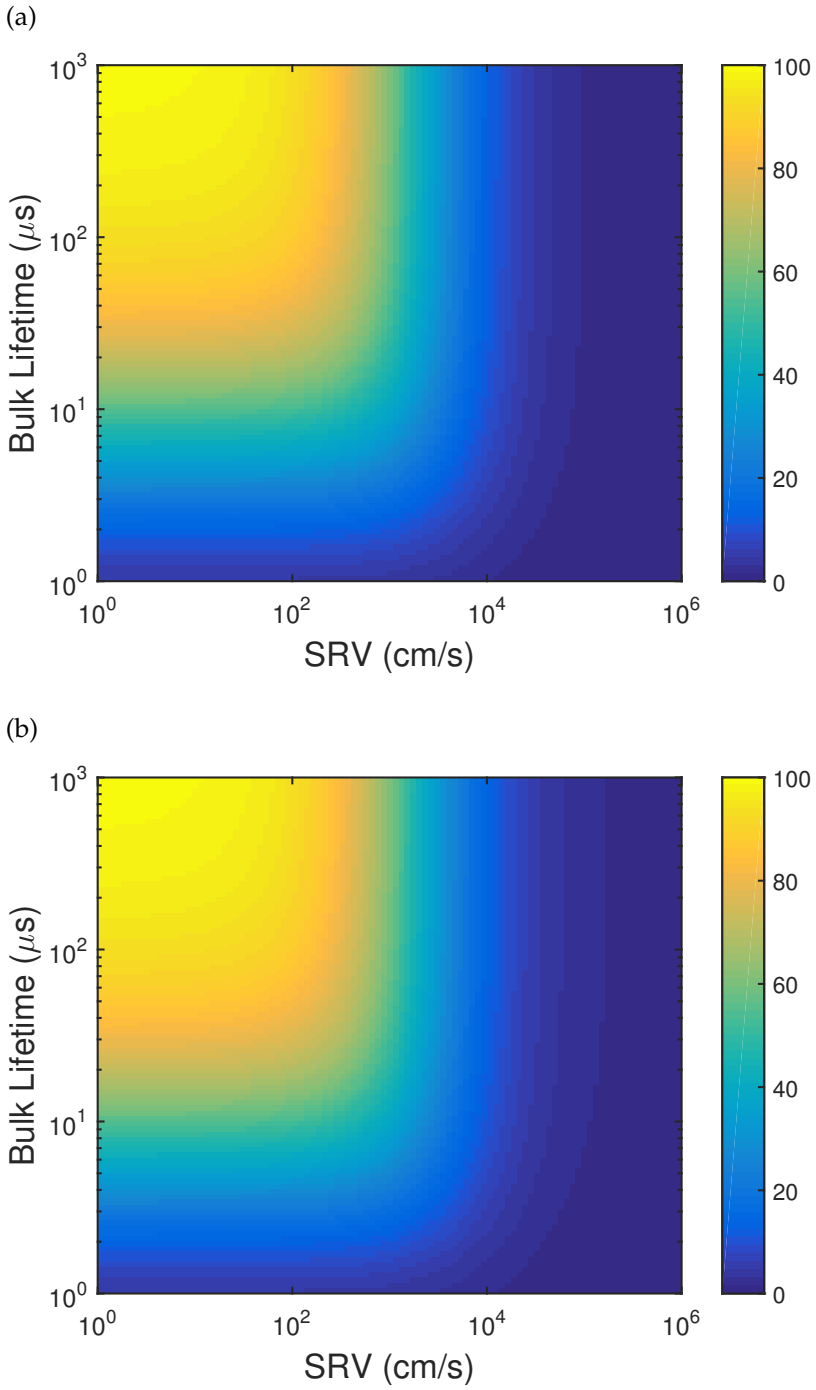

Figure 6-8: IQE for (a) surface carriers and (b) $\lambda = 530\,\text{nm}$ for varying bulk lifetimes and SRV for a backside illuminated Si solar cell design

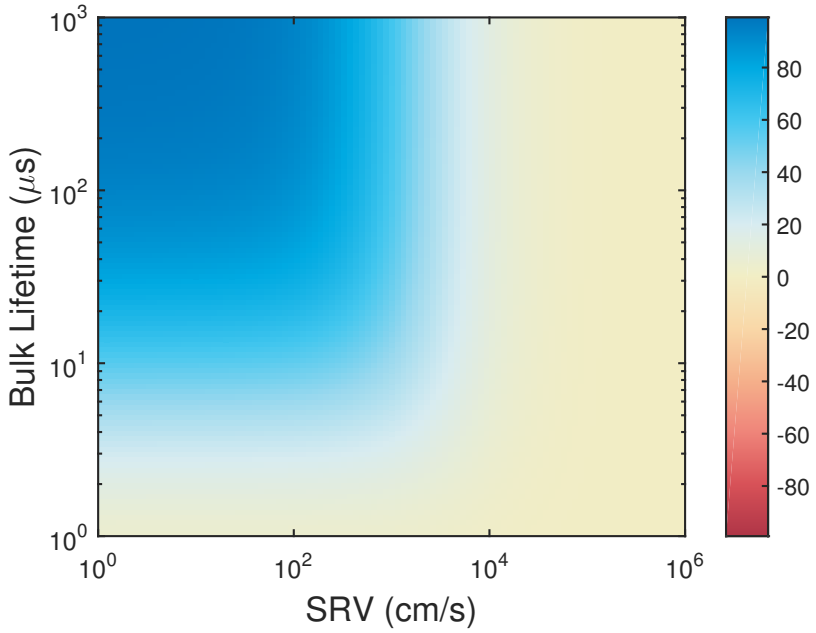

Figure 6-9: Changes in IQE resulting from addition of tetracene for varying bulk lifetimes and SRV for a backside illuminated Si solar cell design.

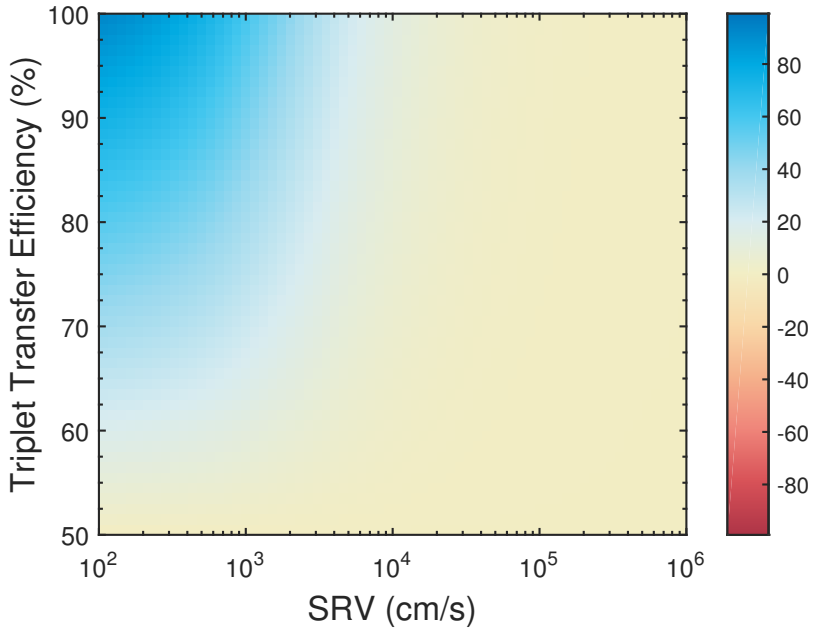

Figure 6-10: Changes in IQE for varying triplet transfer efficiencies and SRV for a backside illuminated Si solar cell design (assuming 1000 µs lifetimes).

6.3 Radio Frequency Photoconductivity Decay (RFPCD)

For either proposed solar cell structure, the quality of the interface between tetracene and silicon is of great importance requiring that the interface be well passivated. Transient radio frequency photoconductivity decay (RFPCD) measurements which are typically used to measure minority carrier recombination lifetimes can provide a quick and contactless method to determine the quality of the silicon surface. The basic operating principle of RFPCD was first developed by Miller in 1976 [149]. A schematic of our RFPCD experimental apparatus is shown in Figure 6-11. The conductance of a wafer is inductively measured through the use of an RF coil which acts as the primary of a transformer while the wafer being measured acts as a short-circuited secondary. A pulsed LED light source is used to optically generate excess carriers increasing the conductivity of the material.

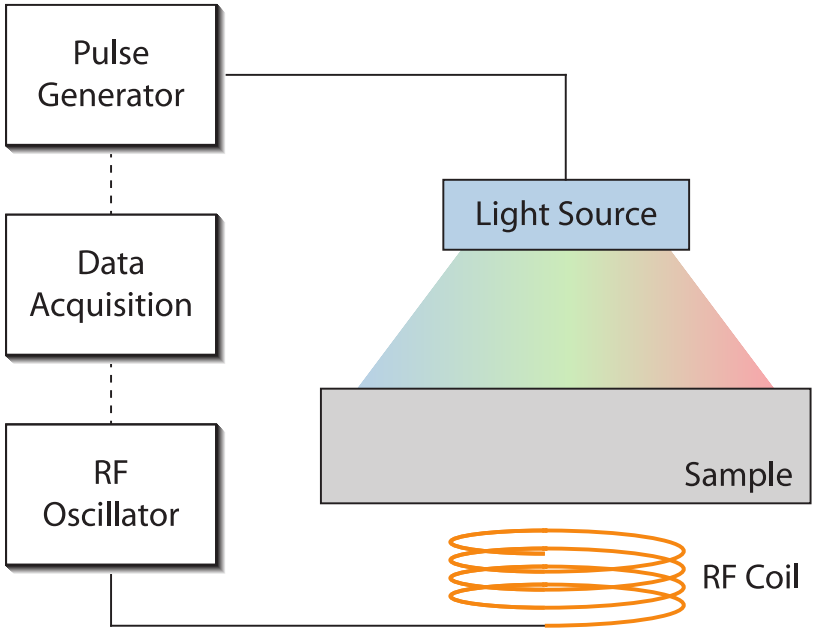

Figure 6-11: Schematic of RFPCD experimental apparatus.

Because generation and recombination processes balance (Section 2.1), the change in excess carrier concentration (which is proportional to the measured signal) with time can be calculated from

$$\frac{d\Delta n}{dt} = G - U = G_{\text{external}} - \frac{\Delta n}{\tau} \tag{6.7}$$

where G_{external} is the generation rate due to some external source which is the LED light source. If our illumination is kept constant during excitation ($G_{\text{external}} = g$) then

$$\Delta n = g\tau \left(1 - e^{-t/\tau}\right). \tag{6.8}$$

After the illumination is removed ($G_{\text{external}} = 0$) then

$$\Delta n = g\tau e^{-t/\tau}. \tag{6.9}$$

Figure 6-12 shows a schematic of the output signal during an RFPCD measurement illustrating the rise in signal during illumination and the decay after the light source is removed. The decay of the RFPCD signal is recorded after the light source is removed and is analyzed to determine the effective minority carrier lifetime which contains both bulk and surface components. For this work we are primarily concerned with recombination at the surface. Taking the derivative of Equation 2.22 yields

$$\frac{\partial \tau_{\text{eff}}}{\partial \tau_{\text{surf}}} = \left(1 + \frac{\tau_{\text{surf}}}{\tau_{\text{bulk}}}\right)^{-1} \tag{6.10}$$

which shows that our sensitivity to changes in surface lifetime increase when the bulk lifetime increases. In addition, for long bulk lifetimes, the contribution of bulk effects to the measured effective carrier lifetime is negligible. Therefore, in this work, all Si substrates used have bulk lifetimes of ~5 ms or greater. Bulk lifetimes were verified by RFPCD measurements while immersed in (hydrofluoric acid) HF which provides hydrogen passivation of the surfaces (S close to zero) [150].

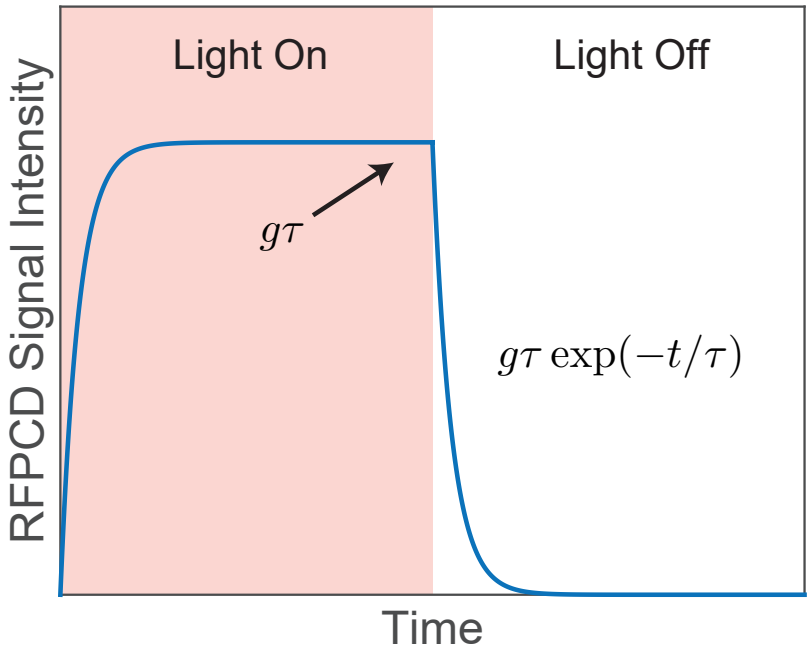

Figure 6-12: Schematic of RFPCD signal output during measurement illustrating how the signal depends on carrier lifetimes and generation rates.

It is also important to note that for high surface recombination velocities ($\gtrsim 10^3$ cm s^{-1}), carrier diffusion to the surface is the rate limiting step for recombination. This puts a lower limit on measured effective carrier lifetimes (approximately equal to the average time it

takes a carrier to diffuse to the surface) of

$$\tau_{\text{eff}} = \frac{d^2}{D\pi^2} \tag{6.11}$$

where d is the wafer thickness and D is the diffusivity of the minority carrier. For the wafers employed in this work, this corresponds to about 38 µs (6-inch, 5×10^{11} cm^{-3} doping n-type) and 44 µs (8-inch, 5×10^{14} cm^{-3} doping n-type). For low surface recombination velocities $< d/\tau_{\text{bulk}}$, the effective carrier lifetime is essentially a measure of the bulk lifetime. In the intermediate range, the surface recombination velocity can be approximated from the effective lifetime by the following expression:

$$\tau_{\text{eff}} = \frac{d}{2S}. \tag{6.12}$$

6.3.1 Determination of Transfer Yields via RFPCD

Another important feature of Figure 6-12, is that when the pulse duration is much larger than the effective lifetime ($t_{\text{pulse}} \gg \tau$), the signal saturates during illumination at a value equal to $g\tau$. Therefore, by employing long pulses we can extract information about the generation rate of carriers in the silicon once τ is extracted from the decay transient. Obtaining absolute measurements of the generation rate using this method are difficult in practice due to the need for calibration measurements and careful control of experimental parameters (e.g., illumination intensity, distribution, and position relative to sample and coil). Therefore, $g\tau$ extracted from RFPCD is typically ignored. However, comparison of similar samples under controlled conditions can yield useful information about relative changes in generation rate. Figure 6-13 shows a schematic of how comparison of RFPCD measurements can be used to determine if energy is transferred from tetracene to silicon. First measurements are made using a sample without tetracene to establish a baseline generation rate. Then a sample tetracene deposited onto a similar sample is measured and the obtained generation rates are compared. When the illumination wavelength is greater than the tetracene absorption band edge, if no energy transfer is occuring, then the signal should decrease based on the amount of the light absorbed by tetracene which can be estimated from the Beer-Lamber law

$$1 - \frac{I(d)}{I_0} = 1 - \exp(-\alpha d) \tag{6.13}$$

where $1 - I(d)/I_0$ is the fraction of absorbed light, d is the thickness of tetracene, and α is the absorption coefficient of tetracene which can be related to the imaginary component of the refractive index, κ, by

$$\alpha = \frac{4\pi\kappa}{\lambda} \tag{6.14}$$

where λ is the wavelength of light. If the ratio of the generation rate without tetracene to with tetracene exceeds the fraction of absorbed light, then some of the energy absorbed by the tetracene is being transferred to silicon. This alone, however, does not indicate whether transfer involves any triplet states generated via singlet fission. Excited singlet states can transfer into silicon as well as fluoresce leading to absorption of some fraction of fluoresced

photons by silicon. If 100 % of the energy absorbed in tetracene generated only singlet states which transfer to silicon with 100 % efficiency, then the RFPCD signal would be unaffected leading to a ratio of generation rates without and with tetracene of 1. Therefore, if the generation rate without tetracene to with tetracene exceeds unity, this indicates that transfer of triplets generated by singlet fission is at least partially responsible for the measured signal.

In order to control for unwanted sources of RFPCD signal intensity variations, samples are made to the same size, placed in the same location relative to the coil, and are covered with an aperture which only allows excitation of carriers near the center of the sample to reduce edge effects. In addition, the Gaussian LED source is placed relatively far away so that the combination of distance and use of an aperture ensures even illumination onto the sample. Intensity variations seen due to reflectivity variations of samples can be corrected for by measurement of reflection spectra using an integrating sphere to capture light reflected at all angles. Additionally, as a verification, measurements can be made using a wavelength of light that is absorbed by silicon but not tetracene. Samples with and without tetracene should see no change and the generation rate ratio should equal 1. In this work, we have primarily used 470 nm (strong tetracene absorption) and 850 nm (no tetracene absorption) LEDs for excitation during measurements.

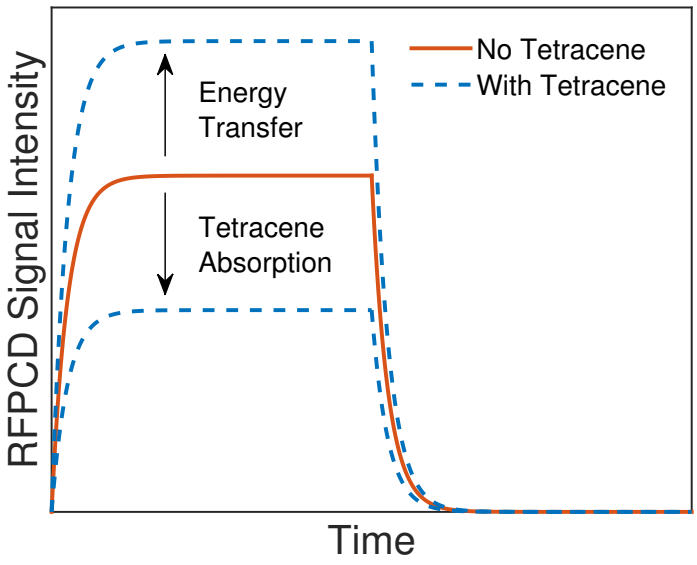

Figure 6-13: Schematic of RFPCD transfer yield measurements by comparison of generation rates for samples with and without tetracene.

6.4 Magnetic Field Effect Measurement Methodology

As mentioned before, many previous studies have investigated singlet states by transient observation of fluorescence which often yields inconclusive information about triplet states. Because triplet states do not fluoresce, other techniques are required to make more conclusive observations about triplet populations.

One such technique applicable to both photoluminescence and photocurrent measurments is to observed changes in signal intensity as a function of applied magnetic field. Singlet fission rates are dependent on external magnetic fields as explained by the Merrifield model [151, 152]. As shown in Equation 6.3, during singlet fission, intermediate triplet-triplet pair states form. For spin conservation to hold, the pair state must have singlet character. Looking at all the possible spin combinations for a triplet-triplet pair, at zero magnetic field there are three possible triplet-triplet pairs with singlet character. For small applied magnetic fields, the number of singlet character pairs increases. For large applied magnetic fields, the number of singlet character pairs decreases to 2. The fission rate, k_{fis}, depends on the number of possible singlet character states, N, in the following way

$$k_{\text{fis}} \propto \frac{N}{{}^{k_2}/_{k_{-1}} + N} \tag{6.15}$$

which means that the singlet fission rate can be reduced by application of a magnetic field. Therefore, when we are monitoring a process in which there is competition between singlet and triplet states, changes in the signal can indicate contributions from triplet states as seen in Figure 6-14 for fluorescence and photocurrent from a tetracene based organic solar cell. Under applied magnetic as the singlet fission rate decreases, competition to singlet fluorescence from singlet fission is reduced leading to increased singlet fluorescence signal. Conversely, photocurrent measurements of the same device show a decrease with magnetic field indicating that non-emissive triplet states are contributing to the observed photocurrent signal.

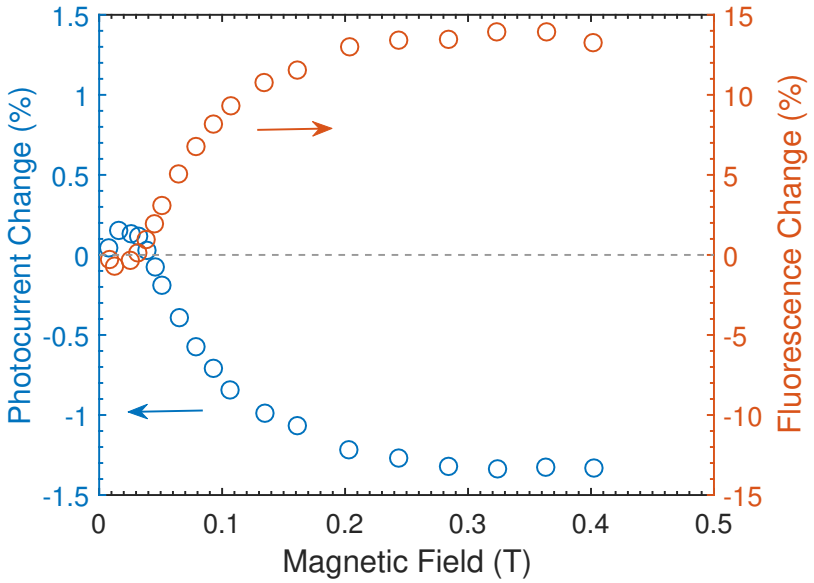

Figure 6-14: Example of using magnetic field effect measurements to identify triplet contributions to signal as seen for fluorescence and photocurrent from tetracene based organic solar cells. *Reproduced from [146]*

In addition to analysis of generation rate ratios via RFPCD, we propose using measure-

ments of Si photoluminescence as a function of applied magnetic field to determine whether or not energy from triplets are transferred into silicon. Even though Si photoluminescence is weak, using a lock-in amplifier and signal averaging, we can reliably detect signal changes of ~0.1 %. Fluorescence from singlet emission in the visible will be filtered out such that all measured PL signal originates from recombination in silicon. An observation of decreased signal after application of a magnetic field would then indicate that some fraction of the Si PL is related energy transferred from triplet states which decreased under an applied magnetic field due to the decreased singlet fission rate. As a verification that Si itself does not have any complicating effects, we have made measurements of Si without tetracene and observe no changes in Si PL with applied magnetic field.

In some applications, when many of the relevant competing reactions and their rates are well understood, models can be built which can accurately extract efficiencies from magnetic field effect measurements. In this case however, at the moment we feel that we do not have a reliable enough model to determine absolute yields from magnetic field effect measurements. Instead, we present them as evidence of triplet contributions and look at qualitative trends.

6.5 Surface Passivation of Silicon via Thin Films

Figure 6-15a shows an effective carrier lifetime from Si wafer pieces immersed in HF which forms a well passivated surface of ~4.3 ms. This is quite long compared to the lifetime measured for bare Si of ~45 µs (Figure 6-15b) which is actually close to the limit we can measure indicating that without any treatment, the surface recombination velocity is $>10^3$ cm s^{-1}. Ideally, tetracene itself could provide adequate passivation of the Si surface. However, deposition of tetracene directly onto Si does not provide much passivation compared to any native oxide that had formed on the bare Si sample. In this work, tetracene is deposited via thermal evaporation by collaborators in the Baldo group.

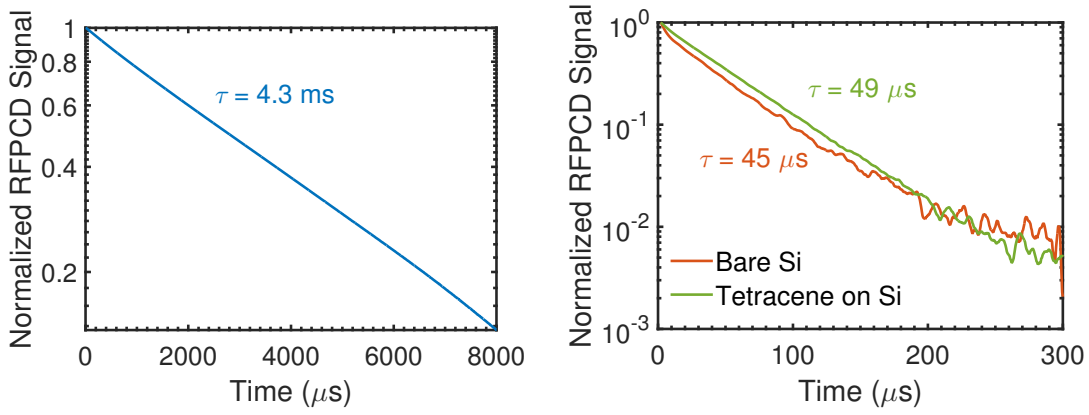

(a) (b)

Figure 6-15: Comparison of lifetimes (850 nm excitation) from 1" x 1" Si wafer pieces (5×10^{14} cm^{-3} n-type) when (a) immersed in HF to form a well passivated surface and (b) left bare and with a 20 nm tetracene film.

6.5.1 Estimation of Transfer Dependence on Barrier Width

Because tetracene cannot provide sufficient passivation, another material must be sandwiched between tetracene and Si in order to reduce surface recombination. As previously mentioned, the triplet energy transfer mechanism is not precisely known but the presence of an intermediate material is likely to affect the transfer efficiency. Therefore, it is useful to model the effect of a passivating barrier material on the transfer efficiency of triplet excitons into electron-hole pairs in silicon. A schematic of the relevant reactions are shown in Figure 6-16. In order to make a simple model, we only need to focus on the rate limiting steps and most reactions can be ignored. For tetracene, excited singlet (S_1) states will quickly undergo singlet fission to form triplet (T_1) states. We can neglect the backwards reaction (triplet-triplet annhilation) for isolated triplet pairs based on the relatively low probability of two triplets diffusing to each other before diffusing to interface. We can also neglect diffusion of the triplets to the surface based on the quick diffusion of triplets relative to their lifetime. Once at the interface, we can assume that based on the energy difference, triplets will preferentially attempt to transfer their energy into silicon rather than diffuse back into the bulk of the tetracene layer. This assumption may not be entirely correct and can possibly lead to overestimation of the transfer efficiency. Greater understanding of the transfer mechanism is required for more precise modeling. If the tetracene is relatively thin, singlet states may also have time to diffuse to the surface and non-radiatively transfer energy into silicon before singlet exciton fission. In this model, we will assume a relatively thick tetracene layer and neglect competition from singlet transfer.

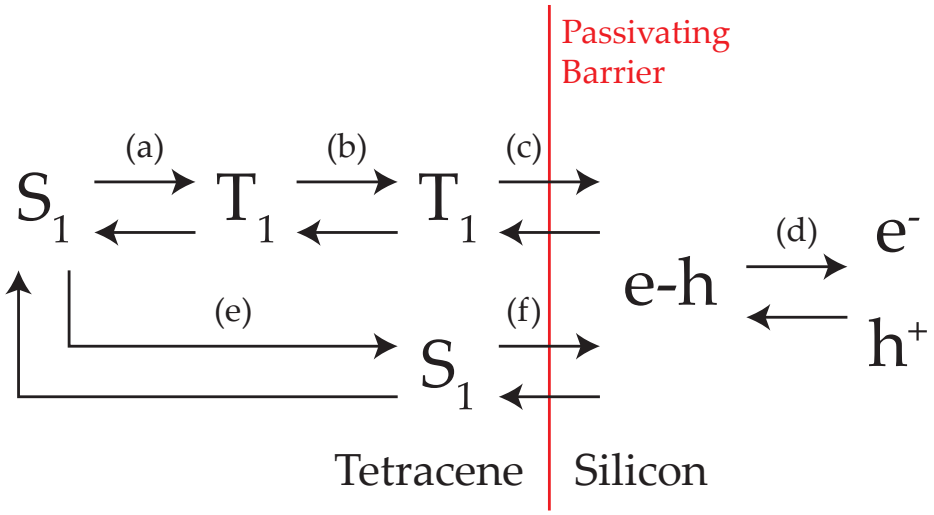

Figure 6-16: Schematic of the various reactions involved in the transfer of triplet exciton energy into silicon: (a) Singlet exciton fission, (b) triplet diffusion to the interface, (c) transfer of triplet state energy into acceptor state in silicon forming electron-hole pair, (d) dissociation of electron-hole pair into free carriers, (e) singlet diffusion to the interface, and (f) transfer of singlet state energy into acceptor state in silicon forming electron-hole pair. The described reactions are reversible and have corresponding backward reactions.

If we assume that transfer occurs due to a Dexter-like process, we can make a rough

estimation of the transfer rate dependence on thickness by modeling triplet transfer from tetracene to silicon as tunneling through a potential barrier due to wavefunction overlap. For 1-D quantum mechanical tunneling through a finite barrier, the transmission rate when $E < V_0$ is

$$T = \left[1 + \frac{V_0^2 \sinh^2(ka)}{4E(V_0 - E)}\right]^{-1} \tag{6.16}$$

where

$$k = \sqrt{\frac{2m(V_0 - E)}{\hbar^2}} \tag{6.17}$$

where V_0 is the barrier height, a is the barrier width, E is the particle energy, and m is the mass of the particle. We estimate the energy of the tunneling particle as the energy difference between tetracene triplet state and silicon bandgap (1.25 eV − 1.12 eV = 0.13 eV) and the barrier height to be the difference in electron affinities of Si and SiO_2 (4.05 eV − 0.95 eV = 3.1 eV). This estimation only considers transport of electrons and assumes no band alignment effects therefore yielding only a rough approximation. However, this calculation is useful for providing an indication of the separation distances required for transfer. Figure 6-17 shows that the transmission rate drops off sharply within 20 Å.

The calculated transmission rate gives the probability that an incident energetic particle can tunnel across a barrier. The actual triplet transfer rate (k_{trans}) is modified by the fact that triplet states attempt to tunnel through the barrier multiple times:

$$k_{\text{trans}} = T\nu_{\text{attempt}} \tag{6.18}$$

where ν_{attempt} is the tunneling attempt frequency and can be estimated by the triplet hopping rate in tetracene, $\sim 10^{13}\ \text{s}^{-1}$ [153]. If there were no competing processes, even for slow transfer rates, the triplets would always eventually transfer to silicon. However, due to competing processes (e.g., intersystem crossing and phosphorescence, triplet-triplet annihilation) we expect triplet states can decay before transfer. The triplet state lifetime (τ_{triplet}) in tetracene is relatively long compared to singlet states, and has been observed to be a long as ~50 µs for bulk single crystal tetracene. However, measurements of thermally evaporated thin films of tetracene (similar to the material used in this work), show much shorter triplet state lifetimes of ~50 ns which is hypothesized to be related to increased recombination at surfaces [145]. Assuming first order reactions, we can estimate the actual transfer yield of triplets in tetracene from

$$\text{Transfer Yield} = \frac{k_{\text{trans}}}{k_{\text{trans}} + \tau_{\text{triplet}}^{-1}} \tag{6.19}$$

which has been plotted a function of barrier width in Figure 6-18. While near unity transfer can be expected for ultra thin barriers, the transfer efficiency begins to drastically decrease once the barrier becomes thicker than ~2 nm. Therefore, based on these calculations and our models for SRV requirements, a challenge to obtaining practical efficiency gains from adding tetracene to a Si solar cell will be to develop a method for adequately passivating the Si surface using an ultra thin barrier.

It should be noted that we neglected backtransfer of energy from silicon into tetracene.

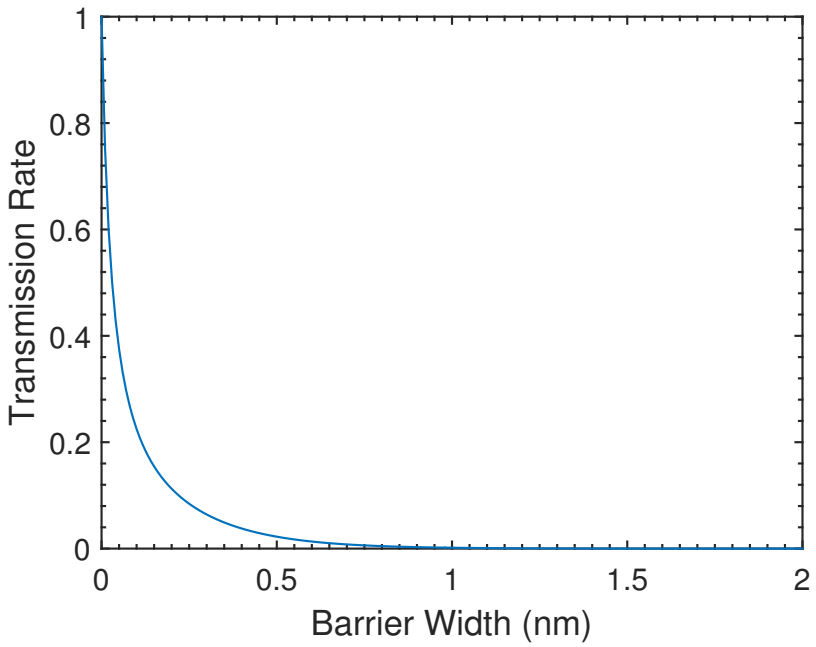

Figure 6-17: Estimation of triplet transfer rate dependence on barrier width by approximating transfer as tunneling through a finite potential barrier.

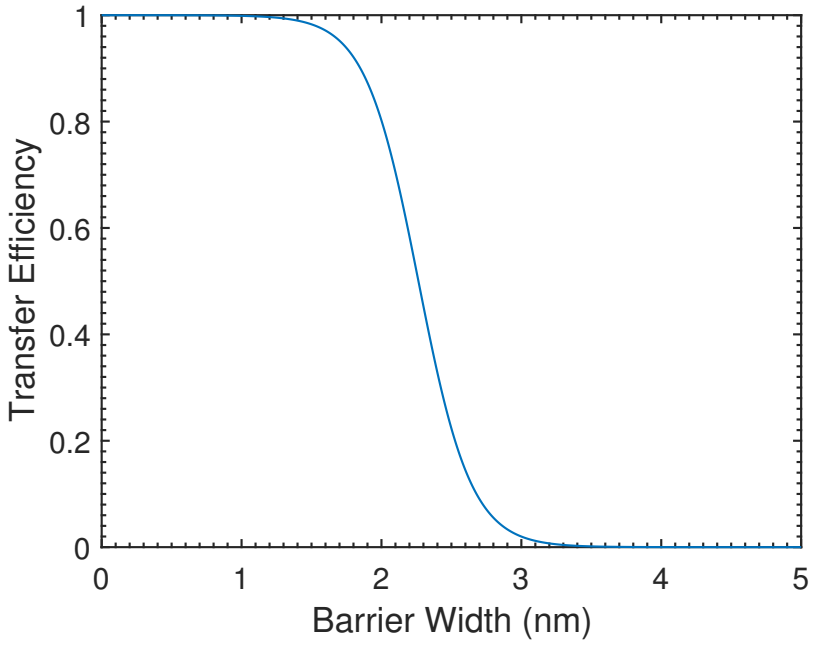

Figure 6-18: Estimation of triplet transfer efficiency on barrier width.

Because excitons have very small binding energies in conventional semiconductors, we expect quick dissociation of the excited acceptor state in Si into free carriers. Assuming the Si state is required for transfer (and is potentially induced by the triplet state in tetracene), this would make the backwards transfer reaction rate negligible. Moreover, even if the Si state exists and allows for backtransfer, the triplet state has a higher energy than an electron-hole pair in Si. We can make an optimistic estimate for the backtransfer rate assuming an Arrhenius dependence where the activation energy is the same energy difference used to model tunneling from tetracene into Si:

$$k_{\text{backtrans}} = T\nu_{\text{debye}} \exp\left(\frac{-0.13\,\text{eV}}{kT}\right) \tag{6.20}$$

which at 300 K leads to

$$k_{\text{backtrans}} \approx 0.06 k_{\text{trans}} \tag{6.21}$$

meaning that even optimistically, we expect the backtransfer rate is small relative to the transfer rate and can be safely ignored in our simple model.

6.5.2 Dry Thermal Oxidation

The standard method for passivation of Si is thermal oxidation which typically results in SRV <10 cm s^{-1} [154]. Rather than deposition of SiO_2 onto the exposed Si surface, thermal oxidation processes drive an oxidizing species (either H_2O or O_2) to the Si surface (diffusing though any oxide that already exists) where it then reacts with Si to form SiO_2 through one of the following reactions

$$Si + 2\,H_2O \longrightarrow SiO_2 + 2\,H_2 \qquad \text{Wet Oxidation} \tag{6.22}$$

$$Si + O_2 \longrightarrow SiO_2 \qquad \text{Dry Oxidation} \tag{6.23}$$

typically at temperatures from 800 °C to 1000 °C. A large advantage of thermal oxidation compared to chemical vapor deposition (CVD) or physical vapor deposition (PVD) methods is the film is grown at the silicon/oxide interface resulting in good passivation even if the starting top surface is not pristine. In this work, we use dry thermal oxidation reactions due to the superior passivation quality even compared to wet oxidation. In addition, wet oxidation film growth is much quicker and is typically used for thick film growth (>100 nm).

The standard model for predicting oxide thickness from thermal oxidation is the Deal-Grove model [155]. This model, however, is not very accurate for modeling films with thicknesses <30 nm and has subsequently been supplemented by empirical data (Massoud model) for application to thinner films [156, 157]. Even these models are only reliable down to film thicknesses of ~25 Å due initial rapid oxidation [158]. A few studies exists which make *in situ* thickness measurements for various dry oxidation parameters but do not qualify the quality of the oxide with regards to passivation or surface recombination [159, 160].

For efficient triplet transfer, we need to develop a process for fabrication of highly passivating thin films. Therefore, we have used RFPCD to determine the impact of oxide thickness (fabricated by dry oxidation) for very thin films on surface passivation. Table 6.1

contains a summary results from dry oxidations including the growth parameters and the resulting thicknesses as measured by spectroscopic ellipsometer. It should be noted that spectroscopic ellipsometry is nominally accurate to ±2 Å but in practice accurate measurement of very thin oxides is difficult as seen by studies comparing various thickness measurement methodologies [161]. Also, the Si used in these experiments were high resistivity (>10 000 Ω cm) float zone wafers which showed some injection level dependence on carrier lifetimes. Therefore, we only report approximate lifetimes which give an indication of surface quality.

Oxide films down to 14 Å were successfully fabricated by dry oxidation showing the potential for this technique to form thin barrier layers through which tunneling is possible. However, with the current process, there is a clear trade-off in passivation quality as films formed by short, low temperature growths have lifetimes almost two orders of magnitude lower indicating significantly larger SRV.

Table 6.1: Summary of results from fabrication of thin oxide films via dry oxidation

Sample Label	Temperature (°C)	O_2 Flow Duration (min)	Thickness (Å)	Effective Carrier Lifetime (ms)	Surface Preparation[a]
A	800	50	57	~5	SC2
B	800	10	33	~5	SC2
C	700	2	21	~5	SC2
D	700	2	19	~5	HF
E	700[b]	2	17	~0.05 to 0.1	SC2
F	700[b]	2	14	~0.05 to 0.1	HF

[a] Wafers are RCA cleaned immediately before oxidation. This column signifies whether samples were given an additional HF dip after SC2 to strip any oxide formed.
[b] The furnace was cooled to 400 °C before sample loading and then slowly ramped to the growth temperature.

6.5.3 Atomic Layer Deposition

Another method used in this work to fabricate thin oxide films was plasma-enhanced atomic layer deposition (ALD). Deposition mechanism is similar to chemical vapor deposition but the surface is exposed to separate precursors in repeated, sequential steps allowing for layer-by-layer control of deposition giving precise control over the final film thickness. The growth rate for SiO_2 for the process used is ~0.91 Å per cycle (as calibrated by measurement of a 100 cycle film using spectroscopic ellipsometry). Films were fabricated using 5 cycles, 11 cycles, and 55 cycles with the expectation of yielding ~5 Å, ~10 Å, and ~50 Å thick films. Spectroscopy ellipsometry for 5 cycles and 11 cycles films yielded anomalously large thicknesses making the real values uncertain. Therefore, the sample thicknesses for ALD films will be reported based on the calibrated thickness per cycle. It is not unreasonable that spectroscopic ellipsometry may give anomalous results due to the thickness being extracted using complex refractive index data for thermal oxide films. Differences in film

densities between the two fabrication methods can lead to index of refraction variations which may have resulted in the erroneous thickness values.

Our ALD process produces short lifetimes comparable to the thinnest dry oxide films of approximately 40 µs to 120 µs. Representative RFPCD measurements from ALD deposition of SiO_2 are shown in Figure 6-19. A key difference between dry oxidation and ALD deposition is that while ALD gives more control over deposition rate, the film is deposited directly onto the surface of the sample. Because passivation quality largely depends on the film immediately grown at the silicon interface, it is a challenge to prevent poor quality native oxide formation before deposition via ALD. All of the samples pre-ALD are given an additional HF dip step for 5 minutes after SC2 during RCA cleaning to strip any native oxide and also leave the surface with hydrogen termination which should prevent native oxidation for a short duration. Unfortunately, due to wafer rinsing and drying requirements in the cleanroom facilities, the minimum time post HF dip to ALD chamber is ~10 min. It is possible that some native oxide forms in this time which results in the lower lifetimes measured. However, ALD may still hold potential for forming well passivating thin films based on the high quality passivation of Si via ALD that is common in industrial cleanroom facilities.

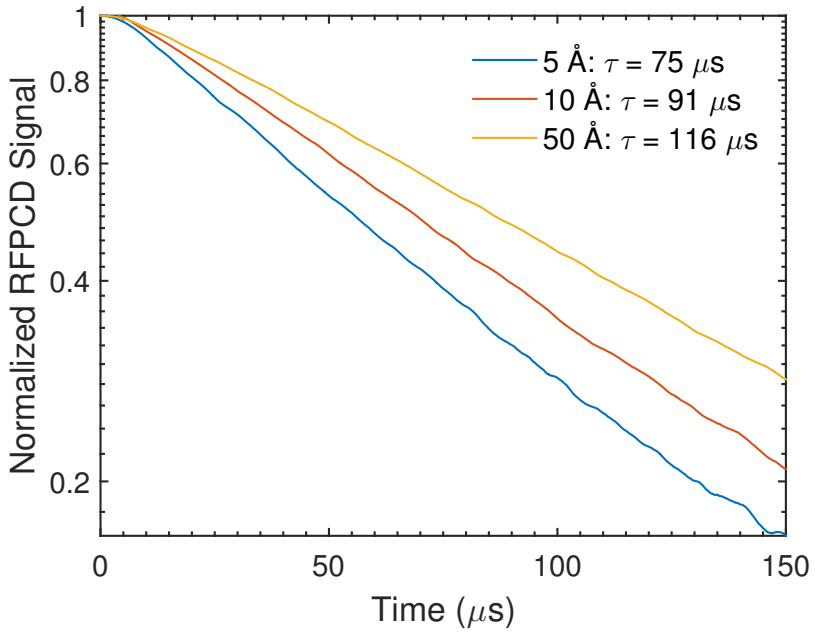

Figure 6-19: Effective carrier lifetimes measured via RFPCD for films deposited by ALD for varying film thicknesses.

6.6 Triplet Energy Transfer to Silicon

6.6.1 Magnetic Field Effect (MFE) Photoluminescence

Thermally evaporated films of tetracene 20 nm thick were deposited on the various oxide films fabricated in the previous section (Section 6.5). The methodology described in Section 6.4 was then used to determine if any triplet states contribute to Si photoluminescence and are therefore transferring their energy to Si. Control measurements of bare silicon without tetracene do not show any dependence of PL on applied magnetic field. In addition, measurements of samples with sufficiently thick oxides such that no non-radiative energy transfer is expected (fabricated by both dry oxidation and ALD) show no evidence of magnetic field dependent PL. Figure 6-20 shows a plot of the PL signal change percent as a function of applied magnetic field for samples with tetracene on ALD deposited SiO_2 films. The thickest film (50 Å) shows variations in the signal close to 0 % on the order of the experimental noise indicating that no triplet transfer is occurring. However, there is a clear decrease in PL from the thinner oxide films (5 Å and 10 Å) as magnetic field is decreasing. The magnetic field is decreasing the singlet fission rate and thus altering the population of triplet states in tetracene. Therefore, this decrease in PL signal shows the first clear evidence that transfer of triplet state energy directly into silicon is possible. Furthermore, our observations show a clear dependence of the signal change magnitude on the separation distance (oxide thickness) as expected. Lack of observation of PL signal change from 50 Å films is also consistent with our model (Section 6.5) which predicts that transfer is quickly quenched by a couple nanometers of oxide.

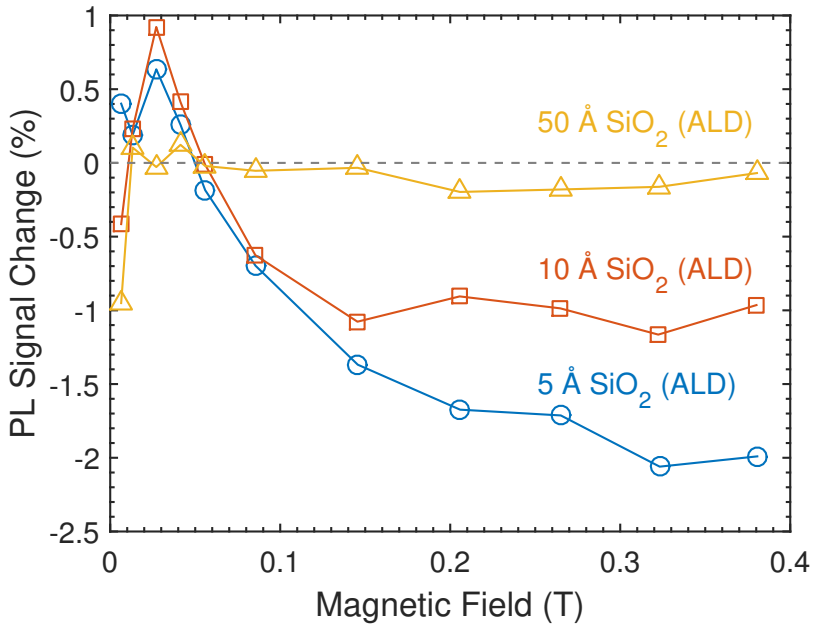

Figure 6-20: Magnetic Field Effect (MFE) PL from ALD passivated samples showing transfer of triplet energy into Si.

The signal in MFE PL measurements are obtained by filtering out visible light (to remove signal from singlet fluorescence) and integration of the near-IR spectra to as collect as much silicon emission as possible due it being an indirect material and thus a poor emitter. In order to verify that the observed PL signal always originates in silicon and that MFE PL is not a result of triplet phosphorescence (unlikely due to low probability), PL spectra were obtained for samples with and without tetracene. Figure 6-21 shows that the spectra are reasonably well matched indicating that our measurements are only probing silicon emission and that the MFE changes observed are indeed due to transfer of triplet energy to silicon.

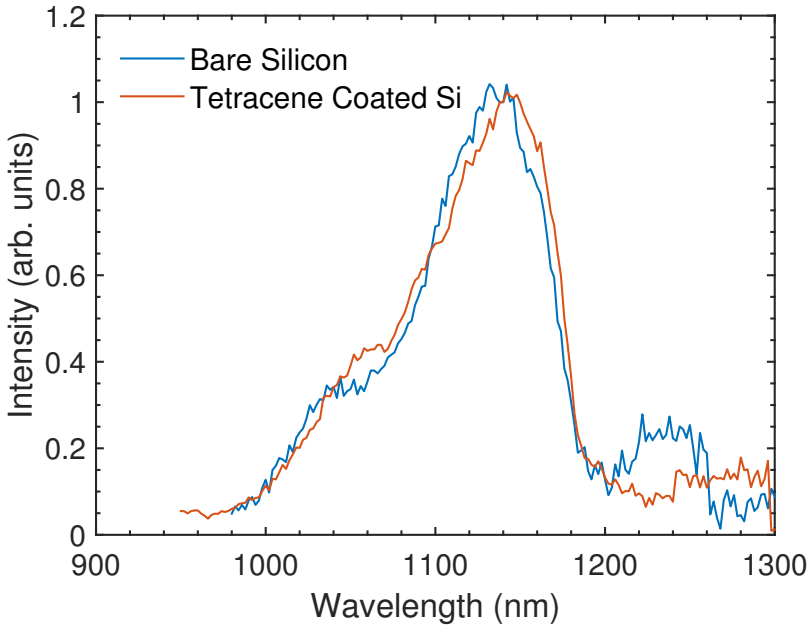

Figure 6-21: Photoluminescence spectra comparison show that emission from tetracene coated Si matches that of bare Si.

Similar MFE results are obtained from samples fabricated via dry oxidation. No MFE was observed for samples with oxides thicker than 19 Å. Unfortunately, this means we have yet to develop a film thin enough for transfer while maintaining the surface passivation quality expected from dry oxidation. While we have shown evidence of transfer, further improvement of the surface quality from very thin films will likely be required for useful solar cell efficiency increases (discussed more in Section 6.2). The two thinner dry oxide samples (E and F) showed weak MFE PL changes approximately an order of magnitude lower percent change in signal compared to ALD samples. The decrease in signal is mostly likely due to the slightly larger thicknesses of the dry oxide samples.

6.6.2 Changes in Generation Rate Measured by RFPCD

To verify the methodology described in Section 6.3.1, generation rates were measured via RFPCD for samples with and without tetracene containing sufficiently thick (50 nm and

100 nm) that no non-radiative energy transfer is expected from tetracene to silicon. Figure 6-22 contains a plot of the generation rate ratios for samples with 20 nm thick tetracene films to without tetracene under optical excitation at 850 nm and 470 nm. Because tetracene does not absorb the excitation and should not affect the reflectivity much for a 20 nm film, under 850 nm excitation, the generation rate with and without tetracene should be identical and the generation rate ratio should be equal to 1 as observed (with a few percent error). Under 470 nm excitation, the tetracene should absorb 14 % of the light in 20 nm based on an a measured absorption coefficient of 7.5×10^4 cm^{-1} assuming a single optical pass. Therefore we expect the generation rate ratio to be ~0.86 with tetracene if no transfer is occurring. We also see this to within a few percent confirming that our measurements are consistent with expectations when energy transfer is absent. The discrepancy may be related to scattering of light by tetracene or changes to the effective path absorption path length in tetracene due to destructive interference (created by reflections off the various interfaces present).

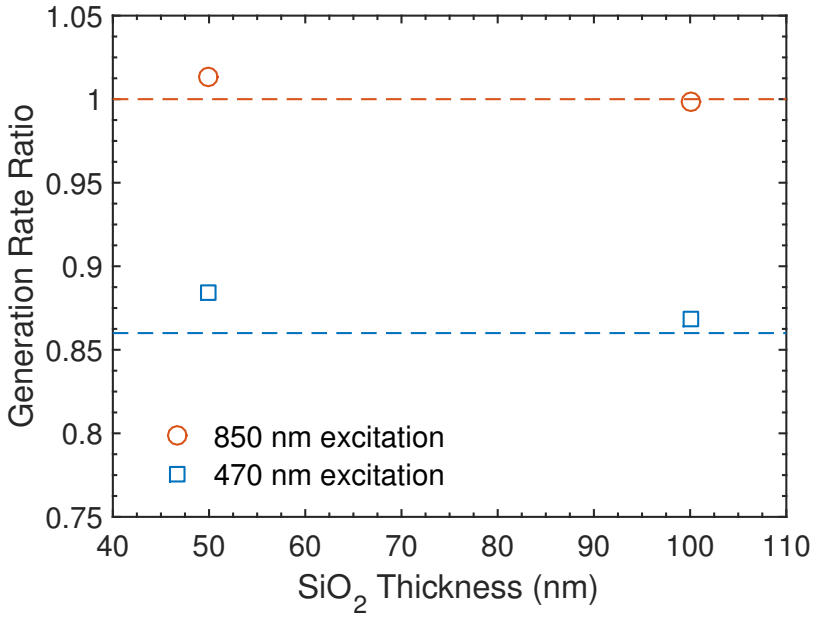

Figure 6-22: Generation rate ratios measured by RFPCD for thick dry oxides.

Because the RFPCD signal is proportional to the lifetime, the signal/noise of our measurements is dependent on the quality of the surface. Accurate determination of generation rate ratios from RFPCD measurements of the samples with thin ALD oxides are made difficult due to their poor lifetimes. At the present moment, an average of multiple RFPCD measurements show indications that energy is transferred from tetracene to silicon when the oxide thickness is small (consistent with MFE measurements). However, individual measurements show considerable spread making it difficult to quantitatively determine the amount of energy absorbed by tetracene which has been transfered silicon. We have made calibration measurements to determine that the sensitivity of differences in generation rate is quite good when the effective lifetime is >1 ms, especially when combined with corrections via reflectivity measurements. Therefore, in the future, if better passivation

can be achieved for films thin enough to allow energy transfer, our developed methodology can potentially be quite useful for providing a quick measurement of energy transfer yields.

6.7 Future Work

In this chapter, we have demonstrated that triplet state energy can transfer into silicon via MFE PL measurements. While this measurement links triplets to emission in silicon, therby showing transfer of energy into silicon, it has yet to be experimentally verified that the energy transferred to silicon can be electrically collected. Therefore, future experiments on observing MFE modulated photocurrent should be performed. For experimental simplicity, transfer can be shown using relatively easy to fabricate photoconductor or MSM photodiode devices. Eventually, direct measurement of transfer yields and efficiency gains can be made from tetracene on Si solar cell devices.

However, based on the simulations and calculations made in this work, that first requires improving passivation of the surface via ultra thin films (<2 nm). As previously mentioned, ALD processing of films in our university cleanroom setting was not ideal for passivating Si. Some improvements may be gained from investigating if annealing can be used to decrease SRV but it may be tricky to avoid further oxide growth at elevated temperatures. An alternative would be to investigate other facilities which may be capable of supplying thin films with satisfactory passivation.

Well passivating thin films would then allow for quantitative measurement of transfer yields through RFPCD (and perhaps devices). Furthermore, the dependence of transfer on various parameters could be used to gain more understanding about the transfer mechanism. Film thickness and composition could be changed to see how transfer is affected by distance, dielectric constant, barrier height, oxide charges, etc. We have seen experimental evidence of triplet transfer, thereby identifying new physics phenomena which are not understood with current models. While we have investigated triplet transfer for photovoltaic applications, understanding the physics behind the transfer mechanism could potentially lead to uses for hybrid organic-inorganic semiconductor systems in new applications.

Chapter 7

Summary

The overall goal of this thesis was to study defects (bulk and interface) in Ge and Si with a focus on understanding the impact that generation and recombination at bandgap states will have on optoelectronic applications.

Point Defects in Germanium

In Chapter 3, a fundamental study of point defects was performed to characterize defect states in Sb-doped Ge. Defect states were introduced by controlled irradiation from a variety of sources (gamma, alpha, and neutron) and full characterization of their electronic properties were presented (previous studies have only reported apparent enthalpies and capture cross sections for most defect states). This knowledge is important for quantitative determination the effect of defects on device performance. In addition, a thorough annealing study of the defects generated by ^{60}Co was performed. From analysis of the irradiation source energies, we predict that ^{60}Co irradiation only produces homogenously distributed single displacements. Compared to studies utilizing higher mass particle irradiation sources, we generate a much simpler primary defect profile. This simple scenario allows for greater understanding of the interactions between defect states enabling us to draw some significant conclusions. We determined which primary defect (vacancy or interstitial) is a component of the observed defect states. We determined that the introduction rate of uncorrelated vacancies and interstitials due to ^{60}Co irradiation is $\sim 2 \times 10^{11}$ cm^{-3} Mrad^{-1}. We determined that the Sb-V associated decays by dissociation and diffusion of the vacancy to sinks in the bulk. The activation energy of decay was used to make estimates for the mono-vacancy migration energy in Ge. Also, the observation of a greater than one conversion rate of defect states has lead to the conclusion that secondary formation of defects in Ge occurs and that E_{22} contains multiple interstitials. Because we have determined which defect states are generated by isolated frenkel pairs, the work stemming from ^{60}Co irradiation will form the backbone for future studies using higher mass particle irradiation sources which generate more complex defect associates related to damage cascades.

Ge-on-Si Laser

In Chapter 4, the experimental apparatus and testing parameters needed for characterization of emission from electrically injected Ge diodes were developed. This allowed for the first demonstration of electrically pumped lasing from Ge epitaxially grown on Si. In addition, lasing was observed over a ~200 nm bandwidth showing that this system holds promise for low-cost on-chip communications applications via silicon microphotonics. The observed large threshold currents were determined to be largely a result of recombination due to threading dislocations. We determined that recombination by threading dislocations becomes negligible when TDD $\approx 4 \times 10^6$ cm^{-2}.

Colloidal Quantum Dot Chalcogenide Glass Films

In Chapter 5, we developed a process for incorporation of colloidal quantum dots into a ChG matrix via solution based processing in common solvents. Observation of PL comparable to QD/PMMA films shows potential for this material to form the basis for low cost light sources which can be integrated with ChG microphotonic systems. Initial attempts using organic ligands resulted in films containing large QD aggregates. For many potential applications, these aggregates would be larger than the device size. More uniformly dispersed films were obtained by replacement of organic ligands with inorganic ligands.

Triplet Energy Transfer To Silicon

In Chapter 6, we investigated how surface recombination affects potential solar cell efficiency gains obtained by transfer of exciton energy from a singlet fission material (tetracene) to silicon. This system can potentially increase the photocurrent from high energy photons in Si solar cells with minimal additional processing and cost. However, because transfer effectively places carriers closer to a surface which mediates recombination, the overall gain from addition of tetracene not immediately apparent and will be dependent on the quality of the interface. Our simulations show that for practical efficiency gains, SRVs for the tetracene/silicon interface must be no greater than 10^4 cm s^{-1}. Characterization via RFPCD showed that tetracene does not provide a sufficient level of passivation thus requiring the use of an intermediate layer which passivates the Si surface. A simple model was proposed that estimates the barrier thickness must be <2 nm (for SiO_2) for efficient transfer of triplet states into Si. Using dry oxidation, well passivated surfaces were obtained but only for thicknesses too large to show detectable triplet transfer. Using thinner films fabricated by ALD, we showed the first direct evidence of triplet energy transfer to Si via MFE PL measurements. A methodology for obtaining triplet transfer yields via RFPCD was also developed.

Bibliography

[1] D. A. B. Miller, "Optical interconnects to electronic chips", *Applied Optics*, vol. 49, no. 25, F59, Sep. 1, 2010. DOI: 10.1364/AO.49.000F59.

[2] R. Kirchain and L. Kimerling, "A roadmap for nanophotonics", *Nature Photonics*, vol. 1, no. 6, pp. 303–305, Jun. 2007. DOI: 10.1038/nphoton.2007.84.

[3] A.-J. Lim, J. Song, Q. Fang, C. Li, X. Tu, N. Duan, K. K. Chen, R.-C. Tern, and T.-Y. Liow, "Review of Silicon Photonics Foundry Efforts", *IEEE Journal of Selected Topics in Quantum Electronics*, vol. 20, no. 4, pp. 405–416, Jul. 2014. DOI: 10.1109/JSTQE.2013.2293274.

[4] M. R. Watts, M. J. Shaw, and G. N. Nielson, "Optical resonators: Microphotonic thermal imaging", *Nature Photonics*, vol. 1, no. 11, pp. 632–634, Nov. 2007. DOI: 10.1038/nphoton.2007.219.

[5] V. Singh, P. T. Lin, N. Patel, H. Lin, L. Li, Y. Zou, F. Deng, C. Ni, J. Hu, J. Giammarco, A. P. Soliani, B. Zdyrko, I. Luzinov, S. Novak, J. Novak, P. Wachtel, S. Danto, J. D. Musgraves, K. Richardson, L. C. Kimerling, and A. M. Agarwal, "Mid-infrared materials and devices on a Si platform for optical sensing", *Science and Technology of Advanced Materials*, vol. 15, no. 1, p. 014 603, Feb. 1, 2014. DOI: 10.1088/1468-6996/15/1/014603.

[6] W. Shockley and W. T. Read, "Statistics of the Recombinations of Holes and Electrons", *Physical Review*, vol. 87, no. 5, pp. 835–842, Sep. 1, 1952. DOI: 10.1103/PhysRev.87.835.

[7] R. N. Hall, "Electron-Hole Recombination in Germanium", *Physical Review*, vol. 87, no. 2, pp. 387–387, Jul. 15, 1952. DOI: 10.1103/PhysRev.87.387.

[8] R. Hall, "Recombination processes in semiconductors", *Proceedings of the IEE - Part B: Electronic and Communication Engineering*, vol. 106, no. 17, pp. 923–931, May 1959. DOI: 10.1049/pi-b-2.1959.0171.

[9] D. A. Drabold and S. K. Estreicher, "Defect Theory: An Armchair History", in *Theory of Defects in Semiconductors*, ser. Topics in Applied Physics 104, D. A. Drabold and S. K. Estreicher, Eds., Springer Berlin Heidelberg, 2007, pp. 11–28. DOI: 10.1007/11690320_2.

[10] P. Blood and J. W. Orton, *The Electrical Characterization of Semiconductors: Majority Carriers and Electron States*, ser. Techniques of physics: 14. Academic Press, 1992.

[11] D. B. Holt and B. G. Yacobi, *Extended Defects in Semiconductors: ELECTRONIC PROPERTIES, Device Effects and Structures*, 1 edition. London; New York: Cambridge University Press, Apr. 9, 2007, 644 pp.

[12] D. V. Lang, "Recombination-Enhanced Reactions in Semiconductors", *Annual Review of Materials Science*, vol. 12, no. 1, pp. 377–398, 1982. DOI: 10.1146/annurev.ms.12.080182.002113.

[13] R. G. Waters, "Diode laser degradation mechanisms: A review", *Progress in Quantum Electronics*, vol. 15, no. 3, pp. 153–174, Jan. 1, 1991. DOI: 10.1016/0079-6727(91)90004-2.

[14] E. A. Fitzgerald, "Dislocations in strained-layer epitaxy: Theory, experiment, and applications", *Materials Science Reports*, vol. 7, no. 3, pp. 87–142, Nov. 1, 1991. DOI: 10.1016/0920-2307(91)90006-9.

[15] K. L. Luke and L.-J. Cheng, "Analysis of the interaction of a laser pulse with a silicon wafer: Determination of bulk lifetime and surface recombination velocity", *Journal of Applied Physics*, vol. 61, no. 6, pp. 2282–2293, Mar. 15, 1987. DOI: 10.1063/1.337938.

[16] N. S. Patel, C. Monmeyran, A. Agarwal, and L. C. Kimerling, "Point defect states in Sb-doped germanium", *Journal of Applied Physics*, vol. 118, no. 15, p. 155 702, Oct. 21, 2015. DOI: 10.1063/1.4933384.

[17] J. Michel, J. Liu, and L. C. Kimerling, "High-performance Ge-on-Si photodetectors", *Nature Photonics*, vol. 4, no. 8, pp. 527–534, Aug. 2010. DOI: 10.1038/nphoton.2010.157.

[18] D. Ahn, C.-y. Hong, J. Liu, W. Giziewicz, M. Beals, L. C. Kimerling, J. Michel, J. Chen, and F. X. Kärtner, "High performance, waveguide integrated Ge photodetectors", *Optics Express*, vol. 15, no. 7, pp. 3916–3921, Apr. 2, 2007. DOI: 10.1364/OE.15.003916.

[19] Y.-H. Kuo, Y. K. Lee, Y. Ge, S. Ren, J. E. Roth, T. I. Kamins, D. A. B. Miller, and J. S. Harris, "Strong quantum-confined Stark effect in germanium quantum-well structures on silicon", *Nature*, vol. 437, no. 7063, pp. 1334–1336, Oct. 27, 2005. DOI: 10.1038/nature04204.

[20] J. E. Roth, O. Fidaner, R. K. Schaevitz, Y.-H. Kuo, T. I. Kamins, J. S. Harris, and D. A. B. Miller, "Optical modulator on silicon employing germanium quantum wells", *Optics Express*, vol. 15, no. 9, pp. 5851–5859, Apr. 30, 2007. DOI: 10.1364/OE.15.005851.

[21] J. Liu, M. Beals, A. Pomerene, S. Bernardis, R. Sun, J. Cheng, L. C. Kimerling, and J. Michel, "Waveguide-integrated, ultralow-energy GeSi electro-absorption modulators", *Nature Photonics*, vol. 2, no. 7, pp. 433–437, Jul. 2008. DOI: 10.1038/nphoton.2008.99.

[22] R. J. Elliott, "Theory of the Effect of Spin-Orbit Coupling on Magnetic Resonance in Some Semiconductors", *Physical Review*, vol. 96, no. 2, pp. 266–279, Oct. 15, 1954. DOI: 10.1103/PhysRev.96.266.

[23] G. W. Ludwig and H. H. Woodbury, "Electron Spin Resonance in Semiconductors", in *Solid State Physics*, vol. 13, 1962.

[24] A. Mesli and A. Nylandsted Larsen, "Irradiation induced defects in Si1=xGex: The effect of alloying", *Nuclear Instruments and Methods in Physics Research Section B: Beam Interactions with Materials and Atoms*, vol. 211, no. 1, pp. 80–90, Sep. 2003. DOI: 10.1016/S0168-583X(03)01167-4.

[25] N. Fukuoka and H. Saito, "Radiation Defects in n-Type Germanium Studied by Deep Level Transient Spectroscopy", *Japanese Journal of Applied Physics*, vol. 20, no. 7, p. L519, Jul. 1, 1981. DOI: 10.1143/JJAP.20.L519.

[26] N. Fukuoka and H. Saito, "Defect States in n-Type Germanium Irradiated with 1.5 MeV Electrons", *Japanese Journal of Applied Physics*, vol. 21, no. 6R, p. 930, Jun. 1, 1982. DOI: 10.1143/JJAP.21.930.

[27] F. Poulin and J. C. Bourgoin, "Characteristics of the electron traps produced by electron irradiation in n-type germanium", *Physical Review B*, vol. 26, no. 12, pp. 6788–6794, Dec. 15, 1982. DOI: 10.1103/PhysRevB.26.6788.

[28] P. M. Mooney, F. Poulin, and J. C. Bourgoin, "Annealing of electron-induced defects in n-type germanium", *Physical Review B*, vol. 28, no. 6, pp. 3372–3377, Sep. 15, 1983. DOI: 10.1103/PhysRevB.28.3372.

[29] V. Nagesh and J. W. Farmer, "Study of irradiation-induced defects in germanium", *Journal of Applied Physics*, vol. 63, no. 5, pp. 1549–1553, Mar. 1, 1988. DOI: 10.1063/1.339939.

[30] J. Fage-Pedersen, A. N. Larsen, and A. Mesli, "Irradiation-induced defects in Ge studied by transient spectroscopies", *Physical Review B*, vol. 62, no. 15, pp. 10 116–10 125, Oct. 15, 2000. DOI: 10.1103/PhysRevB.62.10116.

[31] V. P. Markevich, I. D. Hawkins, A. R. Peaker, K. V. Emtsev, V. V. Emtsev, V. V. Litvinov, L. I. Murin, and L. Dobaczewski, "Vacancy-group-V-impurity atom pairs in Ge crystals doped with P, As, Sb, and Bi", *Physical Review B*, vol. 70, no. 23, p. 235 213, Dec. 27, 2004. DOI: 10.1103/PhysRevB.70.235213.

[32] V. P. Markevich, A. R. Peaker, V. V. Litvinov, V. V. Emtsev, and L. I. Murin, "Electronic properties of antimony-vacancy complex in Ge crystals", *Journal of Applied Physics*, vol. 95, no. 8, pp. 4078–4083, Apr. 15, 2004. DOI: 10.1063/1.1669059.

[33] F. D. Auret, W. E. Meyer, S. Coelho, and M. Hayes, "Electrical characterization of defects introduced during electron beam deposition of Pd Schottky contacts on n-type Ge", *Applied Physics Letters*, vol. 88, no. 24, p. 242 110, Jun. 12, 2006. DOI: 10.1063/1.2213203.

[34] D. V. Lang, "Deep-level transient spectroscopy: A new method to characterize traps in semiconductors", *Journal of Applied Physics*, vol. 45, no. 7, pp. 3023–3032, Jul. 1, 1974. DOI: 10.1063/1.1663719.

[35] G. L. Miller, D. V. Lang, and L. C. Kimerling, "Capacitance Transient Spectroscopy", *Annual Review of Materials Science*, vol. 7, no. 1, pp. 377–448, 1977. DOI: 10.1146/annurev.ms.07.080177.002113.

[36] L. Dobaczewski, A. R. Peaker, and K. B. Nielsen, "Laplace-transform deep-level spectroscopy: The technique and its applications to the study of point defects in semiconductors", *Journal of Applied Physics*, vol. 96, no. 9, pp. 4689–4728, Nov. 1, 2004. DOI: 10.1063/1.1794897.

[37] L. C. Kimerling, "Influence of deep traps on the measurement of free-carrier distributions in semiconductors by junction capacitance techniques", *Journal of Applied Physics*, vol. 45, no. 4, pp. 1839–1845, Apr. 1, 1974. DOI: 10.1063/1.1663500.

[38] J. Srour, C. Marshall, and P. Marshall, "Review of displacement damage effects in silicon devices", *IEEE Transactions on Nuclear Science*, vol. 50, no. 3, pp. 653–670, Jun. 2003. DOI: 10.1109/TNS.2003.813197.

[39] J. O. Stiegler and L. K. Mansur, "Radiation Effects in Structural Materials", *Annual Review of Materials Science*, vol. 9, no. 1, pp. 405–454, 1979. DOI: 10.1146/annurev.ms.09.080179.002201.

[40] O. Klein and Y. Nishina, "Über die Streuung von Strahlung durch freie Elektronen nach der neuen relativistischen Quantendynamik von Dirac", *Zeitschrift für Physik*, vol. 52, no. 11-12, pp. 853–868, 1929. DOI: 10.1007/BF01366453.

[41] E. Holmström, K. Nordlund, and A. Kuronen, "Threshold defect production in germanium determined by density functional theory molecular dynamics simulations", *Physica Scripta*, vol. 81, no. 3, p. 035 601, Mar. 1, 2010. DOI: 10.1088/0031-8949/81/03/035601.

[42] G. H. Kinchin and R. S. Pease, "The Displacement of Atoms in Solids by Radiation", *Reports on Progress in Physics*, vol. 18, no. 1, p. 1, Jan. 1, 1955. DOI: 10.1088/0034-4885/18/1/301.

[43] C. H. Henry and D. V. Lang, "Nonradiative capture and recombination by multiphonon emission in GaAs and GaP", *Physical Review B*, vol. 15, no. 2, pp. 989–1016, Jan. 15, 1977. DOI: 10.1103/PhysRevB.15.989.

[44] A. Mesli, L. Dobaczewski, K. B. Nielsen, V. Kolkovsky, M. C. Petersen, and A. N. Larsen, "Low-temperature irradiation-induced defects in germanium: In situ analysis", *Physical Review B*, vol. 78, no. 16, p. 165 202, Oct. 8, 2008. DOI: 10.1103/PhysRevB.78.165202.

[45] V. Kolkovsky, M. C. Petersen, A. Mesli, J. Van Gheluwe, P. Clauws, and A. N. Larsen, "Gallium interstitial in irradiated germanium: Deep level transient spectroscopy", *Physical Review B*, vol. 78, no. 23, p. 233 201, Dec. 11, 2008. DOI: 10.1103/PhysRevB.78.233201.

[46] F. D. Auret, P. J. J. van Rensburg, M. Hayes, J. M. Nel, W. E. Meyer, S. Decoster, V. Matias, and A. Vantomme, "Electrical characterization of defects introduced in n-type Ge during indium implantation", *Applied Physics Letters*, vol. 89, no. 15, p. 152 123, Oct. 9, 2006. DOI: 10.1063/1.2360922.

[47] S. Brotzmann and H. Bracht, "Intrinsic and extrinsic diffusion of phosphorus, arsenic, and antimony in germanium", *Journal of Applied Physics*, vol. 103, no. 3, p. 033 508, Feb. 1, 2008. DOI: 10.1063/1.2837103.

[48] J. R. Weber, A. Janotti, and C. G. Van de Walle, "Dangling bonds and vacancies in germanium", *Physical Review B*, vol. 87, no. 3, p. 035 203, Jan. 14, 2013. DOI: 10.1103/PhysRevB.87.035203.

[49] K. T. Roro, P. J. Janse van Rensburg, F. D. Auret, and S. Coelho, "Effect of alpha-particle irradiation on the electrical properties of n-type Ge", *Physica B: Condensed Matter*, Proceedings of the Third South African Conference on Photonic Materials, vol. 404, no. 22, pp. 4496–4498, Dec. 1, 2009. DOI: 10.1016/j.physb.2009.09.033.

[50] A. Carvalho, R. Jones, C. Janke, J. P. Goss, P. R. Briddon, J. Coutinho, and S. Öberg, "Self-Interstitial in Germanium", *Physical Review Letters*, vol. 99, no. 17, p. 175 502, Oct. 26, 2007. DOI: 10.1103/PhysRevLett.99.175502.

[51] R. I. Scace and G. A. Slack, "Solubility of Carbon in Silicon and Germanium", *The Journal of Chemical Physics*, vol. 30, no. 6, pp. 1551–1555, Jun. 1, 1959. DOI: 10.1063/1.1730236.

[52] M. Naganawa, Y. Shimizu, M. Uematsu, K. M. Itoh, K. Sawano, Y. Shiraki, and E. E. Haller, "Charge states of vacancies in germanium investigated by simultaneous observation of germanium self-diffusion and arsenic diffusion", *Applied Physics Letters*, vol. 93, no. 19, p. 191 905, Nov. 10, 2008. DOI: 10.1063/1.3025892.

[53] S. Brotzmann, H. Bracht, J. L. Hansen, A. N. Larsen, E. Simoen, E. E. Haller, J. S. Christensen, and P. Werner, "Diffusion and defect reactions between donors, C, and vacancies in Ge. I. Experimental results", *Physical Review B*, vol. 77, no. 23, p. 235 207, Jun. 16, 2008. DOI: 10.1103/PhysRevB.77.235207.

[54] T. R. Waite, "Theoretical Treatment of the Kinetics of Diffusion-Limited Reactions", *Physical Review*, vol. 107, no. 2, pp. 463–470, Jul. 15, 1957. DOI: 10.1103/PhysRev.107.463.

[55] W. S. Snyder and J. Neufeld, "Disordering of Solids by Neutron Radiation", *Physical Review*, vol. 97, no. 6, pp. 1636–1646, Mar. 15, 1955. DOI: 10.1103/PhysRev.97.1636.

[56] J. F. Ziegler, M. D. Ziegler, and J. P. Biersack, "SRIM – The stopping and range of ions in matter (2010)", *Nuclear Instruments and Methods in Physics Research Section B: Beam Interactions with Materials and Atoms*, 19th International Conference on Ion Beam Analysis, vol. 268, no. 11–12, pp. 1818–1823, Jun. 2010. DOI: 10.1016/j.nimb.2010.02.091.

[57] R. E. Camacho-Aguilera, Y. Cai, N. Patel, J. T. Bessette, M. Romagnoli, L. C. Kimerling, and J. Michel, "An electrically pumped germanium laser", *Optics Express*, vol. 20, no. 10, pp. 11 316–11 320, May 7, 2012. DOI: 10.1364/OE.20.011316.

[58] G. E. Moore, "Cramming more components onto integrated circuits", *Electronics*, vol. 38, pp. 114–116, 1965.

[59] M. M. Waldrop, "The chips are down for Moore's law", *Nature*, vol. 530, no. 7589, pp. 144–147, Feb. 9, 2016. DOI: 10.1038/530144a.

[60] J. Cardenas, C. B. Poitras, J. T. Robinson, K. Preston, L. Chen, and M. Lipson, "Low loss etchless silicon photonic waveguides", *Optics Express*, vol. 17, no. 6, p. 4752, Mar. 16, 2009. DOI: 10.1364/OE.17.004752.

[61] D. Liang and J. E. Bowers, "Recent progress in lasers on silicon", *Nature Photonics*, vol. 4, no. 8, pp. 511–517, Aug. 2010. DOI: 10.1038/nphoton.2010.167.

[62] H. Rong, R. Jones, A. Liu, O. Cohen, D. Hak, A. Fang, and M. Paniccia, "A continuous-wave Raman silicon laser", *Nature*, vol. 433, no. 7027, pp. 725–728, Feb. 17, 2005. DOI: 10.1038/nature03346.

[63] H. Rong, S. Xu, Y.-H. Kuo, V. Sih, O. Cohen, O. Raday, and M. Paniccia, "Low-threshold continuous-wave Raman silicon laser", *Nature Photonics*, vol. 1, no. 4, pp. 232–237, Apr. 2007. DOI: 10.1038/nphoton.2007.29.

[64] R. J. Walters, G. I. Bourianoff, and H. A. Atwater, "Field-effect electroluminescence in silicon nanocrystals", *Nature Materials*, vol. 4, no. 2, pp. 143–146, Feb. 2005. DOI: 10.1038/nmat1307.

[65] M. Pollnau, "Rare-Earth-Ion-Doped Channel Waveguide Lasers on Silicon", *IEEE Journal of Selected Topics in Quantum Electronics*, vol. 21, no. 1, pp. 414–425, Jan. 2015. DOI: 10.1109/JSTQE.2014.2351811.

[66] M. E. Groenert, C. W. Leitz, A. J. Pitera, V. Yang, H. Lee, R. J. Ram, and E. A. Fitzgerald, "Monolithic integration of room-temperature cw GaAs/AlGaAs lasers on Si substrates via relaxed graded GeSi buffer layers", *Journal of Applied Physics*, vol. 93, no. 1, pp. 362–367, Jan. 1, 2003. DOI: 10.1063/1.1525865.

[67] H. Park, A. W. Fang, S. Kodama, and J. E. Bowers, "Hybrid silicon evanescent laser fabricated with a silicon waveguide and III-V offset quantum wells", *Optics Express*, vol. 13, no. 23, p. 9460, 2005. DOI: 10.1364/OPEX.13.009460.

[68] M. J. R. Heck, J. F. Bauters, M. L. Davenport, J. K. Doylend, S. Jain, G. Kurczveil, S. Srinivasan, Y. Tang, and J. E. Bowers, "Hybrid Silicon Photonic Integrated Circuit Technology", *IEEE Journal of Selected Topics in Quantum Electronics*, vol. 19, no. 4, pp. 6 100 117–6 100 117, Jul. 2013. DOI: 10.1109/JSTQE.2012.2235413.

[69] G. W. Read, I. P. Marko, N. Hossain, and S. J. Sweeney, "Physical Properties and Characteristics of III-V Lasers on Silicon", *IEEE Journal of Selected Topics in Quantum Electronics*, vol. 21, no. 6, pp. 377–384, Nov. 2015. DOI: 10.1109/JSTQE.2015.2424923.

[70] H. Kroemer, "A proposed class of hetero-junction injection lasers", *Proceedings of the IEEE*, vol. 51, no. 12, pp. 1782–1783, Dec. 1963. DOI: 10.1109/PROC.1963.2706.

[71] J. Liu, X. Sun, L. C. Kimerling, and J. Michel, "Direct-gap optical gain of Ge on Si at room temperature", *Optics Letters*, vol. 34, no. 11, p. 1738, Jun. 1, 2009. DOI: 10.1364/OL.34.001738.

[72] J. Liu, X. Sun, D. Pan, X. Wang, L. C. Kimerling, T. L. Koch, and J. Michel, "Tensile-strained, n-type Ge as a gain medium for monolithic laser integration on Si", *Optics Express*, vol. 15, no. 18, p. 11 272, 2007. DOI: 10.1364/OE.15.011272.

[73] J. Liu, R. Camacho-Aguilera, J. T. Bessette, X. Sun, X. Wang, Y. Cai, L. C. Kimerling, and J. Michel, "Ge-on-Si optoelectronics", *Thin Solid Films*, ICSI-7, vol. 520, no. 8, pp. 3354–3360, Feb. 1, 2012. DOI: 10.1016/j.tsf.2011.10.121.

[74] R. E. Camacho-Aguilera, "Ge-on-Si Laser for Silicon Photonics", Thesis, Massachusetts Institute of Technology, 2013.

[75] Y. Cai, "Materials Science and Design for Germanium Monolithic Light Source on Silicon", Thesis, Massachusetts Institute of Technology, 2014.

[76] E. A. Fitzgerald, Y.-H. Xie, M. L. Green, D. Brasen, A. R. Kortan, J. Michel, Y.-J. Mii, and B. E. Weir, "Totally relaxed GexSi1=x layers with low threading dislocation densities grown on Si substrates", *Applied Physics Letters*, vol. 59, no. 7, pp. 811–813, Aug. 12, 1991. DOI: 10.1063/1.105351.

[77] H.-C. Luan, D. R. Lim, K. K. Lee, K. M. Chen, J. G. Sandland, K. Wada, and L. C. Kimerling, "High-quality Ge epilayers on Si with low threading-dislocation densities", *Applied Physics Letters*, vol. 75, no. 19, pp. 2909–2911, Nov. 8, 1999. DOI: 10.1063/1.125187.

[78] J. Liu, X. Sun, R. Camacho-Aguilera, L. C. Kimerling, and J. Michel, "Ge-on-Si laser operating at room temperature", *Optics Letters*, vol. 35, no. 5, p. 679, Mar. 1, 2010. DOI: 10.1364/OL.35.000679.

[79] X. Sun, J. Liu, L. C. Kimerling, and J. Michel, "Toward a Germanium Laser for Integrated Silicon Photonics", *IEEE Journal of Selected Topics in Quantum Electronics*, vol. 16, no. 1, pp. 124–131, Jan. 2010. DOI: 10.1109/JSTQE.2009.2027445.

[80] J. Liu, "Monolithically Integrated Ge-on-Si Active Photonics", *Photonics*, vol. 1, no. 3, pp. 162–197, Jul. 2, 2014. DOI: 10.3390/photonics1030162.

[81] J. M. Hartmann, J. P. Barnes, M. Veillerot, J. M. Fédéli, Q. Benoit A La Guillaume, and V. Calvo, "Structural, electrical and optical properties of in-situ phosphorous-doped Ge layers", *Journal of Crystal Growth*, vol. 347, no. 1, pp. 37–44, May 15, 2012. DOI: 10.1016/j.jcrysgro.2012.03.023.

[82] R. E. Camacho-Aguilera, Y. Cai, J. T. Bessette, L. C. Kimerling, and J. Michel, "High active carrier concentration in n-type, thin film Ge using delta-doping", *Optical Materials Express*, vol. 2, no. 11, p. 1462, Nov. 1, 2012. DOI: 10.1364/OME.2.001462.

[83] Y. Cai, R. Camacho-Aguilera, J. T. Bessette, L. C. Kimerling, and J. Michel, "High phosphorous doped germanium: Dopant diffusion and modeling", *Journal of Applied Physics*, vol. 112, no. 3, p. 034 509, Aug. 1, 2012. DOI: 10.1063/1.4745020.

[84] Z. Alferov, "Double heterostructure lasers: Early days and future perspectives", *IEEE Journal of Selected Topics in Quantum Electronics*, vol. 6, no. 6, pp. 832–840, Nov. 2000. DOI: 10.1109/2944.902131.

[85] R. Camacho-Aguilera, J. Bessette, Y. Cai, L. C. Kimerling, and J. Michel, "Electroluminescence of highly doped Ge pnn diodes for Si integrated lasers", in *2011 8th IEEE International Conference on Group IV Photonics (GFP)*, Sep. 2011, pp. 190–192. DOI: 10.1109/GROUP4.2011.6053759.

[86] Y. Cai, Z. Han, X. Wang, R. E. Camacho-Aguilera, L. C. Kimerling, J. Michel, and J. Liu, "Analysis of Threshold Current Behavior for Bulk and Quantum-Well Germanium Laser Structures", *IEEE Journal of Selected Topics in Quantum Electronics*, vol. 19, no. 4, pp. 1 901 009–1 901 009, Jul. 2013. DOI: 10.1109/JSTQE.2013.2247573.

[87] X. Sun, "Ge-on-Si Light-Emitting Materials and Devices for Silicon Photonics", Thesis, Massachusetts Institute of Technology, 2009.

[88] C. Claeys and E. Simoen, Eds., *Extended Defects in Germanium*, vol. 118, ser. Springer Series in Materials Science, Berlin, Heidelberg: Springer Berlin Heidelberg, 2009.

[89] J. R. Patel and L. R. Testardi, "Electronic effects on dislocation velocities in heavily doped germanium", *Applied Physics Letters*, vol. 30, no. 1, pp. 3–5, Jan. 1, 1977. DOI: 10.1063/1.89204.

[90] Y. Cai, W. Yu, L. C. Kimerling, and J. Michel, "Chemical Mechanical Polishing of Selective Epitaxial Grown Germanium on Silicon", *ECS Journal of Solid State Science and Technology*, vol. 3, no. 2, P5–P9, Jan. 1, 2014. DOI: 10.1149/2.003401jss.

[91] G. Farca, S. I. Shopova, and A. T. Rosenberger, "Cavity-enhanced laser absorption spectroscopy using microresonator whispering-gallery modes", *Optics Express*, vol. 15, no. 25, p. 17 443, 2007. DOI: 10.1364/OE.15.017443.

[92] N. M. Hanumegowda, C. J. Stica, B. C. Patel, I. White, and X. Fan, "Refractometric sensors based on microsphere resonators", *Applied Physics Letters*, vol. 87, no. 20, p. 201 107, Nov. 14, 2005. DOI: 10.1063/1.2132076.

[93] J. Hu, X. Sun, A. Agarwal, and L. C. Kimerling, "Design guidelines for optical resonator biochemical sensors", *Journal of the Optical Society of America B*, vol. 26, no. 5, p. 1032, May 1, 2009. DOI: 10.1364/JOSAB.26.001032.

[94] A. L. Efros, Rosen, and M., "The Electronic Structure of Semiconductor Nanocrystals", *Annual Review of Materials Science*, vol. 30, no. 1, pp. 475–521, 2000. DOI: 10.1146/annurev.matsci.30.1.475.

[95] M. S. Skolnick and D. J. Mowbray, "SELF-ASSEMBLED SEMICONDUCTOR QUANTUM DOTS: Fundamental Physics and Device Applications", *Annual Review of Materials Research*, vol. 34, no. 1, pp. 181–218, 2004. DOI: 10.1146/annurev.matsci.34.082103.133534.

[96] P. Bhattacharya, S. Ghosh, and A. D. Stiff-Roberts, "Quantum Dot Opto-Electronic Devices", *Annual Review of Materials Research*, vol. 34, no. 1, pp. 1–40, 2004. DOI: 10.1146/annurev.matsci.34.040203.111535.

[97] V. M. Ustinov, *Quantum Dot Lasers*. Oxford University Press, 2003.

[98] C. B. Murray, D. J. Norris, and M. G. Bawendi, "Synthesis and characterization of nearly monodisperse CdE (E = sulfur, selenium, tellurium) semiconductor nanocrystallites", *Journal of the American Chemical Society*, vol. 115, no. 19, pp. 8706–8715, Sep. 1, 1993. DOI: 10.1021/ja00072a025.

[99] C. B. Murray, Kagan, C. R., and M. G. Bawendi, "Synthesis and Characterization of Monodisperse Nanocrystals and Close-Packed Nanocrystal Assemblies", *Annual Review of Materials Science*, vol. 30, no. 1, pp. 545–610, 2000. DOI: 10.1146/annurev.matsci.30.1.545.

[100] D. Zherebetskyy, Y. Zhang, M. Salmeron, and L.-W. Wang, "Tolerance of Intrinsic Defects in PbS Quantum Dots", *The Journal of Physical Chemistry Letters*, vol. 6, no. 23, pp. 4711–4716, Dec. 3, 2015. DOI: 10.1021/acs.jpclett.5b02202.

[101] Y. Shirasaki, G. J. Supran, M. G. Bawendi, and V. Bulović, "Emergence of colloidal quantum-dot light-emitting technologies", *Nature Photonics*, vol. 7, no. 1, pp. 13–23, Jan. 2013. DOI: 10.1038/nphoton.2012.328.

[102] J. Kwak, J. Lim, M. Park, S. Lee, K. Char, and C. Lee, "High-Power Genuine Ultraviolet Light-Emitting Diodes Based On Colloidal Nanocrystal Quantum Dots", *Nano Letters*, vol. 15, no. 6, pp. 3793–3799, Jun. 10, 2015. DOI: 10.1021/acs.nanolett.5b00392.

[103] J. M. Pietryga, R. D. Schaller, D. Werder, M. H. Stewart, V. I. Klimov, and J. A. Hollingsworth, "Pushing the Band Gap Envelope: Mid-Infrared Emitting Colloidal PbSe Quantum Dots", *Journal of the American Chemical Society*, vol. 126, no. 38, pp. 11 752–11 753, Sep. 1, 2004. DOI: 10.1021/ja047659f.

[104] S. Keuleyan, J. Kohler, and P. Guyot-Sionnest, "Photoluminescence of Mid-Infrared HgTe Colloidal Quantum Dots", *The Journal of Physical Chemistry C*, vol. 118, no. 5, pp. 2749–2753, Feb. 6, 2014. DOI: 10.1021/jp409061g.

[105] V. I. Klimov and M. G. Bawendi, "Ultrafast Carrier Dynamics, Optical Amplification, and Lasing in Nanocrystal Quantum Dots", *MRS Bulletin*, vol. 26, no. 12, pp. 998–1004, Dec. 2001. DOI: 10.1557/mrs2001.256.

[106] P. T. Snee, Y. Chan, D. G. Nocera, and M. G. Bawendi, "Whispering-Gallery-Mode Lasing from a Semiconductor Nanocrystal/Microsphere Resonator Composite", *Advanced Materials*, vol. 17, no. 9, pp. 1131–1136, May 2, 2005. DOI: 10.1002/adma.200401571.

[107] A. V. Malko, A. A. Mikhailovsky, M. A. Petruska, J. A. Hollingsworth, H. Htoon, M. G. Bawendi, and V. I. Klimov, "From amplified spontaneous emission to microring lasing using nanocrystal quantum dot solids", *Applied Physics Letters*, vol. 81, no. 7, pp. 1303–1305, Aug. 12, 2002. DOI: 10.1063/1.1497708.

[108] S. Hoogland, V. Sukhovatkin, I. Howard, S. Cauchi, L. Levina, and E. H. Sargent, "A solution-processed 1.53 um quantum dot laser with temperature-invariant emission wavelength", *Optics Express*, vol. 14, no. 8, p. 3273, 2006. DOI: 10.1364/OE.14.003273.

[109] F. W. Wise, "Lead Salt Quantum Dots: The Limit of Strong Quantum Confinement", *Accounts of Chemical Research*, vol. 33, no. 11, pp. 773–780, Nov. 1, 2000. DOI: 10.1021/ar970220q.

[110] E. H. Sargent, "Infrared Quantum Dots", *Advanced Materials*, vol. 17, no. 5, pp. 515–522, Mar. 8, 2005. DOI: 10.1002/adma.200401552.

[111] A. L. Lacaita, "Phase change memories: State-of-the-art, challenges and perspectives", *Solid-State Electronics*, Special Issue: Papers selected from the 2005 ULIS Conference, vol. 50, no. 1, pp. 24–31, Jan. 2006. DOI: 10.1016/j.sse.2005.10.046.

[112] F. Wang, "Non-Volatile Memory Devices Based on Chalcogenide Materials", in *Flash Memories*, I. Stievano, Ed., InTech, Sep. 6, 2011.

[113] E. D. Palik, in *Handbook of Optical Constants of Solids*, Burlington: Academic Press, 1997.

[114] R. Kitamura, L. Pilon, and M. Jonasz, "Optical constants of silica glass from extreme ultraviolet to far infrared at near room temperature", *Applied Optics*, vol. 46, no. 33, p. 8118, Nov. 20, 2007. DOI: 10.1364/AO.46.008118.

[115] J. Hu, V. Tarasov, N. Carlie, N.-N. Feng, L. Petit, A. Agarwal, K. Richardson, and L. Kimerling, "Si-CMOS-compatible lift-off fabrication of low-loss planar chalcogenide waveguides", *Optics Express*, vol. 15, no. 19, p. 11 798, 2007. DOI: 10.1364/OE.15.011798.

[116] J. Hu, N. Carlie, N.-N. Feng, L. Petit, A. Agarwal, K. Richardson, and L. Kimerling, "Planar waveguide-coupled, high-index-contrast, high-Q resonators in chalcogenide glass for sensing", *Optics Letters*, vol. 33, no. 21, p. 2500, Nov. 1, 2008. DOI: 10.1364/OL.33.002500.

[117] J. Hu, N.-N. Feng, N. Carlie, L. Petit, A. Agarwal, K. Richardson, and L. Kimerling, "Optical loss reduction in high-index-contrast chalcogenide glass waveguides via thermal reflow", *Optics Express*, vol. 18, no. 2, p. 1469, Jan. 18, 2010. DOI: 10.1364/OE.18.001469.

[118] S. Song, N. Carlie, J. Boudies, L. Petit, K. Richardson, and C. B. Arnold, "Spin-coating of Ge23Sb7S70 chalcogenide glass thin films", *Journal of Non-Crystalline Solids*, vol. 355, no. 45–47, pp. 2272–2278, Nov. 1, 2009. DOI: 10.1016/j.jnoncrysol.2009.07.015.

[119] P. K. Khanna and N. Singh, "Light emitting CdS quantum dots in PMMA: Synthesis and optical studies", *Journal of Luminescence*, vol. 127, no. 2, pp. 474–482, Dec. 2007. DOI: 10.1016/j.jlumin.2007.02.037.

[120] M. V. Kovalenko, M. Scheele, and D. V. Talapin, "Colloidal Nanocrystals with Molecular Metal Chalcogenide Surface Ligands", *Science*, vol. 324, no. 5933, pp. 1417–1420, Jun. 12, 2009. DOI: 10.1126/science.1170524. pmid: 19520953.

[121] M. V. Kovalenko, M. I. Bodnarchuk, J. Zaumseil, J.-S. Lee, and D. V. Talapin, "Expanding the Chemical Versatility of Colloidal Nanocrystals Capped with Molecular Metal Chalcogenide Ligands", *Journal of the American Chemical Society*, vol. 132, no. 29, pp. 10 085–10 092, Jul. 28, 2010. DOI: 10.1021/ja1024832.

[122] (2013). Climate Change 2013: The Physical Science Basis, Intergovernmental Panel on Climate Change, [Online]. Available: http://www.ipcc.ch/report/ar5/wg1/.

[123] P. Beiter. (2014). Renewable Energy Data Book, U.S. Department of Energy, [Online]. Available: http://www.nrel.gov/analysis/energy_data.html.

[124] (2012). SunShot Vision Study, [Online]. Available: http://energy.gov/eere/sunshot/sunshot-vision-study (visited on 03/28/2016).

[125] W. Shockley and H. J. Queisser, "Detailed Balance Limit of Efficiency of p-n Junction Solar Cells", *Journal of Applied Physics*, vol. 32, no. 3, pp. 510–519, Mar. 1, 1961. DOI: 10.1063/1.1736034.

[126] (2016). Best Research-Cell Efficiencies, National Renewable Energy Laboratory, [Online]. Available: http://www.nrel.gov/ncpv/images/efficiency_chart.jpg.

[127] T. Tiedje, E. Yablonovitch, G. D. Cody, and B. G. Brooks, "Limiting efficiency of silicon solar cells", *IEEE Transactions on Electron Devices*, vol. 31, no. 5, pp. 711–716, May 1984. DOI: 10.1109/T-ED.1984.21594.

[128] M. Pope and C. E. Swenberg, *Electronic Processes in Organic Crystals and Polymers*, 2 edition. New York: Oxford University Press, Dec. 2, 1999, 1328 pp.

[129] A. Köhler and H. Bässler, *Electronic Processes in Organic Semiconductors: AN INTRODUCTION*. Weinheim, Germany: Wiley-VCH Verlag GmbH & Co. KGaA, May 11, 2015.

[130] D. J. Griffiths, *Introduction to Quantum Mechanics*, 2nd edition. Upper Saddle River, NJ: Pearson Prentice Hall, Apr. 10, 2004, 480 pp.

[131] H. Uoyama, K. Goushi, K. Shizu, H. Nomura, and C. Adachi, "Highly efficient organic light-emitting diodes from delayed fluorescence", *Nature*, vol. 492, no. 7428, pp. 234–238, Dec. 13, 2012. DOI: 10.1038/nature11687.

[132] M. B. Smith and J. Michl, "Singlet Fission", *Chemical Reviews*, vol. 110, no. 11, pp. 6891–6936, Nov. 10, 2010. DOI: 10.1021/cr1002613.

[133] M. B. Smith and J. Michl, "Recent Advances in Singlet Fission", *Annual Review of Physical Chemistry*, vol. 64, no. 1, pp. 361–386, 2013. DOI: 10.1146/annurev-physchem-040412-110130.

[134] D. N. Congreve, J. Lee, N. J. Thompson, E. Hontz, S. R. Yost, P. D. Reusswig, M. E. Bahlke, S. Reineke, T. V. Voorhis, and M. A. Baldo, "External Quantum Efficiency Above 100% in a Singlet-Exciton-Fission–Based Organic Photovoltaic Cell", *Science*, vol. 340, no. 6130, pp. 334–337, Apr. 19, 2013. DOI: 10.1126/science.1232994. pmid: 23599489.

[135] D. L. Dexter, "Two ideas on energy transfer phenomena: Ion-pair effects involving the OH stretching mode, and sensitization of photovoltaic cells", *Journal of Luminescence*, vol. 18–19, Part 2, pp. 779–784, Jan. 1979. DOI: 10.1016/0022-2313(79)90235-7.

[136] M. Stavola, D. L. Dexter, and R. S. Knox, "Electron-hole pair excitation in semiconductors via energy transfer from an external sensitizer", *Physical Review B*, vol. 31, no. 4, pp. 2277–2289, Feb. 15, 1985. DOI: 10.1103/PhysRevB.31.2277.

[137] T. Hayashi, T. G. Castner, and R. W. Boyd, "Quenching of molecular fluorescence near the surface of a semiconductor", *Chemical Physics Letters*, vol. 94, no. 5, pp. 461–466, Feb. 4, 1983. DOI: 10.1016/0009-2614(83)85032-5.

[138] P. M. Whitmore, A. P. Alivisatos, and C. B. Harris, "Distance Dependence of Electronic Energy Transfer to Semiconductor Surfaces: N3pi* Pyrazine/GaAs (110)", *Physical Review Letters*, vol. 50, no. 14, pp. 1092–1094, Apr. 4, 1983. DOI: 10.1103/PhysRevLett.50.1092.

[139] M. I. Sluch, A. G. Vitukhnovsky, and M. C. Petty, "Anomalous distance dependence of fluorescence lifetime quenched by a semiconductor", *Physics Letters A*, vol. 200, no. 1, pp. 61–64, Apr. 10, 1995. DOI: 10.1016/0375-9601(95)00120-R.

[140] L. Danos, R. Greef, and T. Markvart, "Efficient fluorescence quenching near crystalline silicon from Langmuir–Blodgett dye films", *Thin Solid Films*, Proceedings on Advanced Materials and Concepts for Photovoltaics EMRS 2007 Conference, Strasbourg, France, vol. 516, no. 20, pp. 7251–7255, Aug. 30, 2008. DOI: 10.1016/j.tsf.2007.12.103.

[141] G. B. Piland, J. J. Burdett, T.-Y. Hung, P.-H. Chen, C.-F. Lin, T.-L. Chiu, J.-H. Lee, and C. J. Bardeen, "Dynamics of molecular excitons near a semiconductor surface studied by fluorescence quenching of polycrystalline tetracene on silicon", *Chemical Physics Letters*, vol. 601, pp. 33–38, May 9, 2014. DOI: 10.1016/j.cplett.2014.03.075.

[142] N. J. Thompson, M. W. B. Wilson, D. N. Congreve, P. R. Brown, J. M. Scherer, T. S. Bischof, M. Wu, N. Geva, M. Welborn, T. V. Voorhis, V. Bulović, M. G. Bawendi, and M. A. Baldo, "Energy harvesting of non-emissive triplet excitons in tetracene by emissive PbS nanocrystals", *Nature Materials*, vol. 13, no. 11, pp. 1039–1043, Nov. 2014. DOI: 10.1038/nmat4097.

[143] A. Yeltik, B. Guzelturk, P. L. Hernandez-Martinez, A. O. Govorov, and H. V. Demir, "Phonon-Assisted Exciton Transfer into Silicon Using Nanoemitters: The Role of Phonons and Temperature Effects in Förster Resonance Energy Transfer", *ACS Nano*, vol. 7, no. 12, pp. 10 492–10 501, 2013. DOI: 10.1021/nn404627p.

[144] V. K. Thorsmølle, R. D. Averitt, J. Demsar, D. L. Smith, S. Tretiak, R. L. Martin, X. Chi, B. K. Crone, A. P. Ramirez, and A. J. Taylor, "Morphology Effectively Controls Singlet-Triplet Exciton Relaxation and Charge Transport in Organic Semiconductors", *Physical Review Letters*, vol. 102, no. 1, p. 017 401, Jan. 5, 2009. DOI: 10.1103/PhysRevLett.102.017401.

[145] J. J. Burdett, A. M. Müller, D. Gosztola, and C. J. Bardeen, "Excited state dynamics in solid and monomeric tetracene: The roles of superradiance and exciton fission", *The Journal of Chemical Physics*, vol. 133, no. 14, p. 144 506, Oct. 14, 2010. DOI: 10.1063/1.3495764.

[146] T. C. Wu, N. J. Thompson, D. N. Congreve, E. Hontz, S. R. Yost, T. V. Voorhis, and M. A. Baldo, "Singlet fission efficiency in tetracene-based organic solar cells", *Applied Physics Letters*, vol. 104, no. 19, p. 193 901, May 12, 2014. DOI: 10.1063/1.4876600.

[147] D. L. Dexter, "A Theory of Sensitized Luminescence in Solids", *The Journal of Chemical Physics*, vol. 21, no. 5, pp. 836–850, May 1, 1953. DOI: 10.1063/1.1699044.

[148] G. D. Scholes, "Long-Range Resonance Energy Transfer in Molecular Systems", *Annual Review of Physical Chemistry*, vol. 54, no. 1, pp. 57–87, 2003. DOI: 10.1146/annurev.physchem.54.011002.103746. pmid: 12471171.

[149] G. L. Miller, D. a. H. Robinson, and J. D. Wiley, "Contactless measurement of semiconductor conductivity by radio frequency-free-carrier power absorption", *Review of Scientific Instruments*, vol. 47, no. 7, pp. 799–805, Jul. 1, 1976. DOI: 10.1063/1.1134756.

[150] E. Yablonovitch, D. L. Allara, C. C. Chang, T. Gmitter, and T. B. Bright, "Unusually Low Surface-Recombination Velocity on Silicon and Germanium Surfaces", *Physical Review Letters*, vol. 57, no. 2, pp. 249–252, Jul. 14, 1986. DOI: 10.1103/PhysRevLett.57.249.

[151] R. C. Johnson and R. E. Merrifield, "Effects of Magnetic Fields on the Mutual Annihilation of Triplet Excitons in Anthracene Crystals", *Physical Review B*, vol. 1, no. 2, pp. 896–902, Jan. 15, 1970. DOI: 10.1103/PhysRevB.1.896.

[152] V. Ern and R. E. Merrifield, "Magnetic Field Effect on Triplet Exciton Quenching in Organic Crystals", *Physical Review Letters*, vol. 21, no. 9, pp. 609–611, Aug. 26, 1968. DOI: 10.1103/PhysRevLett.21.609.

[153] S. L. Shapiro, *Ultrashort Light Pulses: PICOSECOND TECHNIQUES and Applications*. Springer Science & Business Media, Jun. 29, 2013, 397 pp.

[154] A. G. Aberle, "Surface passivation of crystalline silicon solar cells: A review", *Progress in Photovoltaics: Research and Applications*, vol. 8, no. 5, pp. 473–487, Sep. 1, 2000. DOI: 10.1002/1099-159X(200009/10)8:5<473::AID-PIP337>3.0.CO;2-D.

[155] B. E. Deal and A. S. Grove, "General Relationship for the Thermal Oxidation of Silicon", *Journal of Applied Physics*, vol. 36, no. 12, pp. 3770–3778, Dec. 1, 1965. DOI: 10.1063/1.1713945.

[156] H. Z. Massoud, J. D. Plummer, and E. A. Irene, "Thermal Oxidation of Silicon in Dry Oxygen Accurate Determination of the Kinetic Rate Constants", *Journal of The Electrochemical Society*, vol. 132, no. 7, pp. 1745–1753, Jan. 7, 1985. DOI: 10.1149/1.2114204.

[157] H. Z. Massoud, J. D. Plummer, and E. A. Irene, "Thermal Oxidation of Silicon in Dry Oxygen Growth-Rate Enhancement in the Thin Regime I . Experimental Results", *Journal of The Electrochemical Society*, vol. 132, no. 11, pp. 2685–2693, Jan. 11, 1985. DOI: 10.1149/1.2113648.

[158] H. Cui, C. X. Wang, G. W. Yang, and D. Jiang, "Origin of unusual rapid oxidation process for ultrathin oxidation (<2 nm) of silicon", *Applied Physics Letters*, vol. 93, no. 20, p. 203 113, Nov. 17, 2008. DOI: 10.1063/1.3030985.

[159] Y. Enta, B. S. Mun, M. Rossi, P. N. R. Jr, Z. Hussain, C. S. Fadley, K.-S. Lee, and S.-K. Kim, "Real-time observation of the dry oxidation of the Si(100) surface with ambient pressure x-ray photoelectron spectroscopy", *Applied Physics Letters*, vol. 92, no. 1, p. 012 110, Jan. 7, 2008. DOI: 10.1063/1.2830332.

[160] C. Krzeminski, G. Larrieu, J. Penaud, E. Lampin, and E. Dubois, "Silicon dry oxidation kinetics at low temperature in the nanometric range: Modeling and experiment", *Journal of Applied Physics*, vol. 101, no. 6, p. 064 908, Mar. 15, 2007. DOI: 10.1063/1.2711764.

[161] C. van der Marel, M. A. Verheijen, Y. Tamminga, R. H. W. Pijnenburg, N. Tombros, and F. Cubaynes, "Thickness and composition of ultrathin SiO2 layers on Si", *Journal of Vacuum Science & Technology A*, vol. 22, no. 4, pp. 1572–1578, Jul. 1, 2004. DOI: 10.1116/1.1701864.